

AUTOMATING SURFACE WATER DETECTION FOR RIVERS

THE ESTIMATION OF THE GEOMETRY OF RIVERS BASED ON OPTICAL EARTH
OBSERVATION SENSORS

BY J.J.M. THISSEN



AUTOMATING SURFACE WATER DETECTION FOR RIVERS

THE ESTIMATION OF THE GEOMETRY OF RIVERS BASED ON OPTICAL
EARTH OBSERVATION SENSORS

By

J.J.M. Thissen

Student number: 1767089

in partial fulfilment of the requirements for the degree of

Master of Science

in Civil Engineering & Management

at the University of Twente,
Faculty of Engineering Technology

February, 2019

Keywords: automated surface water detection, river geometry, river polygon, centerline, multispectral satellite imagery, Google Earth Engine, Landsat 8, Sentinel-2

Supervisors:	Prof. Dr. S.J.M.H. Hulscher	University of Twente
	Ir. A. Bomers	University of Twente
	Ir. K.D. Berends	University of Twente
	Dr. Ir. M.F.M. Yossef	Deltares
	Ir. J.S. de Jong	Deltares

SUMMARY

This thesis studies the extent to which the geometry of rivers around the globe can be determined in an automated manner, based on openly available optical Earth Observational (EO) satellite sensors. Knowledge of the course of a river allows for the bathymetry to be estimated. Currently, the course of a river, at any given point in time, is derived by means of visual inspection based on geographical maps, which may be time-consuming. Automating this process can therefore be highly beneficial. The utilization of remote sensing technology is investigated to observe the dynamics of rivers at frequent time intervals. Google Earth Engine is adopted for the analysis, interpretation and manipulation of multispectral satellite data.

In order to detect surface water within a multispectral satellite image, water indices are utilized, followed by a HAND-map and an image thresholding approach (Otsu's method). The purpose of a water index is to enhance water features, the HAND-map to avoid potential errors due to shadows, and Otsu's method to reduce the resulting grayscale image to a binary surface water mask, separating foreground (water) from background features. To estimate the bounds of a river under cloudy circumstances, multiple historical images are sampled to generate a composite, representing the water occurrence of a river over time in the form of a binary image. Historical images are weighted based on the date they were sampled, in order to reduce the impact of varying surface water widths over time. The composite is used to estimate segments of a river that were initially unknown due to the presence of clouds.

The resulting surface water mask is converted to a smooth river polygon. River widths are subsequently derived based on a Euclidian distance map in combination with a centerline, which is obtained by extracting a skeleton from a Voronoi diagram, followed by a pruning procedure.

The approach has been validated based on two river polygons provided by Rijkswaterstaat, representing a segment of the Meuse and the Rhine. The estimated geometries based on EO satellite imagery were found to be highly similar to that of the two river polygons. Throughout 2016, for a segment of the Meuse, deviations between +2 and -2 meters (+1.53% and -1.53%) as well as +1 and -8 meters (+0.76% and -6.11%) were found compared to data provided by Rijkswaterstaat, for cloudless and cloudy images respectively. For the segment that comprises of the Rhine and the Waal, deviations between +29 and -15 meters (+7.36% and -3.81%) as well as +17 and -13 meters (+4.31% and -3.30%) were found for cloudless and cloudy images respectively, for the same year. Furthermore, a comparison towards a recently build database consisting of global river widths from Landsat imagery (GRWL; Allen and Pavelsky, 2018) revealed clear similarities.

Although the estimation of the geometry of rivers in a more or less automated manner was found to be achievable, its global applicability remains limited to a local scale. Currently, the biggest limitation is the fact that the amount of usable memory is capped within GEE. Computations were found to be too resource-demanding, limiting the maximum size of a river polygon that can be generated. Furthermore, the estimation of the geometry of a river is found to be limited to rivers that are at least three to four times wider than the corresponding satellite's spatial resolution in order to obtain usable results. Rivers that are relatively relative narrow (<100 meters) were found to be difficult to identify using either Sentinel-2 or Landsat 8 multispectral satellite data.

CONTENTS

Summary	3
List of figures	6
List of tables	7
1 Introduction	8
1.1 Background.....	8
1.2 Problem definition.....	8
1.3 Research gap	9
1.4 Research objective & questions	10
1.5 Thesis outline.....	10
2 Literature review: overview of the current remote sensing techniques	12
2.1 Optical Earth observation sensors.....	12
2.2 Surface water detection methods.....	13
2.3 Surface water detection challenges for rivers.....	16
2.4 Conclusions.....	17
3 Method	18
3.1 Study area: Trinity River, Texas, USA	18
3.2 Data resources.....	19
3.3 Avoidance of image disturbances.....	20
3.4 Conversion to a river polygon and spatial interpolation methods.....	26
3.5 Derivation river widths	29
3.6 Exclusion of surface water	32
4 Results and evaluation	34
4.1 Validation	34
4.2 Global applicability & limitations	43
5. Sensitivity analysis	50
6. Discussion	61
7. Conclusions and recommendations	63
7.1 Conclusions.....	63
7.1.1 Answers to research questions.....	63

7.2	Recommendations	64
7.2.2	Recommendations for further work.....	64
7.2.1	Recommendations for use	66
	References.....	69
	Appendix A: Otsu thresholding & Canny edge detector	73
	Appendix B: Morphological operators.....	75
	Appendix C: Overlapped river polygons	77
	Appendix D: River classification scheme	79
	Appendix E: Scripts & typical memory usage	80
	Appendix F: Inaccurate estimates under highly variable conditions.....	83

LIST OF FIGURES

Figure 1.1 – Overview of the research project (RQ = research question).....	11
Figure 2.1 – Reflectance values of common land cover objects.....	14
Figure 3.1 – Study area: Trinity River, Texas, USA.....	18
Figure 3.2 – Surface water detection of the Trinity River, Texas, USA.....	20
Figure 3.3 – Estimated surface water mask.....	22
Figure 3.4 – The relationship between A_{ratio} and the kernel radius r as well as various weight distributions	23
Figure 3.5 – Updated estimated surface water mask.....	24
Figure 3.6 – First three steps of the generation of a surface water mask in an automated manner.....	24
Figure 3.7 – Steps towards the generation of a historical composite	25
Figure 3.8 – Steps towards the final surface water mask	26
Figure 3.9 – Differences between various interpolation techniques applied to a river polygon (Landsat 8).....	28
Figure 3.10 – Differences between various interpolation techniques applied to a river polygon (Sentinel-2).....	29
Figure 3.11 – The effect of the opening operator	30
Figure 3.12 – Overview of the generation of a pruned skeleton	32
Figure 3.13 – Final estimation of the geometry of a segment of the Trinity River.....	32
Figure 3.14 – Demonstration of the exclusion of surface water for a segment of the Waal.	33
Figure 4.1 – Automatically generated river polygon vs a river polygon provided by Rijkswaterstaat (Meuse).....	35
Figure 4.2 – The centerline for a segment of the Meuse (cloudless multispectral image).....	37
Figure 4.3 – The centerline for a segment of the Meuse (cloudy multispectral image).....	37
Figure 4.4 – Comparison between the river widths of multiple datasets (Meuse)	38
Figure 4.5 – Comparison between the quality of the GRWL centerline and the Voronoi-based centerline	38
Figure 4.6 – Automatically generated river polygon vs a river polygon provided by Rijkswaterstaat (Rhine)	39
Figure 4.7 – The centerline for a segment of the Rhine (cloudless multispectral image).....	41
Figure 4.8 – The centerline for a segment of the Rhine (cloudy multispectral image).....	41
Figure 4.9 – Comparison between the river widths of multiple datasets (Meuse).	42
Figure 4.10 – An overview of the selected rivers and their locations.	45
Figure 4.11 – Typical resulting river polygons for the Danube in Budapest, Hungary	45
Figure 4.12 – Typical resulting river polygons for the Murray River in Victoria/New South Wales, Australia.....	46
Figure 4.13 – Typical resulting river polygons for the Niger River in Segou, Mali.....	46
Figure 4.14 – Typical resulting river polygon for the Magdalena River nearby La Dorada, Colombia.....	46
Figure 4.15 – Typical resulting river polygon for the Thanlyin River nearby Khe Hpyu, Myanmar.	47
Figure 4.16 – Typical resulting river polygon for the Thanlyin River nearby Turtas, Russia.....	47
Figure 4.17 – Typical resulting river polygon for the Yellowstone River nearby Forsyth, USA.	47
Figure 4.18 – Typical resulting centerline for a segment of the Danube in Budapest, Hungary	49
Figure 4.19 – Typical resulting centerlines for the Magdalena River, Colombia and the Thanlyin River, Myanmar. ...	50
Figure 5.1 – Sensitivity of the Trinity River towards a gradually enlarged time window of the historical composite..	50
Figure 5.2 – Sensitivity of the historical composite of the Trinity River towards an increasing threshold value	52
Figure 5.4 – Sensitivity of varying weight distributions.....	54
Figure 5.5 – Sensitivity of varying kernel radii (erosion) towards the geometry of Trinity River.....	55
Figure 5.6 – The impact of erosion towards the derived surface water mask of the Trinity River.....	56
Figure 5.7 – Sensitivity of varying distributions towards the total surface area for a segment of the Trinity River ...	57
Figure 5.8 – The estimated historical composites for the distributions as illustrated in Figure 5.7	57
Figure 5.9 – Sensitivity of the total water surface area towards varying kernel radii (opening).....	58
Figure 5.10 – The impact of opening towards the derived surface water masks for varying kernel radii.....	59
Figure 5.11 – The impact of various projection scales towards the quality of the river polygon and the centerline...	60
Figure 5.12 – The impact of the number of vertices used towards the quality of the EDM, and thus the centerline....	60
Figure B.1 – Erosion of binary image A by kernel B.	75
Figure B.2 – Dilation of binary image A by kernel B.....	76
Figure C.1 – Automatically generated river polygon vs a river polygon provided by Rijkswaterstaat (Meuse).....	77
Figure C.2 – Automatically generated river polygon vs a river polygon provided by Rijkswaterstaat (Rhine).....	78
Figure D.1 – Classification of river channel patterns.	79
Figure E.1 – Profiling results of a segment of the Trinity River based on bilinear interpolation.....	81
Figure E.2 – Profiling results of a segment of the Trinity River based on bicubic interpolation	82
Figure F.1 – Scenario for a relatively narrow river subject to highly variable surface water widths.	83
Figure F.2 – Scenario for a relatively wide river subject to highly variable surface water widths.....	84

LIST OF TABLES

Table 2.1 – Commonly used remote sensors for surface water detection.....	13
Table 2.2 – Popular water indices including their equations.	16
Table 3.1 – Relevant specifications for Landsat 8 and Sentinel-2 satellites.	19
Table 4.1 – Relative differences of the total surface areas and the mean river widths (Meuse, cloudless).....	36
Table 4.2 – Relative differences of the total surface areas and the mean river widths (Meuse, cloudy).....	36
Table 4.3 – Relative differences of the total surface areas and the mean river widths (Rhine, cloudless)..	40
Table 4.4 – Relative differences of the total surface areas and the mean river widths (Rhine, cloudy).....	40
Table 5.1 – Sensitivity data for a gradually enlarged sampling window (26-10-2016)	51
Table 5.2 – Sensitivity data for a gradually enlarged sampling window (24-04-2017)	51
Table 5.3 – Sensitivity data for varying threshold values.....	52
Table 5.4 – Sensitivity data for varying weighted distributions.....	54
Table 5.5 – Sensitivity data for varying kernel radii (erosion).	55
Table 5.6 – Sensitivity data for varying distributions of A and r	57
Table 5.7 – Sensitivity for varying kernel radii (opening).....	58

1 INTRODUCTION

1.1 BACKGROUND

River monitoring is an essential aspect in providing safety against floods, sufficient amount of available water and safe navigation for ships. Traditionally, people have inhabited places close to rivers or lakes to ensure fresh water supply for a variety of purposes. Kummu et al. (2011) stated that over 50% of the population across the globe lives closer than 3 kilometers to a surface freshwater body, and that only 10% of the population lives further than 10 kilometers away. Additionally, the competitiveness as well as the economic viability of ports is directly linked to the condition of the waterway network, providing access to smooth and safe transport by water.

To provide answers to questions related to flood safety, water availability and safe navigation of ships by means of numerical models, information about the bathymetry of rivers is required. However, bathymetric data of rivers is generally limited. This is due to the fact that (1) the collection of data requires a significant amount of time and effort, (2) the collection of data is often deemed as expensive or even (3) because rivers change their course throughout time. To solve this problem, Deltares, an independent institute for applied research in the field of water, developed a rapid assessment tool which aims to “*rapidly assess a river’s suitability for inland navigation based on state-of-the-art scientific knowledge and freely available data sources*” (Zervakis, 2015). More specifically, the tool aims to provide quantitative information regarding geometrical, hydrological and geographical river aspects as well as navigational bottlenecks and the costs of required interventions, based on open source data. As a result, the tool allows for policymakers to evaluate a river’s navigation potential without the need for extensive input data (Beltman, 2016).

The Deltares Rapid Assessment Tool for Inland Navigation (D-RATIN) performs a total of three steps. Firstly, the D-RATIN attempts to reconstruct a river’s bed-levels by combining a geometrical and physics-based model with interpolated bathymetric data. Subsequently, a 1D SOBEK model is set-up to calculate water depths based on the generated river bathymetry. Lastly, a route optimization algorithm using a cost-function is applied in order to obtain the optimal route, calculate the volume of dredging and the costs of the needed river interventions for a given ship dimension (Beltman, 2016).

1.2 PROBLEM DEFINITION

In the current version of the D-RATIN, both the physics-based dataset and the interpolated dataset, which are fused to assess a river’s bed-levels, are reliant on a curvilinear grid that defines how the input data is stored, manipulated and displayed. Additionally, the curvilinear grid serves as guideline for the direction of the flow relevant for the curvature of a river. However, in order to compute such a grid, knowledge about the course of a river and its corresponding banks is required.

The course of a river, at any instance in time, can be expressed through its width, that is the distance between a river’s banks as well as the direction of flow. This particular information can be derived from a geometric shape: a river polygon. A river polygon can be interpreted as a two-dimensional shape consisting of three or more vertices. The D-RATIN utilizes a river polygon to

delineate a river and compute the above-mentioned curvilinear grid. In the current build, a river polygon is either obtained through a given dataset or is determined based on visual inspection (i.e. by manually drawing the shape on the basis of a geographical map). The main problem of the current procedure is that the estimation of the geometry of a river by means of visual inspection may be highly time-consuming, depending on the overall size and complexity of a river (in terms of its shape).

1.3 RESEARCH GAP

State-of-the-art remote sensing techniques allow for the continuous monitoring of rivers at multiple scales around the globe. Various studies have been performed in the past to improve the separability between water and background features based on optical Earth Observation (EO) sensors (Manavalan et al., 1993; Frazier and Page, 2000; Ozesmi and Bauer, 2002; Sun et al, 2011; Acharya et al., 2016; Olthof, 2017). Optical EO sensors make use of visible, near infrared and shortwave infrared light to form images of the Earth's surface based on the reflectance of solar radiation from objects on the ground. The ability of a surface to reflect radiant energy differs per material, allowing for the detection, extraction and monitorization of surface water over time. Especially methods based on water indices were proven to be effective, which are calculated based on a ratio between different spectral bands (specific range of wavelengths within the electromagnetic spectrum such as red, green or infrared) (McFeeters, 1996; Xu, 2006; Duan & Bastiaanssen, 2013; Hui et al., 2008; Murray et al., 2012). However, these methods rely on a threshold value to separate water from non-water features, that vary on a case-by-case basis as a result of slightly varying spectral properties of open water across the globe. More recent studies provide methods to automatically determine an optimal water thresholding value instead of doing so manually, allowing for the detection of water bodies in a more automated manner (Li and Sheng, 2012; Li and Wang, 2012; Donchyts et al., 2016; Xie et al., 2016; Zhang et al., 2018).

The most problematic issue is that optical remote sensors remain hindered by cloud obstructions, limiting their applicability to favorable weather conditions. Optical EO sensors combined with Synthetic Aperture Radar (SAR) technology can potentially solve this issue due to the ability of SAR to penetrate clouds. However, the application of the two data sources in tandem is currently limited due to inconsistent data availability, distinct physical properties that optical and SAR instruments sense, and dissimilar data delivery platforms (Markert et al, 2018). Cloudless composite multispectral satellite images are often generated to deal with cloud obstructions (e.g. percentile or interval mean composites). However, this is in most cases only suitable to detect long-term changes, or water bodies that change relatively slowly over time (e.g., Potapov et al., 2012; Hansen et al., 2013; Donchyts et al., 2016). Furthermore, the detection of surface water has been investigated on a global scale, where long-term surface water changes have been mapped in detail based on inter-annual composites of multispectral satellite images in combination with water indices (Aqua Monitor; Donchyts et al., 2016).

Although much has been achieved in the recent years towards the detection of surface water, an all-inclusive approach, specifically focused on the detection of rivers, that allows for the geometry of a river to be estimated on a global level, at more or less any point in time¹, in an automated manner², does not yet seem to exist. The extent to which this can be achieved is explored.

¹ Assuming that satellite images are indeed available for a certain date of interest.

² That is, the requirement of limited user-input, such as the area of interest and a specific point in time.

Even though this research specifically addresses a problem related to estimation of the bathymetry of a river (that is, the D-RATIN), an automated method that allows for estimation of the geometry of a river from multispectral satellite images offers value for other purposes as well. For example, a series of river polygons may be used to obtain knowledge of the behavior of a river over time, or to extend and improve flood maps.

1.4 RESEARCH OBJECTIVE & QUESTIONS

The objective of this thesis is to investigate the extent to which the geometry of rivers can be determined in an automated manner, based on openly available multispectral satellite images. Furthermore, there is a need to explore the extent to which the geometry of rivers can be estimated on a global scale. Four research questions have been formed to guide the study towards the objective. These are as follows:

- 1. How can river bounds be detected in an automated manner, in case a multispectral satellite image is subject to common disturbances, such as clouds, haze or fog?**
- 2. How can river widths be determined in an automated manner, based on openly available multispectral satellite imagery?**
- 3. What is the global applicability of river polygons?**
- 4. What is the sensitivity of parameters that directly influence the geometry of a river polygon?**

1.5 THESIS OUTLINE

The structure of this thesis is laid out as follows (see Figure 1.1):

- Chapter 2 provides an overview of commonly used remote sensing techniques by reviewing the current literature, specifically targeted at the detection of surface water using optical EO sensors.
- Chapter 3 describes the steps taken to estimate the geometry of a river based on optical EO sensors. Mostly existing concepts from various fields are combined to do so.
- Chapter 4 features the results. In this chapter, the method is validated, the global applicability of river polygons is assessed and the limitations are listed.
- Chapter 5 describes the sensitivity analysis, which provides insight into the dependency of the estimated river geometry towards influential variables.
- Chapter 6 presents the discussion.
- Chapter 7 describes the conclusions and the recommendations.

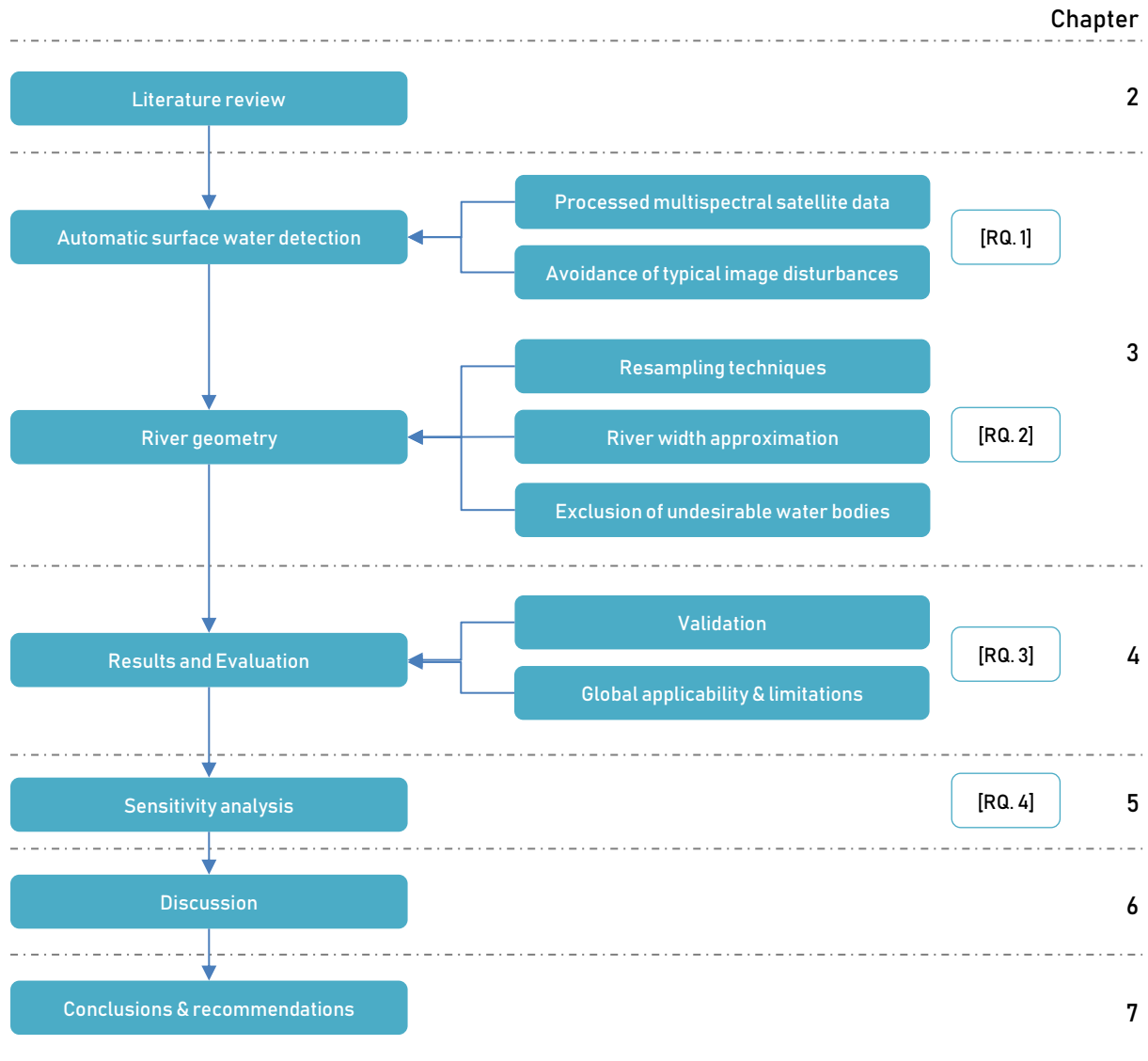


Figure 1.1 – Overview of the research project (RQ = research question).

Additionally, a total of six appendices that provide supplementary information are included. Links to the developed scripts can be found in Appendix E.

- Appendix A: Otsu thresholding & Canny edge detection;
- Appendix B: Morphological operators;
- Appendix C: Overlapped river polygons;
- Appendix D: River classification scheme;
- Appendix E: Scripts & typical memory usage;
- Appendix F: Inaccurate estimates under highly variable conditions.

2 LITERATURE REVIEW: OVERVIEW OF THE CURRENT REMOTE SENSING TECHNIQUES

This chapter provides an overview of commonly used remote sensing techniques described by the current literature, specifically targeted at the detection of surface water. Firstly, commonly used remote sensors and satellites are investigated (§2.1). Subsequently, methods that allow for the detection of surface water are explored (§2.2). Thereafter, challenges related to the detection of rivers are researched (§2.3). Lastly, the main conclusions of the literature study are formulated (§2.4).

2.1 OPTICAL EARTH OBSERVATION SENSORS

Remote sensing technology offers effective ways to observe surface water dynamics and allows for continuous monitoring of the Earth's surface at multiple scales (Huang et al., 2018). Due to the availability of spatially and temporally frequent observational data of physical attributes about the Earth's surface, the dynamics of rivers can be detected at frequent time intervals.

Recent studies related to surface water and flood inundation mainly focus on making use of satellite-based optical Earth Observation (EO) sensors to detect changes of surface water bodies. Generally, there are two categories of sensors that are able to measure surface water –microwave sensors and optical sensors. Microwave sensors are able to function day and night under any weather conditions and have the ability to penetrate cloud coverage in addition to certain vegetation coverage. Schumann and Moller (2015) conducted a detailed review of microwave remote sensing for flood inundation and found Synthetic Aperture Radar (SAR) to be the most suitable sensor type for monitoring flood inundation. Optical EO sensors are only able to capture features in case of favorable weather conditions. Nevertheless, optical EO sensors are the preferred source of information due to their straightforward interpretability of water features (Bioresita et al., 2018). They have been widely used in terms of surface water detection due to high availability of data, as well as suitable spatial and temporal resolutions (Huang et al., 2015). Although optical EO sensors are often preferred over SAR technology for the detection of surface water, the combination of both sensors for this purpose have recently been investigated thoroughly since the recent launch of both Sentinel-1 (SAR; 03-04-2014) and Sentinel-2 (optical EO; 23-06-2015). However, the application of the two data sources in tandem is currently still in its early stages due to inconsistent data availability, distinct physical properties that optical and SAR instruments sense, and dissimilar data delivery platforms (Markert et al, 2018). This limits the use for the purpose of surface water detection.

One of the most important factors that decides the usage between different optical remote sensors in terms of surface water detection is the spatial resolution. Spatial resolution refers to the area of ground observed within a pixel and determines the level of detail captured by the sensors. Another important aspect is a satellite's temporal resolution, which is defined as the period of time required for a satellite to revisit a specific geographic location (revisit period). Although various optical sensors, containing different spatial and temporal resolutions, are available, medium spatial resolution sensors (5-200 meters per pixel) with a relatively high revisit period (5-30 days) have widely been used over the past years to detect surface water of all kinds (e.g., Acharya et al., 2016; Donchyts et al., 2016; Du et al., 2014; Gao et al., 2016; Ji et al.,

2015; Li et al., 2016; Liu et al., 2016; Singh et al., 2016; Xie et al., 2016; Yang et al., 2015). Multispectral satellite data acquired through Landsat EO satellites is often used, with Landsat 8 providing the highest spatial resolution—30 meters per pixel (functional since 11-02-2013). Alternatively, Sentinel-2 EO data can be used since 23-06-2015, which provides a spatial resolution of 10 meters. Both Du et al. (2016) and Yang et al. (2017) have verified its ability to map surface water bodies.

Huang et al. (2018) provides an overview of the most commonly used satellite for surface water detection as well as their features. This is illustrated in Table 2.1. In this study, data originating from the medium-resolution EO sensors, specifically the Landsat-8 and Sentinel-2 satellites, is used. The main reasons for the selection of these two satellites is that a combination provides relatively high-resolution EO data (Sentinel-2: 10 × 10 m per pixel; Landsat 8: 30 × 30 per pixel), is freely accessible, and provides sufficiently available data – from 11-02-2013 up to now. Other optical EO sensors are either of commercial nature or provide data of much lower spatial resolution compared to Landsat 8 and Sentinel-2.

Table 2.1 – Commonly used remote sensors for surface water detection (Huang et al., 2018).

Category	Satellite/sensor	Number of bands	Spatial resolution (m)	Temporal resolution (day)	Data availability
Coarse > 200 m	NOAA/AVHRR	5	1,100	0.5	1978-
	MODIS	36	250–1,000	0.5	1999-
	Suomi NPP-VIIRS	22	375–750	0.5	2012-
	MERIS	15	300	3	2002-2012
	Sentinel-3 OLCI	21	300	2	2016-
Medium 5-200 m	Landsat	4–9	15–80	16	1972-
	SPOT	4–5	2.5–20	26	1986-
	Aster	14	15–90	16	1999-
	Sentinel-2 MSI	13	10–60	5	2015-
High < 5 m	IKONOS	5	1–4	1.5–3	1999-
	QuickBird	5	0.61–2.24	2.7	2001-
	WorldView	4–17	0.31–2.40	1–4	2007-
	RapidEye	5	5	1–5.5	2008-
	ZY-3	4	2.1–5.8	5	2012-
	GF-1/GF-2	5	1–16	4–5	2013-

2.2 SURFACE WATER DETECTION METHODS

Essentially, the principle of extracting any kind of surface cover type from optical images is based on an object's ability to reflect radiant energy within a certain spectral channel. This can be interpreted as a range of wavelengths within the electromagnetic spectrum, such as ultraviolet, visible or infrared light. The main principle of surface water detection from multispectral satellite images is the significantly lower reflectance of water in infrared channels, compared to that of other land cover types. Researchers at the United States Geological Survey (USGS) Spectroscopy Laboratory have measured the spectral reflectance of thousands of materials in a lab and compiled the results, proving the noticeably of lower reflectance values in infrared channels (official publication: Kokaly et al., 2017; data release: Kokaly et al., 2017). A comparison between the reflectance of water and other land cover types is presented in Figure 2.1.

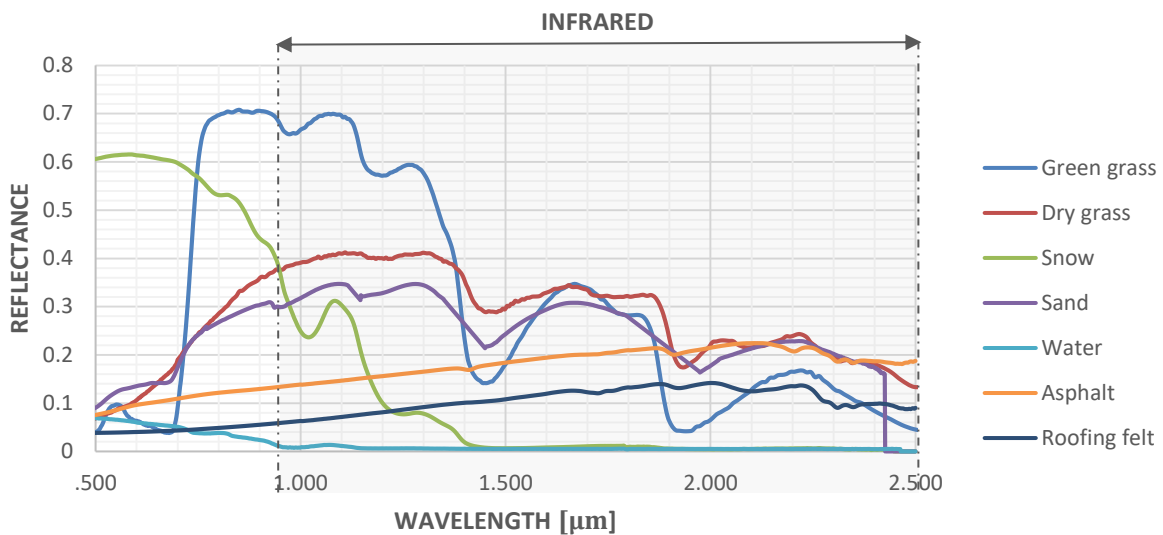


Figure 2.1 – Reflectance values of common land cover objects, including water. Collected from United States Geological Survey (USGS) digital spectral library (<https://speclab.cr.usgs.gov/spectral-lib.html#description>).

Based on the relatively low reflectance of water, various techniques have been developed for detecting surface water from multispectral satellite imagery. Yang et al. (2015) ultimately grouped water body identification methods using the following categories:

1. Digitizing through visual interpretation, which is considered to be a highly accurate method, but extremely labor intensive and therefore difficult to repeat.
2. Density slicing of a single infrared band, which applies a fixed threshold to a given spectral band to derive a water map (Frazier and Page, 2000). This is done by dividing the pixel values of a single band into intervals (e.g. in the form of a histogram), followed by assigning a color to each interval, allowing for an analysis of the differences between colors.
3. Calculating spectral (water) indices, which combines two or more bands by mathematical ratios to derive water pixels from an image (e.g., Chen et al., 2014; Chowdary et al., 2008; Choi & Bindschadler, 2004; Feyisa et al., 2014; Fisher et al., 2016; Hoberg et al., 2015; Hui et al., 2008; McFeeters, 1996; Mohammadi et al., 2017; Salomonson & Appel, 2004; Xu, 2006).
4. Either supervised or unsupervised³ classification methods (e.g., Manavalan et al., 1993; Ozesmi and Bauer, 2002), used to generate land cover maps from which water maps could be extracted.

Additionally, decision trees were built using multispectral bands to detect surface water bodies (e.g., Acharya et al., 2016; Olthof, 2017; Sun et al., 2011). Huang et al. (2018) concluded that the problem with a majority of the methods is that their classification rules are difficult to build and therefore are often not robust enough to be universally applicable. Donchyts (2018) also stated

³ In supervised classification, classes within an image are predicted based on labeled data (e.g. sample/training data). In unsupervised classification, data is unlabeled, and the algorithm is left to its own device to predict the classes within an image, based on underlying structures.

that, even though most recent methods provide better classification accuracy between water and non-water coverage, they mostly require manual threshold adjustments to provide the best results. This largely impacts their application on global scale, due to the need for manual adjustments per location.

Surface water detection on the basis of water indices have been widely studied over the past decades (grouped as (3) by Yang et al., 2015) and its ability to separate water from background features (non-water) has proven to be effective. This works by applying a mathematical ratio between two or more spectral bands of a multispectral satellite image, allowing for the identification of a threshold value that separates water from non-water features. Early studies proposed the Tasseled Cap Wetness (TCW) (Crist, 1985) to separate water and non-water surfaces, and the Normalized Difference Vegetation Index (NDVI), a vegetation index which has been used to detect water and floods in some studies (Domenikiotis et al., 2003). More useful indices are the Normalized Difference Water Index (NDWI) (McFeeters, 1996) and the modified NDWI (MNDWI) (Xu, 2006). The NDWI has been widely used during the first 10 years of the 21st century (Chowdary et al., 2008; Hui et al., 2008). The MNDWI became widely accepted as the more stable and reliable index after that period, due to the fact that the short-wave infrared band is able to reflect more subtle characteristics of water compared to the near-infrared band used in the NDWI. Although the MNDWI is generally favored to discriminate water from land, it is found to be much more sensitive to snow and cold clouds. This is because, even though snow generally has a higher reflectance than water, reflectance in the short-wave infrared band as well as the green band is more or less equal to that of water. In fact, the Normalized Difference Snow Index (NDSI) is often used to identify surface areas covered by snow (Choi and Bindenschadler, 2004; Salomonson and Appel, 2004). Later, in 2009, Ji et al. suggested that adjustment of the threshold value based on the location could usually achieve better extraction results. Li and Sheng (2012) then developed an automated method for mapping glacier lake dynamics using NDWI, and Allen and Pavelsky (2015) adopted the scheme to generate a land-water mask for North America, based on the MNDWI. Donchyts et al. (2016) subsequently developed an adaptive threshold detection method based on the MNDWI, thus allowing water pixels to be classified in an automated manner.

Although more water indices allowing for the detection of surface water were introduced quite recently, such as the Automated Water Extraction Index (AWEI) (Feyisa et al., 2014) and Water Index (WI₂₀₁₅) (Fisher et al., 2016), no index was proven to perform the best across all water and non-water pixel types according to research conducted by Fisher et al. (2016) based on Landsat's 30 meters resolution imagery. A water extraction method that performs perfectly for all satellites/sensors has therefore yet to be formed. An overview of the aforementioned popular water indices including their corresponding equations is presented in Table 2.2.

Table 2.2 – Popular water indices including their equations. ρ represents the spectral reflectance of a band. “Nir” refers to the near-infrared band and both “swir1” and “swir2” refer to the short-wave infrared bands at different wavelengths (1.55-175 μm and 2.08-2.35 μm respectively).

Indices	Spectral index equations
NDWI	$\frac{\rho_{green} - \rho_{nir}}{\rho_{green} + \rho_{nir}}$
MNDWI	$\frac{\rho_{green} - \rho_{swir1}}{\rho_{green} + \rho_{swir1}}$
AWEI	$4 \times (\rho_{green} - \rho_{swir1}) - (0.25 \times \rho_{nir} + 2.75 \times \rho_{swir2})$
WI ₂₀₁₅	$1.7204 + 171 \times \rho_{green} + 3 \times \rho_{red} - 70 \times \rho_{nir} - 45 \times \rho_{swir1} - 71 \times \rho_{swir2}$

2.3 SURFACE WATER DETECTION CHALLENGES FOR RIVERS

Although the application of water indices to detect surface water from a multispectral satellite images have been used widely, and, more recently successfully in an automated manner, the most serious issue is that optical EO sensing data is easily affected by cloud obstructions. This limits its applicability to favorable weather conditions, and poses a problem considering that the fact that multispectral satellite data free of clouds is not always available. It was found that this severely hinders the detection of surface water in tropical regions in particular, whereas arid regions stand out as particularly cloudless (Mercury et al, 2012; Gunderson & Chodas, 2011; Wylie et al., 2005). For images of the Landsat series specifically, Pekel et al. (2016) found that more cloudless observations are available during dry seasons than wet seasons.

Cloudless composite images are usually generated to deal with cloud obstructions, which are often based on average reflectance composites instead of instantaneous images, or percentiles are employed to estimate the average cloud-free reflectance values (e.g., Potapov et al., 2012; Hansen et al., 2013; Donchyts et al., 2016). Another commonly used approach to build the composite is to iterate through all pixels over multiple satellite images, where pixels that are found to be the “least cloudy” are identified and combined into a single image. These types of pixels can be obtained by looking for various properties belonging to clouds – that is, their brightness in red, green, blue and infrared bands, their reasonably cool temperature and their distinction from snow. However, the disadvantage of these methods is that they are in most cases only suitable to detect long-term changes, or water bodies that change relatively slowly over time. In case of rivers that rapidly alter their course over time, changes towards the stream width⁴ may not be captured.

Donchyts (2018) recently introduced a new approach which allows for the detection of surface water of a partially visible water body by analyzing multiple cloud-free historical images, in which accurate estimates of the surface water body can be established using a probability density function. The method was applied and validated based on a large reservoir, on the assumption that the morphology of the water body does not change significantly. However, its application to rivers, specifically, has not been demonstrated. Nonetheless, unlike the typical composite approach, which is suitable for long-term changes, this particular method shows good potential to estimate the course of rivers that are partially covered by clouds. In theory, a set of cloud-free images of a river can be sampled over a certain time span (e.g. 1 month). Assuming that the course

⁴ In this thesis, stream width is defined as the wetted width of flowing water within a channel, or river.

of a river does not drastically change, its bounds can be estimated by combining said images, resulting in the average representation of the course of a river over time.

Lastly, another approach is to merge optical EO sensors with SAR technology, due to the fact that SAR is able to avoid cloud obstructions and optical EO techniques provide proven methods to interpret water features (Ward et al., 2014). However, the combination of the two data sources is, as mentioned earlier in §2.1, still a challenge due to inconsistent data availability, distinct physical properties and dissimilar data delivery (Markert et al, 2018).

Besides the hindrance by clouds, other common issues in regard to the detection of surface water from multispectral satellite imagery exist. Most notably, cloud shadows, hill shadows and snow cover, all of which are often mistakenly interpreted as water. However, methods introduced over the past years have been able to mostly avert these issues to a large extent. Digital elevation model (DEM) data is often used as supplementary information to eliminate the confusion caused by shadows (Gianinetto et al., 2006; Qi et al., 2009). Zhu & Woodcock (2012) and Zhu & Woodcock (2014) describe methods to detect cloud shadows and snow by relying on information of view angle of the satellite sensor in combination with the position of the sun (solar azimuth and solar zenith). Tan et al., (2013) used the same framework in addition to a Digital Elevation Map (DEM) allowing for the detection hill shadows. Furthermore, modified DEMs such as the Height Above the Nearest Drainage (HAND; Renno et al., 2008) and the Multi-resolution Valley Bottom Flatness (MrVBF; Gallant and Downling, 2003) have been developed to identify areas with a higher probability of water presence. Both models have successfully been used in the removal of most misinterpreted water pixels due to shadows and snow (Mueller et al., 2016; Donchyts et al., 2016; Huang et al., 2017; Donchyts, 2018).

2.4 CONCLUSIONS

Recent studies related to the detection of surface water mainly focus on making use of satellite-based optical Earth Observation (EO) sensors. Data provided by Landsat 8 and Sentinel-2 satellites is often consulted, as a result of their relatively high spatio-temporal resolution and spectral band availability. To separate water from background features, water indices are regularly employed due to their effectiveness, and straightforward implementation (e.g. NDWI, MNDWI, AWEI and WI₂₀₁₅). The most problematic issue is that optical remote sensors remain hindered by cloud obstructions, limiting their applicability to favorable weather conditions. Optical EO sensors combined with SAR technology may potentially solve this issue in the future, due to the ability of SAR to penetrate clouds. However, the application of the two data sources in tandem is currently limited due to inconsistent data availability, distinct physical properties that optical and SAR instruments sense, and dissimilar data delivery platforms. Cloudless composite multispectral satellite images are often constructed to avoid cloud obstructions. However, this is in most cases only suitable to detect long-term changes. A recently introduced approach, where surface water is estimated based on multiple cloud-free images, shows great potential towards the estimation of water under cloudy circumstances. However, its applicability to rivers specifically has not been demonstrated. Furthermore, methods introduced over the past years have largely been able to mitigate the negative impact of cloud shadows, hill shadows and snow cover – often misinterpreted as water – by means of additional information, such as the satellite view angle, the position of the sun (solar azimuth and solar zenith), DEMs and specially modified DEMs such as HAND and MrVBF.

3 METHOD

This chapter covers the steps taken to estimate the geometry of a river based on EO satellite imagery. Firstly, the study area is selected (§3.1). Next, the datasets used are briefly described (§3.2). Thereafter, the approach towards the avoidance of image disturbances is explained, and, the steps undertaken to detect the bounds of a river from a cloudy multispectral satellite image are described (§3.3). Subsequently, common remote sensing interpolation techniques are investigated in order to allow for a more accurate representation of the course of a river (§3.4). Thereafter, a method is proposed that allows for the derivation of river widths from a river polygon (§3.5). Lastly, it is shown how this information can be used to exclude potentially undesirable water bodies (§3.6).

3.1 STUDY AREA: TRINITY RIVER, TEXAS, USA

One of the main objectives is that the overall method should ultimately be applicable to more or less any river in the world⁵. Therefore, it would be senseless to limit the research to one specific study area. However, to provide demonstrative evidence, an initial study area has been selected; a small section of the Trinity River located close by Galveston Bay, Texas, USA. The Trinity River is single-threaded, roughly 6 kilometers long, about 100 meters wide and displays a high-degree of sinuosity at the location of interest. Both Landsat 8 and Sentinel-2 satellites offer plentiful cloudless and cloudy satellite images for this specific area. Furthermore, the Trinity River is sufficiently wide that it is detectable by both satellites (the worst-case scenario is a 30×30 meters spatial resolution). Rivers showing signs of braiding or anastomosing characteristics were initially avoided due to their complexity. The initially chosen study area is displayed in Figure 3.1.

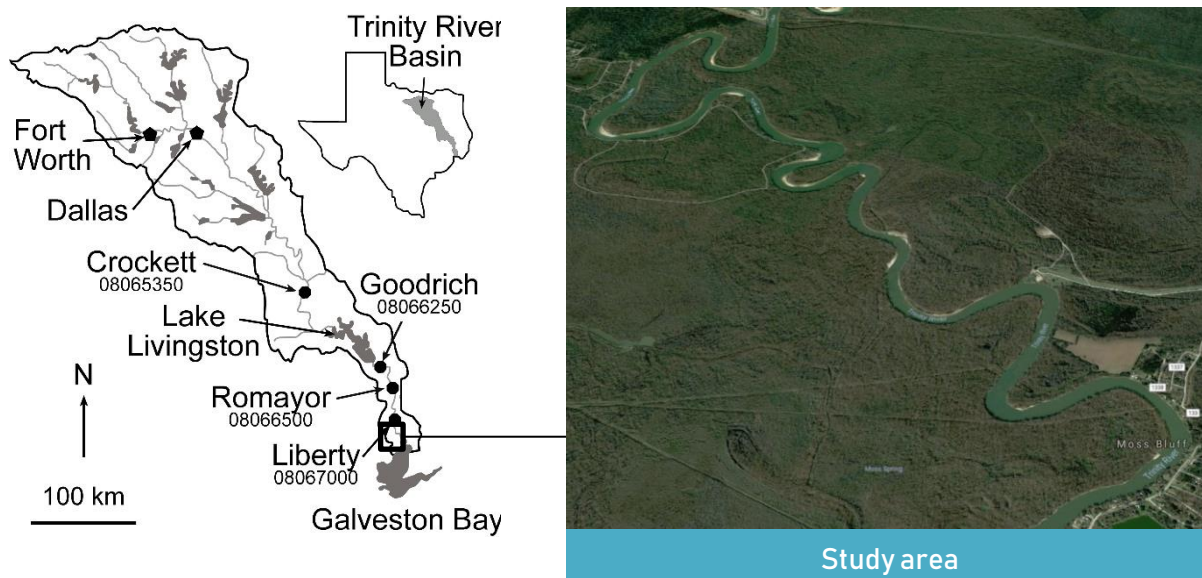


Figure 3.1 – Study area: Trinity River, Texas, USA (Phillips et al., 2004; Map data © 2018 Google).

⁵ (1) Assuming said river is sufficiently wide that it is detectable by either the Landsat 8 or the Sentinel-2 satellite and (2) multispectral satellite images are available.

3.2 DATA RESOURCES

Three raw input datasets were used as a basis in order to generate the water mask from which later river polygons are derived. Two of which are datasets acquired from multispectral satellites: Landsat-8 and the fairly recently launched Sentinel-2. Figure 3.1 provides information that is relevant for both satellites, that is: spatial resolution, revisit interval, data availability and spectral band availability. The combined usage of both satellites provides a relatively high spatial resolution, allowing for the accurate detection of the smaller features of a river. Furthermore, both the relatively low revisit interval and the data availability ensure that sufficient satellite images are available, covering a time span of roughly 5 years (11-02-2013 up to now). The availability of red, green, near-infrared and short-wave infrared bands provide the necessary data to calculate water indices, allowing for the detection of water features from a multispectral satellite image. Specifically, the MNDWI is utilized for its ability to discriminate water from land and is widely regarded as a stable and reliable water index. However, the MNDWI is sensitive to snow and ice, since it makes use of the short-wave infrared band, which is also used to separate snow from clouds (NDSI). Donchyts et al. (2018) shows that a good separation between water and snow/ice can be achieved by using the near-infrared band instead of the short-wave infrared band, which is less sensitive to snow/ice content. In fact, substituting the short-wave infrared band for the near-infrared band results in the NDWI. Therefore, this particular index is used under the presence of snow or ice.

Table 3.1 – Spatial resolution, revisit interval, data availability and number of available bands for Landsat 8 and Sentinel-2 satellites.

Dataset	Type	Spatial resolution (pixel size)	Revisit interval (days)	Data availability	Number of bands
Landsat 8	Multispectral imagery	30 x 30 m	16	April 11, 2013 – now	9
Sentinel-2	Multispectral imagery	10 x 10 m*	5	June 23, 2015 – now	12
HAND	Normalized elevation dataset	30 x 30 m			

*The short-wave infrared channel has a spatial resolution of 20 x 20 meters, which is rescaled to 10 x 10 meters.

Furthermore, the Height Above Nearest Drainage (HAND) 30 meters resolution dataset, which is derived from the Shuttle Radar Topography Mission (SRTM) Digital Elevation Model (DEM), is used as a topographic mask to detect and exclude pixels where potential errors occur due to shadows. Water is often erroneously detected in areas of terrain shadow, because shadows are generally spectrally similar to water, appearing as a scattering of flood pixels in hilly regions. The HAND model is based on a calculated drainage network, from which a nearest drainage map is generated. Each pixel on this map contains an elevation difference with its associated nearest drainage pixel. Therefore, as opposed to DEM, the HAND model is not based on absolute heights, but is the normalized (or relative), local height, defined as the vertical distance from a hillslope surface cell to a nearby drainage cell. A study by Huang et al. (2017) verified that elevation information directly acquired from DEM is sometimes unsuitable for the mapping of surface water and that a HAND model is recommended over DEM for global purposes.

Google Earth Engine (GEE) is used for the analysis and manipulation of the data resources. This is a cloud-based geospatial processing platform that allows for planetary-scale geospatial

analysis, providing access to publicly available remotely sensed imagery and cloud-based computing power.

Although the addition of more data sources such as Landsat 7 or even Open Street Maps were considered, their inclusion was deemed not feasible within the given available amount of time and were thus excluded to narrow down the overall scope.

3.3 AVOIDANCE OF IMAGE DISTURBANCES

Clouds, haze and fog are a common phenomenon in remote sensing imagery and a significant concern for most land surface remote sensing applications. This is especially true for images that have been obtained by means of optical EO satellites, where these types of noise form a severe hindrance and may significantly impact the information that is required to accurately detect water. The method as described by Donchyts et al. (2016) is firstly applied to the study area, allowing for the detection of surface water in an automated manner based on an adaptive thresholding procedure. The surface water detection technique relies on two key algorithms: Otsu thresholding and the Canny edge detector. The essence of the procedure is elaborated in Appendix A. In short: The edges of a surface water body are detected by initially applying the NDWI, followed by a Canny edge detector. Sharp changes (between water and land) are subsequently sampled by buffering (that is, expanding) the detected edges to obtain a bimodal distribution of water and land pixels. Thereafter, a threshold value is obtained by applying Otsu's method, separating water from land. Lastly, the Canny edge detector is applied once more to the resulting surface water mask in order to detect the edges. The final result is depicted in Figure 3.2 (1) and is based on a Landsat 8 image that is completely cloud-free. No adjustments were needed. However, the introduction of image disturbances, such as clouds, appear to be problematic (see Figure 3.2 (2)).

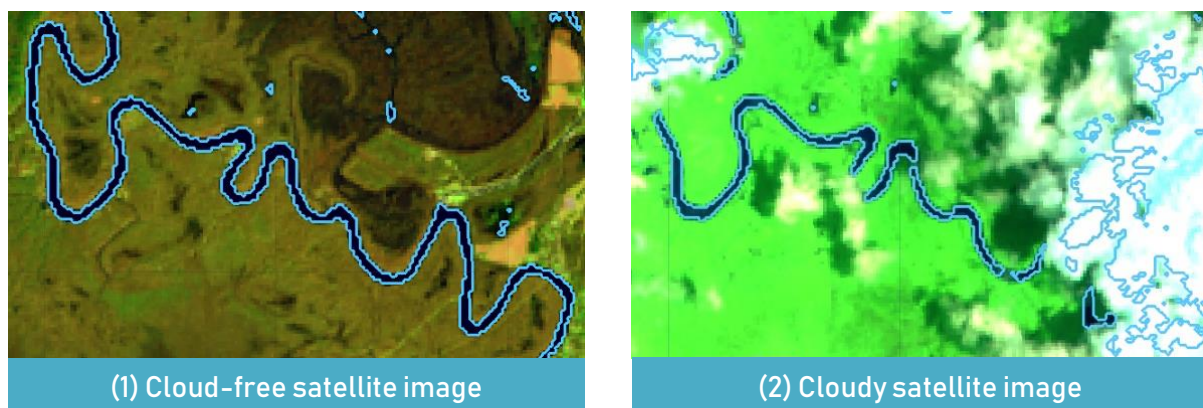


Figure 3.2 – (1) Surface water detection of the Trinity River, Texas, USA based on a cloud-free multispectral satellite image and (2) the exact same method applied to a satellite image that is hindered by clouds (2).

Based on the study of literature, it was found that a recently introduced method by Donchyts (2018) is able to estimate the bounds of a relatively large surface water body under cloudy conditions with a high-degree of accuracy. However, its applicability towards rivers specifically was not demonstrated. Nonetheless, the method shows great potential towards the estimation of the bounds of a river of a cloudy satellite image. For this reason, its applicability towards rivers is further investigated.

The general idea of the approach is to compute an underlying image that stores information of where and how often surface water occurred over time based on a series of cloudless historical images, which is defined as the water occurrence. Here, the frequency at which water occurred at a pixel can be any number between 0 and 1, where 1 means that water has been detected in every sampled image and 0 that water has never been detected. Sampling of historical observations allows for the prediction of a river's course, which enables the possibility of estimating missing data points due to the presence of clouds. For example, a river's course on the first of January, 2017, can be predicted based on a combination of images taken in December, 2016, as well as images taken in February, 2017. As demonstrated by Donchyts (2018), the algorithm performs well for larger-sized water bodies under cloudy conditions. However, minor modifications were found to improve its overall reliability towards the estimation of the course of rivers under cloudy circumstances specifically.

To identify surface water under cloudy circumstances, the algorithm compares the surface area of water that has been detected without any form of cloud-avoidance-procedure to the surface area of water that has been estimated based on historical imagery (referred to as the historical composite from now on). If the differences between their area is found to be large, the historical composite is selected as the most accurate representation of a water body. This is due to the fact that it is very likely that, in this case, a multispectral satellite image is largely, or even completely, obstructed by clouds, which makes it difficult to estimate its bounds. Otherwise, if their difference is relatively small, the multispectral satellite image is likely to be hindered by some form of cloud obstruction, and the originally detected water body is merged with the historical composite. In this scenario, the size of the detected water from the historical composite is reduced by a morphological operation known as erosion⁶. This operation shrinks (erodes) the shape of the detected water body and thus reduces its overall size. This is a common operation within the field of computer vision and works, as essentially any filter, by taking a small grid of numbers (a kernel), which is then passed over the whole image, transforming it based on what those numbers are (see Appendix B for a description of how this works exactly). The historical composite is subsequently merged with the originally detected surface water mask by means of addition. The result is the originally detected water body, where possible missing gaps due to cloud obstructions are estimated using the eroded historical composite.

Although this procedure works well for larger water bodies (e.g. lakes and reservoirs), it does, in its current form, not produce optimal results for rivers. This is largely attributed to the fact that the radius of the kernel, used to erode the bounds, is a fixed value. In Figure 3.3, the procedure is applied to the Trinity River, and the resulting surface water masks are displayed in binary form. Pixels that contain water are assigned the number 1 and pixels that do not contain water are assigned the number 0. By convention, 0 is associated to black, and 1 to white. Here, missing gaps as a result of clouds are estimated and thus "filled" by the historical composite. However, this is done insufficiently so, resulting in an underestimation of the width over the course of the Trinity River (see blue arrows).

⁶ For a more thorough explanation of erosion, as well as other morphological operators used frequently in this thesis, see Appendix B.

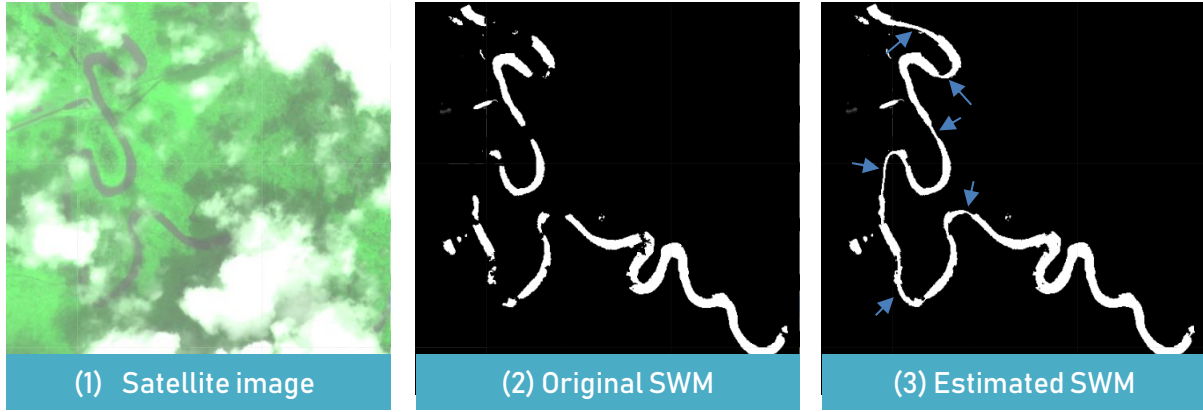


Figure 3.3 – (1) Original satellite image of a section of the Trinity River, (2) automatically detected surface water mask (SWM), (3) estimated surface water mask due to cloud obstructions based on the method described by Donchyts (2018).

To improve the accuracy of the historical composite under cloudy circumstances, for rivers specifically, the proposition is to linearly scale the strength by which the historical composite is eroded, based on the differences between the total surface area of water of the originally detected surface water mask (that is, (2) in Figure 3.3) and the historical composite. Under cloudy circumstances, the total surface area of the historical composite is likely to be larger than the originally detected surface water mask, since the course of a river represented by the historical composite does not contain any gaps. This is true under the assumption that the geometry of a river has not changed significantly within the time window wherein historical images have been sampled. Furthermore, instead of relying on a historical composite that represents the average course of a river over time, weights are attached to the sampled historical images based on the date at which they were sampled, resulting in a historical composite that represents a weighted average. By doing so, the impact of variable discharge patterns towards the geometry of a river can be reduced, depending on the distribution of the weights, resulting in an estimate that is likely to be more in line with the originally detected surface water mask. The new set of rules followed to estimate the course of a river under cloudy circumstances is as follows:

Let $SWM1$ be the detected surface water mask at the current instant in time, $SWM2$ the surface water mask of the historical composite, K a set of real numbers ranging from 1 to 1.5, L a set of real numbers ranging from 0 to 25, ω a kernel filled with 1's (1 represents water), r the radius of the kernel where $\min(L) \leq r \leq \max(L)$, and A_{SWM1} and A_{SWM2} the total surface area of water present in either surface water mask. The estimate of the new surface water mask under cloudy conditions is defined as:

$$SWM_{estimate}(i,j) = SWM1(i,j) + (SWM2(i,j) \ominus \omega) \quad (3.3.1)$$

where the radius r of kernel ω equals:

$$r = \begin{cases} \min(L), & \text{if } A_{ratio} > \max(K) \\ \frac{\min(L) - \max(L)}{\max(K) - \min(K)} (A_{ratio} - \min(K)) + \max(L), & \text{if } \min(K) < A_{ratio} < \max(K) \\ \max(L), & \text{if } A_{ratio} < \min(K) \end{cases}$$

with A_{ratio} defined as $A_{ratio} = \frac{A_{SWM2}}{A_{SWM1}}$.

In other words, the surface water mask at the current instant in time and the surface water mask of the historical composite are now always merged by means of addition. However, the influence of the historical composite towards the originally detected surface water mask depends on the difference between the total surface area of both surface water masks. In case it is found that the course of a river varies highly over time, and $A_{ratio} > \max(K)$ is true, an option is provided to instead select the historical composite as a best estimate. However, this was found to be highly unlikely.

The distribution between A_{ratio} and the kernel radius r is demonstrated in Figure 3.4 (left). The maximum kernel radius by which a river is eroded is limited at 25, since a radius that is too big is found to excessively erode the surface water mask of the historical composite, especially for rivers that are relatively narrow (<100 meters wide). In chapter 5, the sensitivity of various kernel radii is demonstrated. The sensitivity of K for various maxima of the defined set of real values is also shown (that is, 1.5, 2, 3 and 5 as seen in Figure 3.4).

Furthermore, a simple inverse distance weighting function as defined by Shepard (1968) is used in order to reduce the impact of sampled images that are relatively far off the considered point in time:

$$f(I) = \frac{\sum_{i=1}^n w_i z_i(x, y)}{\sum_{i=1}^n w_i}, \quad w_i = \frac{1}{|d(x, x_i)|^p} \quad (3.3.2)$$

where images further off from the reference image I will have lower weights, z_i is the value at a pixel within an image, w_i is the weight (rescaled to [0-1]) by which values of a sampled image are multiplied, d is the time in milliseconds from the sampled date x to the considered date of interest x_i , and p a positive real number, which defines the shape of the distribution by which sampled images are weighted. Various values can be used for p (e.g. Figure 3.4 (right)), depending on the variability of the geometry of a river over time. A distribution with $p = 0.1$ is assumed for the weights attached to the sampled images. The sensitivity of the historical composite towards various values for p is later demonstrated in chapter 5.

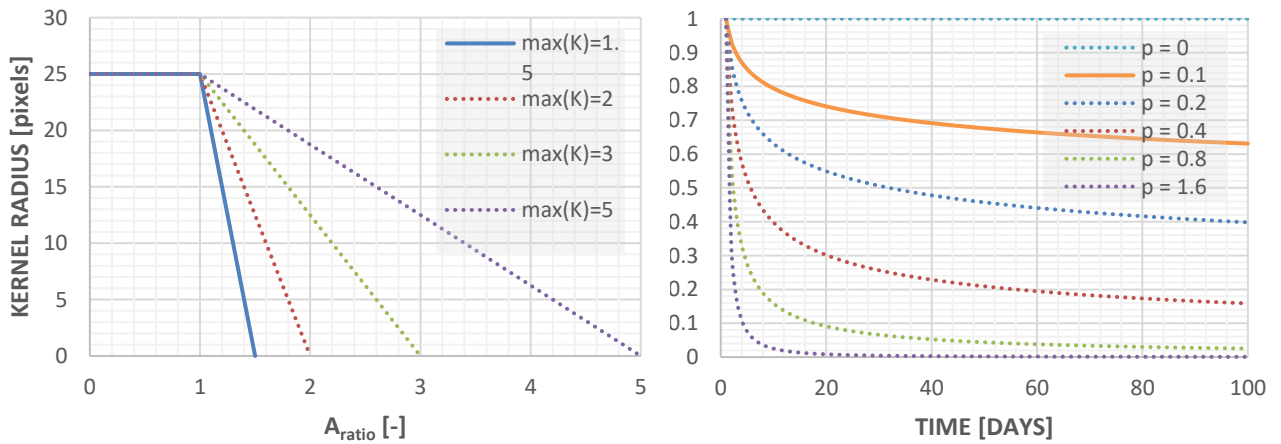


Figure 3.4 – The relationship between A_{ratio} and the kernel radius r (left) as well as an example of various distributions for the assigned weights (right).

The result of the modified procedure for the exact same moment in time as seen in Figure 3.3 is presented in Figure 3.5. Differences between the original estimation and the modified procedure can clearly be observed.

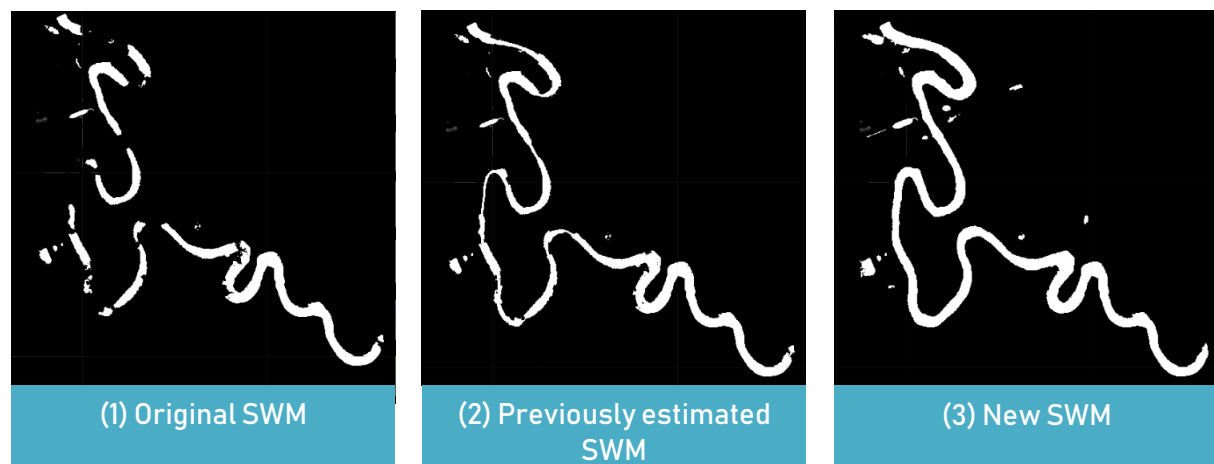


Figure 3.5 – (1) Original surface water mask, (2) previously estimated surface water mask and the (3) new estimation of the water mask, which is obtained by linearly scaling the erosion between the surface area of the historical composite and the originally detected image and applying weights to sampled historical images.

The overall approach towards the estimation of the course of a river under cloudy circumstances is now as follows. Firstly, the MNDWI is calculated to enhance open water features while efficiently suppressing background noise. Additionally, the HAND dataset is used to exclude pixels that may result in potential errors due to shadows. Afterwards, the method described by Donchyts et al. (2016) is applied to generate a surface water mask in an automated manner, based on Otsu thresholding. The result is a binary image, where pixels that contain water are assigned the number 1 and pixels that do not contain water are assigned the number 0. Clouds have not been removed as of yet, and thus a significant number of pixels (white) are incorrectly classified as water. The first three steps are illustrated in Figure 3.6.

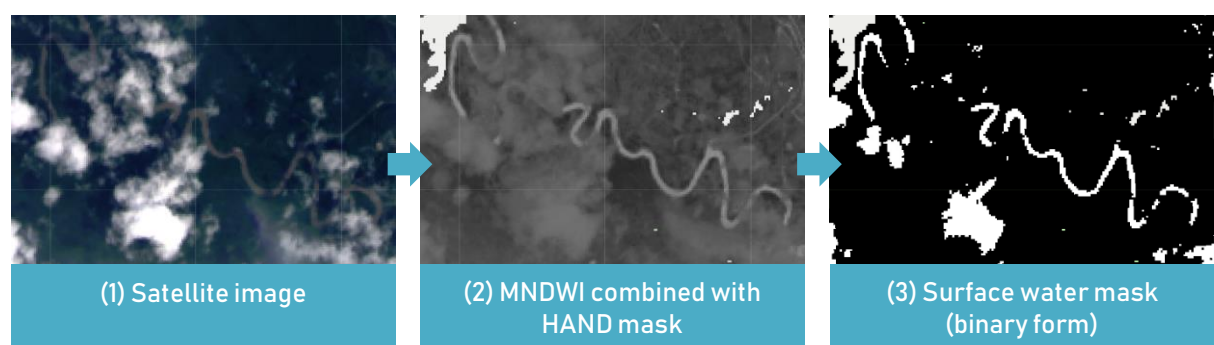


Figure 3.6 – The generation of a surface water mask in an automated manner: (1) multispectral satellite image, (2) calculate the MNDWI and exclude pixels that may result in potential errors due to shadows or snow through the utilization of HAND, (3) apply Otsu thresholding to generate a surface water mask.

Subsequently, the water occurrence composite based on historical data is generated. In order to do so, multispectral satellite images that are below a certain threshold value in terms of cloud coverage are filtered from the Landsat 8 and Sentinel-2 satellite databases. A percentage that is roughly equal or less than 15 was found to, generally, provide a relatively accurate representation of the course of a river. This percentage ensures that several images are considered in case of a

relatively short sampling window (e.g. 1 month). However, in case plenty cloud-free images are available, this may be lowered to 10, or even 5, to assure only perfectly cloudless images are used to sample from, improving the estimate.

Thereafter, for every historical image, a surface water mask is computed, resulting in a series of binary images. This is done by repeating (1), (2) and (3) as seen in Figure 3.6, but for the series of mostly cloudless sampled historical images. Thereafter, the binary images are summed and, divided over the total number of binary images, resulting in a composite image displaying the frequency of water over time, where each pixel is assigned a value between 0 and 1 as a result. Areas that inundate every so often, or clouds that have falsely been detected as water and are therefore not considered to be part of the main river course, can then be eliminated based on their low occurrence frequency. Due to the fact that the water occurrence composite is based on multiple historical satellite images, the frequency of which water occurs at a pixel is detectable. Relatively low values between 0 and 1 indicate that water has not occurred very frequently, meaning that it is likely to be the result of either a short-term flood or a misinterpreted cloud. A threshold value of 0.2 was found to, generally, exclude most of the misinterpreted pixels due to clouds, or water as a result of short-termed floods. This effectively means that every value that is equal or less than 0.2 is converted to 0 (black). In chapter 5, the sensitivity of this particular threshold value is demonstrated. The detection of water of multiple historical images, the water occurrence composite before the application of a threshold value, and the final water occurrence composite are illustrated in Figure 3.7.

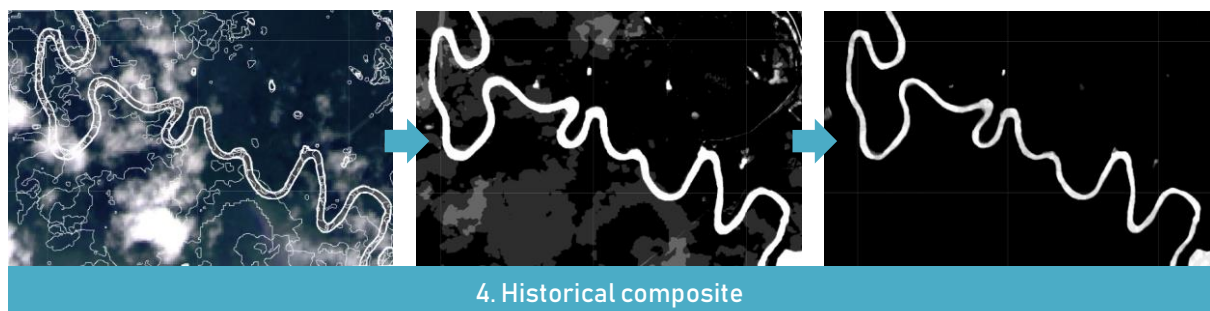


Figure 3.7 – The generation of a historical composite: (1) sample relatively cloudless multispectral satellite images and compute their surface water masks based on the procedure as seen in Figure 3.5, (2) construct the average course of a river of interest by summing all binary images and dividing the values of all pixels by the total amount of images, (3) eliminate all pixels of that are below a predefined threshold value.

From there on, both the surface water mask (3) and the historical composite (4) are combined by means of multiplication. This means that pixels that have originally been assigned the value of water, 1, are indeed water in case they are multiplied by a positive value. Pixels that have originally been assigned the value of water but are multiplied by 0, are most likely clouds that mistakenly have been detected as water due to their similar spectral properties. The result is illustrated in Figure 3.8 (5). Subsequently, the historical composite is merged with the newly obtained surface water mask (as seen in 5), and possible overestimations of the historical composite, relative to the originally detected surface water mask, are eroded in an adaptive manner. This is done by calculating the difference between the originally detected surface water mask (5) and the historical composite (4), followed by the application of erosion (see Appendix B), based on the value for A_{ratio} .

Lastly, the edges are detected by means of the Canny edge detector. This is done for visualization purposes, as the surface water mask is in fact all that is needed to determine the surface river widths, which is demonstrated in §3.5.

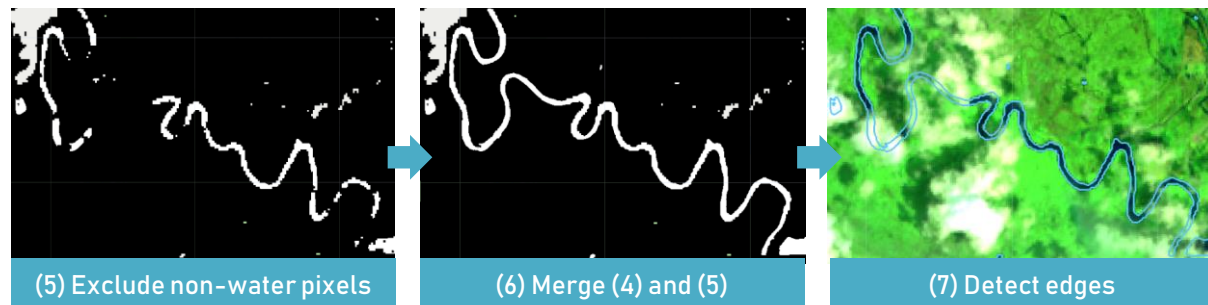


Figure 3.8—The detection of a river’s edges: (5) removal of falsely detected water pixels, (6) merge the detected water mask and the historical composite, (7) compute the edges by means of the Canny edge detector.

3.4 CONVERSION TO A RIVER POLYGON AND SPATIAL INTERPOLATION METHODS

In the previous segment it is demonstrated how the course of a river under cloudy circumstances can be estimated using multiple images from the past, in the form of a binary surface water mask. However, the obtained data is currently not represented in the desired spatial format. Geospatial data can be represented in two formats, either in the form of a raster or a vector (Burrough, 1986). Raster data is based on a matrix of grid cells of uniform size and is especially suitable for capturing, storing and analyzing data, such as the elevation, land use or temperature. Vector data is comprised of coded points (vertices) and lines and is excellent for capturing and storing spatial details, such as the edges of features, in this case rivers. Multispectral satellite data is represented in raster format, where each pixel represents the reflectance across multiple wavelengths within the electromagnetic spectrum (bands). Google Earth Engine provides a built-in algorithm, which is able to convert the raster data of an image to vector data, based on homogeneous regions. This allows for the conversion of the final surface water mask ((6) in Figure 3.7) to a vector format, which indeed consists of a homogeneous form after the removal of non-water (black) pixels. Although this method certainly works, a disadvantage is that it remains unclear how it exactly is implemented, leaving room for potential unexplainable errors. Since the direct access to the source code of GEE is not permitted, the exact implementation remains unknown. However, there is a good chance that it is based off of work by Riekert (1993), where an algorithm is proposed allowing for the extraction of area objects from raster image data. Or, work by Lou et al. (2005), where a popular approach to vectorization of remote sensing images is presented based on the characteristics of raster data.

Immediate conversion from raster data to vector data will not lead to the desired polygon, because of the fact that data is drawn from multispectral satellite images containing pixels with a resolution of 30×30 meters, resulting in blocky polygons having the same pixel size (in case of Sentinel-2’s 10×10 spatial resolution, the edges remain visibly jagged). In computer graphics and digital imaging, a common technique is resampling, allowing for the direct manipulation of a digital image, transforming it to another form. In this particular case, the reason is to create more vertices, allowing for a more accurate representation of the course of a river. This is of importance, since the river widths are later (§3.5) derived from the shape of the river polygon.

In the processing of satellite imagery, there are three common resampling techniques: nearest-neighbor interpolation, bilinear interpolation and bicubic interpolation. In terms of functionality, the main differences between the three techniques is that nearest-neighbor interpolation bases the new value for a pixel on the value of the nearest pixel, bilinear interpolation assigns the output pixel value by taking the weighted average (distance based) of the four nearest neighbors and bicubic interpolation does the same, but for 16 nearest neighbors and takes the gradient (or orientation) into account. The latter usually results in the smoothest edges. The trade-off is that bicubic interpolation is much slower in terms of computation speed compared to nearest-neighbor interpolation. This is demonstrated in Appendix E by means of profiling the script, which is a tool that helps to identify bottlenecks by providing information about the CPU and memory usage. In §4.2 it is shown that the performance of the script is in fact of great importance, limiting the maximum size of the river polygon that can be rendered. In Google Earth Engine, nearest-neighbor is implemented by default when satellite data is projected on the map, therefore it is not necessary to discuss this technique. The effect of both bilinear and bicubic interpolation are explored, where the governing equations of bilinear and bicubic interpolation can be defined as

$$f(x, y) = \sum_{i=0}^1 \sum_{j=0}^1 a_{ij} x^i y^j = a_{00} + a_{10}x + a_{01}y + a_{11}xy \quad (3.3.1)$$

$$f(x, y) = \sum_{i=0}^3 \sum_{j=0}^3 a_{ij} x^i y^j \quad (3.3.2)$$

where x and y are the coordinates of a new location, $f(x, y)$ the value of the pixel and a_{ij} the coefficients. Furthermore, $a_{00} = f(0,0)$, $a_{10} = f(1,0) - f(0,0)$, $a_{01} = f(0,1) - f(0,0)$ and $a_{11} = f(1,1) + f(0,0) - (f(1,0) + f(0,1))$, assuming the known four corners are $(0,0)$, $(1,0)$, $(0,1)$ and $(1,1)$. The result of raster to vector conversion (R2V), as well as the application of both interpolation methods are shown in Figure 3.9, including a depiction of the smoothness of the edges for each approach. Here, Landsat 8 data serves as a basis. Clear differences are visible between the images, although the differences between bilinear and bicubic interpolation are relatively minor. Bicubic interpolation shows the most accurate edges.

To reduce the number of vertices and optimize the polygon, it is then simplified. This is based on the Douglas-Peucker algorithm (Douglas and Peucker, 1973). Consider a set of points (P_0, \dots, P_n) on a piecewise linear curve. The algorithm firstly connects the start (P_0) and end points (P_{end}) with a straight line. It then computes the distance of all intermediate vertices perpendicular to the straight line. The vertex that is the furthest away from the line of which the distance is larger than a prespecified threshold value, is marked and added to the simplification. This means that simplified line now connects P_0 to P_{new} and P_{new} to P_{end} . The process is repeated, but now for all vertices between P_0 and P_{new} , as well as P_{new} and P_{end} , until no more vertices of the original curve are available of which the distance is greater than the prespecified threshold value.

Furthermore, the effect of bicubic interpolation using a Sentinel-2 multispectral satellite image is demonstrated in Figure 3.10. The resulting polygon using the Sentinel-2 dataset appears to produce slightly more accurate results based on visual interpretation. Images (5) in Figure 3.9 and image (2) in Figure 3.10 are not repeated for bilinear interpolation, since they are, in fact, more or less similar.

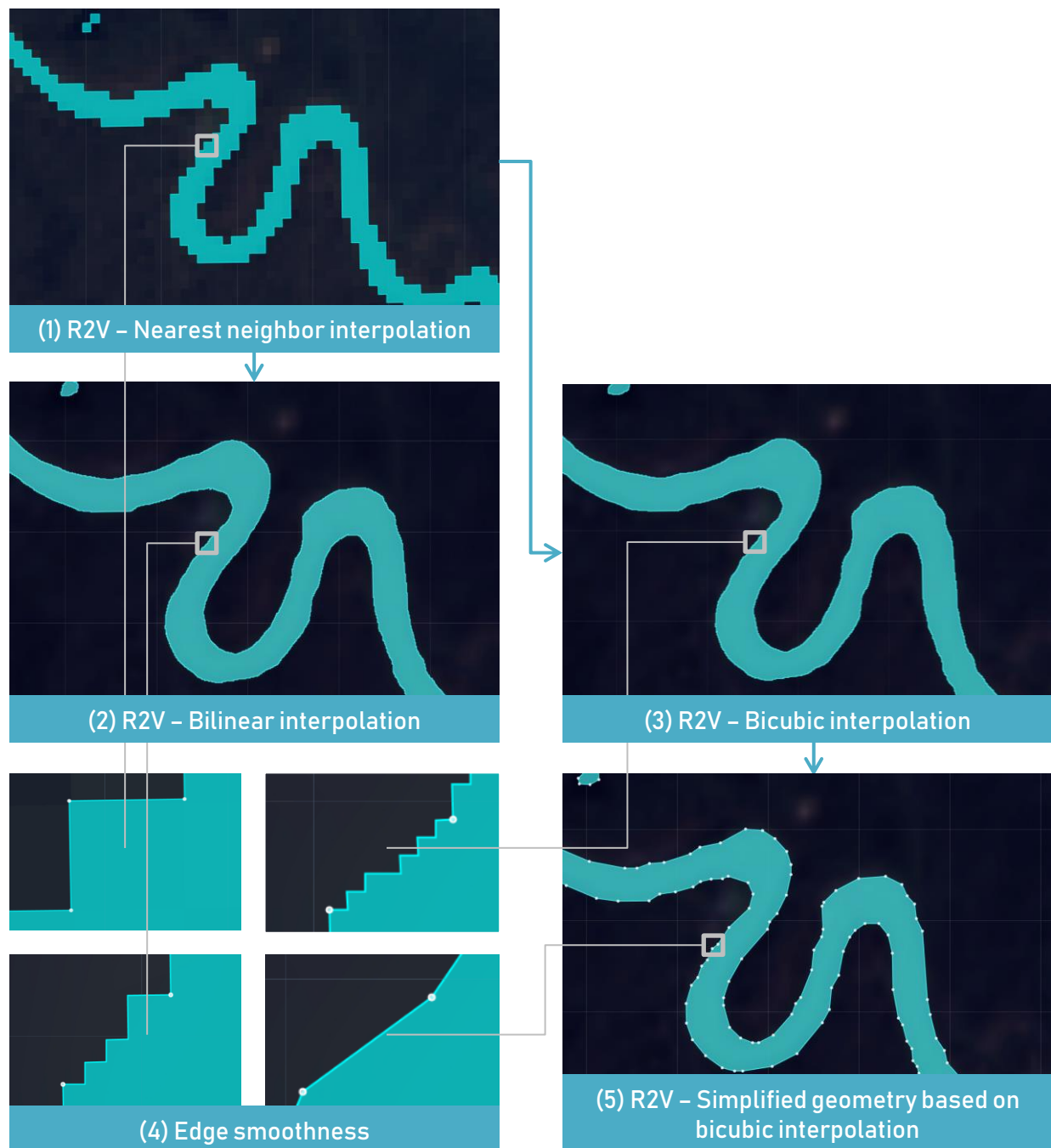


Figure 3.9 – Overview of the effect of raster to vector conversion (R2V) for bilinear and bicubic interpolation, based on Landsat 8 multispectral satellite data. The following images are displayed: (1) R2V without any sort of interpolation applied, (2) application of bilinear interpolation on (1), (3) application of bicubic interpolation on (1), (4) zoomed-in view of the result of both interpolation methods, (5) simplified geometry based on bicubic interpolation for optimization purposes.

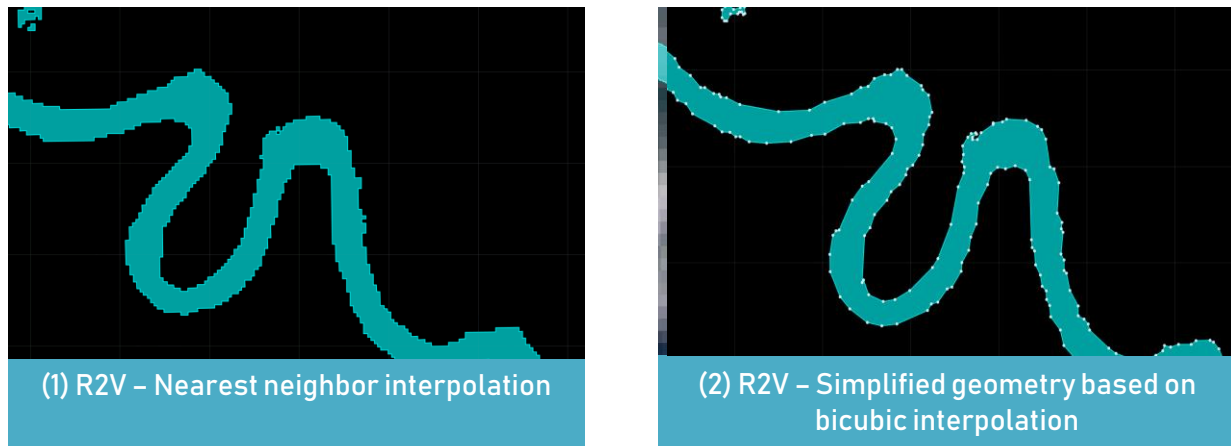


Figure 3.10 – Overview of the effect of R2V conversion for bicubic interpolation, based on Sentinel-2 satellite data. The following images are displayed: (1) R2V without any sort of interpolation applied, (2) simplified geometry based on bicubic interpolation.

3.5 DERIVATION RIVER WIDTHS

The purpose of a river polygon is that it provides information about the course of a river. However, a river polygon does not provide direct information about its width. Based on existing concepts, a method is implemented that allows for the derivation of the river width from a river polygon, in an automated manner. The method consists of three main steps:

1. Euclidian distance map (EDM);
2. Centerline (Voronoi-based skeletonization followed by skeleton pruning);
3. River widths.

However, before doing so, a preprocessing step is applied—that is, relatively small water bodies that are present within the multispectral satellite image, thus disconnected from the main river of interest, are removed. To do so, morphological opening is applied. This is a variation on morphological erosion, as previously seen in §3.2, and is defined as erosion followed by dilation. Opening first shrinks (erodes) the shape of a detected water body, reducing its overall size, and subsequently enlarges (dilates) the detected water body. The whole point of the operation is to first apply erosion to such an extent that relatively small water bodies are completely removed. Since this operation affects the whole image, and thus the river of interest, this is followed by dilation to restore the river to its original size. Furthermore, as a result of dilation, small gaps which have been overlooked by the surface water detection algorithm are filled, improving the result. A typical kernel filled with 1's (water pixel representation) is used to apply the operation. The result of the opening operation is depicted in Figure 3.11. Due to the fact that the current study area does not show a significant amount of water bodies surrounding the Trinity River, the operation is applied to a more fitting location: a segment of the Waal nearby Nijmegen, located in The Netherlands. This particular location contains a vast amount of water bodies, of various sizes and shapes, surrounding the Waal and thus makes the impact of the operation more noticeable. Note that there is a slight gap in the Waal (bottom right corner), which is the result of a bridge crossing the river. For relatively high resolutions (e.g. 10×10 meters), this is an unsolved issue as the river polygon is either split in two or remains connected (simply due to the fact that a 30×30 meters resolution does not detect the bridge).

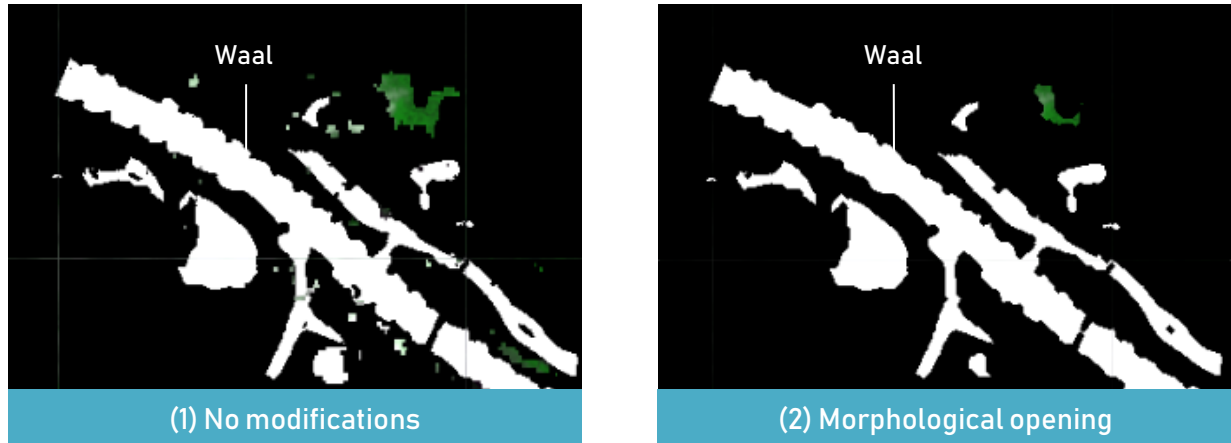


Figure 3.11 – Comparison of two binary images, demonstrating the effect of the opening operator on the Waal including its neighboring water bodies.

Secondly, the distance transform is computed in Euclidian space, and is generally used to compute medial axes, Voronoi diagrams, shortest-path computation and image segmentation (Fabbri et al., 2008). The distance transform is an operator that computes the distance of each pixel to the nearest obstacle pixel and is ultimately based on the Euclidean distance given by:

$$d(p, q) = \sqrt{(p_x - q_x)^2 + (p_y - q_y)^2} \quad (3.5.1)$$

where d is the distance from point p to point q . In this case, the distance transform is obtained based on a set of boundary points, resulting in a distance map where each pixel contains the distance value to the closest boundary point. Therefore, more boundary points directly relates to a more accurate distance map. Since the overall computation speed is of importance, a generally high-performant approach to the Euclidean Distance Transform (EDT) by Meijster (2004) has been used to compute the distance per pixel, denoted as:

$$EDT(x, y) = \min\{(x - i)^2 + G(i, y)\} \quad (3.5.2)$$

$$G(i, y) = \min\{(y - j)^2 \mid F(i, y) = 0\} \quad (3.5.3)$$

where given an input image F , the distance transform is firstly calculated for each column of pixels by performing a forward scan (top-to-bottom) followed by a backward scan, generating the image G . Secondly, the algorithm iterates through each row, from left to right and vice versa, calculating the minimum distance value for each pixel. The result of the EDT applied to a segment of the Trinity River is presented in Figure 3.12 (1) in the form of a gradient, where the distance of each pixel to the nearest boundary of each polygon is illustrated by its color. Here, a pixel that is farther away from the boundary is colored white.

Next, the medial axis of a polygon, also known as the skeleton, is computed based on the distance map. To do so, a Voronoi diagram is firstly generated based on a two-dimensional convolution between the distance map and a Laplacian-8-edge-detection structural element. This is based on work by Brandt et al. (1992). Let $I(x, y)$ be the image of the distance map and let $f(x, y)$ be the structural element. Then the discrete 2D convolution is

$$(I * f)(x, y) = \sum_{u=-k}^k \sum_{v=-k}^k I(x - u, y - v) f(u, v) \quad (3.5.4)$$

where $(I * f)$ is the resulting image, k the overall boundary conditions, $*$ the convolution operator and f the Laplacian-8-edge-detection structural element.

Subsequently, a skeleton can be computed based off of the computed Voronoi diagram. Since a Voronoi diagram consists of convex polygons, which in turn consist of vertices, vertices of convex polygons that intersect with the original boundary of the Voronoi diagram (in other words, the boundary of the detected surface water body) are discarded, resulting in a skeleton (Figure 3.12 (2)). Although there are various ways to compute a skeleton of a geometry (Tagliasacchi et al. (2016) provides an extensive overview of state-of-the-art approaches), the Voronoi-based approach was implemented since it can be computed relatively quickly.

In the current form, the resulting skeleton contains undesirable branches as a result of the Voronoi-based approach, known as spurious branches. In order to remove the spurious branches in an automated manner, or, prune the skeleton, an approach by Solís Montero et al. (2012) has been implemented. The essence of the algorithm is quite straightforward and ultimately comes down to the following equation:

$$|e_p - b_p| \leq s \times |f - b_p| \quad (3.5.5)$$

where b_p is a branch point (a vertex on a skeleton where two or more lines meet), e_p an end point of a branch (connected to only one line), s an arbitrary scale multiplier and f the closest boundary point relative to b_p . The pruning criterion is as follows: Consider a branch of the skeleton $\{b_p, \dots, e_p\}$ with branch point b_p and end point e_p such that line between both points is not interrupted by other branch points. The branch $\{b_p, \dots, e_p\}$ is marked for removal if the end point e_p lies inside of a circle that is centered around the nearest boundary point b_p , with a radius that is equal to the Euclidean distance $|f - b_p|$. The process is re-iterated until no more branches can be removed. In regard to D-RATIN – in some cases, the end-user may want to exclude relatively large branches that are not removed by default. Therefore, a scale factor s is introduced, which allows for the amplification of the search radius. By default, the scale multiplier is set to 1.

An overview of the three steps applied to the Trinity River is demonstrated in Figure 3.12. Here, the EDT is first shown. This is followed by the resulting Voronoi skeleton as well as the centerline, which was obtained by pruning the undesirable branches of the skeleton.

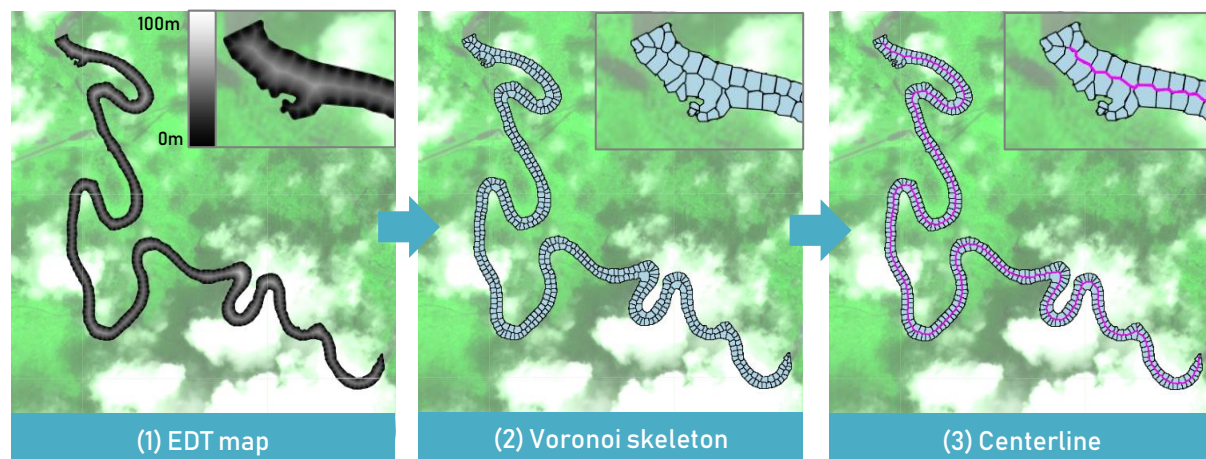


Figure 3.12 – Overview of the generation of a pruned skeleton: (1) EDM (a pixel that is farther away from a boundary point is colored white), (2) Voronoi skeleton, (3) centerline (purple).

Information about the width of a river polygon can now be determined as follows. Firstly, the resulting centerline is masked (overlapped) by values of the EDM. This results in a centerline where every pixel contains information about its distance to the nearest boundary, in Euclidian space. Subsequently, the resulting values are multiplied by two in order to obtain the river width, instead of the distance from the boundary to the center. The final result is demonstrated in Figure 3.13. Here, the river polygon of a segment of the Trinity River is displayed including its width by means of a centerline (left). The color gradient provides information about the width. Furthermore, the width of the Trinity River is displayed over its course (right). The river length starts at zero in the bottom right corner of Figure 3.13 (left).

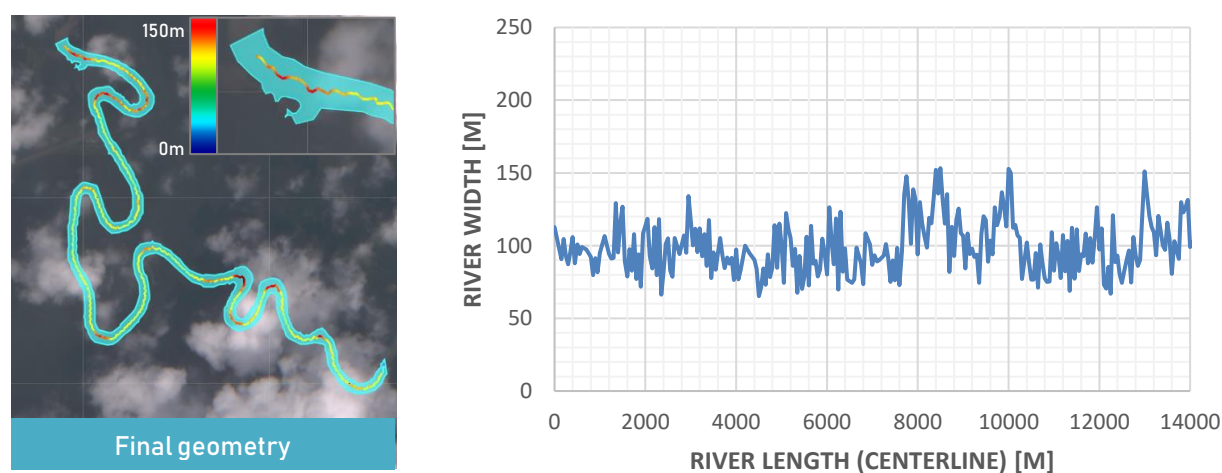


Figure 3.13 – Final estimation of the geometry of a segment of the Trinity River.

3.6 EXCLUSION OF SURFACE WATER

One of the current issues in terms of surface water detection based on a multispectral satellite image is that for every single pixel within an image the water content is computed, based on the utilization of a spectral index (in this case, the MNDWI). This means that, when the data is converted to a vector format, every water body, regardless of its size, will be included in the polygon. In order for the D-RATIN tool to provide quantitative information regarding geometrical, hydrological and geographical river aspects, the first step is to reconstruct the bed-

levels of a river of interest. This requires the river polygon to exclude surface water data that may not be relevant, such as a nearby lake or pond.

To exclude any surface water body that is not part of a river of interest, polygons are computed for every surface water body that is present within a multispectral satellite image. Subsequently, their mean widths are calculated based on the exact same approach as seen in §3.5. Polygons that do not fall within a user-specified width-threshold are excluded (e.g. only display water bodies of which the river width is between 100 and 150 meters). This approach only fails if another water body has the exact same width as a specific river of interest. Alternatively, another option to exclude water bodies that are not part of a river of interest is to only display the water body that contains the greatest number of vertices, or surface area. In terms of script performance, which is found to ultimately limit the maximum size of a river polygon (§4.2), this approach requires much less resources, since the width does not have to be computed for every water body within an image. Another advantage is that this particular approach operates in an automated manner. Since the overall area of interest is based on a user-defined custom shape, water bodies that may be larger than a river of interest can simply be excluded and will therefore not be detected in the first place.

The remaining issue is that the method as described above does not exclude surface water that is part of a river of interest, such as a nearby harbor, or, any other segment or branch of a river of which the bathymetry may not be of importance. A simple geometry subtraction is proposed, allowing for the removal of any segment of a water body by manually drawing a custom shape at the desired location.

In Figure 3.14, the removal of surface water within a multispectral satellite image is illustrated. As a result of the lack of water bodies surrounding the Trinity River, a segment of the Waal is once again illustrated for demonstrational purposes. Firstly, water bodies that are not part of the Waal are excluded. This can either be achieved by defining a width-threshold, or by defining the area of interest in such a way that the Waal contains the largest surface area/most vertices within an image. Furthermore, surface water that may not be relevant to the river bathymetry is excluded by defining two custom shapes (red).



Figure 3.14 – Demonstration of the exclusion of surface water for a segment of the Waal.

4 RESULTS AND EVALUATION

In this chapter, the method as discussed in chapter 3 is applied to two study cases in order to validate its accuracy. The results are interpreted and evaluated. To do so, two study cases are selected based on river polygon data provided by Rijkswaterstaat; a segment of the Meuse and the Rhine, dated from 1995. These are in fact the river polygons that are used to date. Both river polygons were created based on geographical map information and are therefore assumed to be valid in terms of accuracy. Surface areas of river polygons that are generated in an automated manner by means of EO satellite data are compared to the surface areas of river polygons by Rijkswaterstaat. Furthermore, the river widths are compared. Although the river widths were not provided by Rijkswaterstaat, the approach as demonstrated in §3.5 is applied to derive them.

Quite recently, Allan and Pavelsky (2018) built a database consisting of the global river widths from Landsat (GRWL) imagery to characterize the global coverage of rivers and streams, based on mean discharge data. To further validate the approach as presented in this thesis, the EO satellite-based river polygons are compared to the surface water masks of the GRWL database. Additionally, the river widths are compared. This is done for the same segments of the Meuse and the Rhine as previously mentioned. Although their dataset was also composed based on the usage of multispectral satellite imagery, relevant datasets that contain information about both the course and width of rivers seem to be scarce, and the recent advancements in terms of remote sensing applications allow for this kind of data to be obtained in an effective manner.

Furthermore, the global applicability of the approach as described in chapter 3 is assessed by generating river polygons for a total of seven rivers around the world, each displaying various features (e.g. meandering, braiding, islands and varying sizes) (§4.2). This allows for the overall limitations to be assessed.

4.1 VALIDATION

Two river polygons of the Meuse and the Rhine dating from 1995 were provided by Rijkswaterstaat for comparison. A randomly selected segment for both river polygons is chosen. The river geometry is compared to the EO satellite-derived river polygons. Due to the fact that rivers are dynamic by nature, this is done for four instances in time throughout 2016, in order to account for possible variations. EO satellite data is therefore sampled on the first of March, June, September and December. In case EO satellite is not available on one of the aforementioned dates, the most recent satellite image relative to the specific date of interest is selected. The comparison between the river polygons is done for a set of images that are considered to be cloudless—that is, satellite images of which less than 15% of the image is obstructed by clouds—and a set of images that are considered to be cloudy ($\geq 15\%$ is obstructed by clouds). For cloudy images, a period of 4 months was selected to generate the historical composite. First, the overall shape, the surface areas and the mean river widths of the river polygons are compared for the selected segment of the Meuse. This is demonstrated in Figure 4.1, as well as Table 4.1 and 4.2. Figure 4.1 demonstrates the typical representation of the EO satellite-based river polygons (cyan), as well as the river polygons provided by Rijkswaterstaat (orange), under both cloudless and cloudy circumstances. In order to present a clear visualization of both polygons, the decision was made to cut the river polygons in half, diagonally. Since both river polygons show a high degree of

similarity, differences between the two are hardly noticeable if they are overlapping⁷. The corresponding surface areas and mean river widths acquired at four instances throughout 2016 is presented in Tables 4.1. and 4.2. The data has been sampled for the same segment of the Meuse as seen in Figure 4.1. From a visual perspective, the shapes of the EO satellite-based river polygons show a high degree of similarity compared to the river polygon provided by Rijkswaterstaat. The results show that, for relatively cloudless images, the total surface area of the EO satellite-based river polygons deviate between +1.21% and -0.95% from its reference case—that is, the river polygon from 1995. The mean river widths deviate between +1.53% and -1.53% from its reference case (+2 and -2 meters respectively). For cloudy images, the surface areas appear to deviate between +1.24% and -3.61%. Here, the mean river widths deviate between +0.76% and -6.11% from its reference case (+1 and -8 meters respectively).

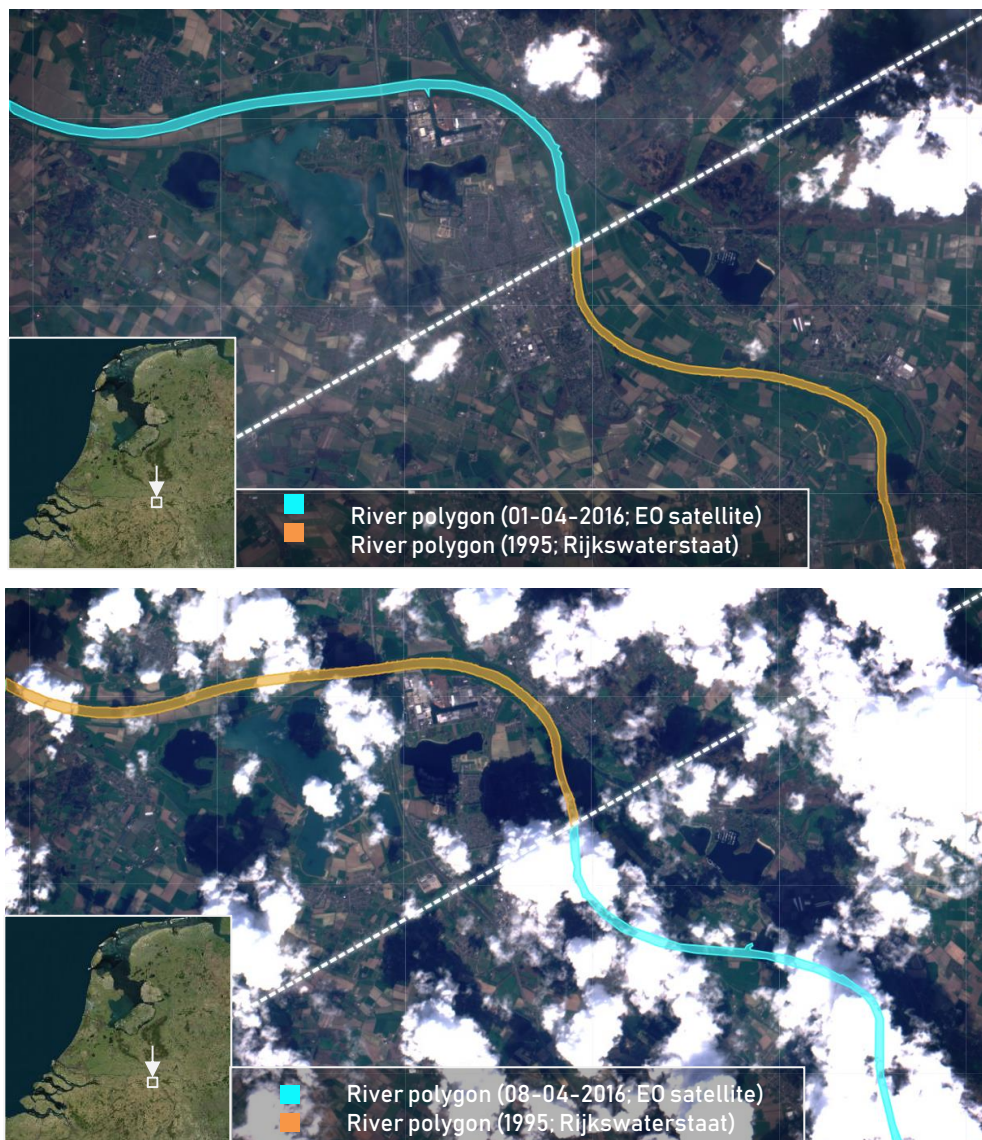


Figure 4.1 – Differences between an automatically generated river polygon (cyan) and a river polygon provided by Rijkswaterstaat (orange) for a segment of the Meuse, for both cloudless and cloudy satellite images.

⁷ However, for the sake of completeness, these images can be found in Appendix C.

Table 4.1 – Comparison between the total surface area and mean river width of various river polygons of a segment of the Meuse throughout 2016, based on fairly cloudless EO satellite images (< 15%cloud coverage), as well as the river polygon provided by Rijkswaterstaat (1995).

River polygon origin	Date [dd-mm-yyyy]	Total surface area [m ²]	Relative difference [%]	Mean river width [m]	Relative difference [%]
Rijkswaterstaat	1995	2,651,233	-	131	-
EO satellite	12-03-2016	2,626,116	-0.95	129	-1.53
EO satellite	20-07-2016	2,683,329	+1.21	133	1.53
EO satellite	08-09-2016	2,627,686	-0.89	128	-2.29
EO satellite	04-12-2016	2,662,584	+0.43	131	0.00

Table 4.2 – Comparison between the total surface area and mean river width of various river polygons of a segment of the Meuse throughout 2016, based on cloudy EO satellite images (\geq 15%cloud coverage), as well as the river polygon provided by Rijkswaterstaat (1995).

River polygon origin	Date [dd-mm-yyyy]	Total surface area [m ²]	Relative difference [%]	Mean river width [m]	Relative difference [%]
Rijkswaterstaat	1995	2,651,233	-	131	-
EO satellite	09-03-2016	2,610,012	-1.55	129	-1.53
EO satellite	07-06-2016	2,684,147	+1.24	132	0.76
EO satellite	05-09-2016	2,655,368	+0.16	131	0.00
EO satellite	14-12-2016	2,555,594	-3.61	123	-6.11

To further assess the correctness of the width of the EO satellite-based river polygons, the GRWL dataset by Allan and Pavelsky (2018) is consulted. The river widths of both cloudless and cloudy images are compared to the GRWL dataset. Due to the fact that GRWL dataset relies on mean discharges, the mean discharges of the Meuse and the Rhine were determined based on gauging stations close by the locations of interest, based on data between 01-01-2000 and 01-01-2018. The data was retrieved from the Directorate-General for Public Works and Water Management⁸. A randomly selected date where the discharge roughly matched the average discharge was selected for comparison.

The mean discharge for the selected segment of the Meuse was found to be \sim 260 m³/s at a gauge station nearby Megen. To further assess the validity of the approach as presented in §3.5, both a cloudless and cloudy multispectral satellite image were sampled on dates where the discharge is relatively close to \sim 260 m³/s—that is, on 02-11-2017 (\sim 215 m³/s) and 17-11-2017 (\sim 247 m³/s).

In Figures 4.2 and 4.3, for both the cloudless and cloudy multispectral satellite images, river polygons are shown including their centerlines, as well as the surface water mask sourced from the GRWL dataset. In Figure 4.4, the computed river widths are compared to both the GRWL dataset as well as the river polygon provided by Rijkswaterstaat. Here, branches are excluded for the sake of direct comparison. Furthermore, data is sampled every 10 meters. In Figure 4.2, “start” and “end” denote the length over which the river width is sampled.

⁸ https://waterinfo.rws.nl/#!/kaart/Afvoer/Debiet__200ppervlaktewater__20m3__2Fs/

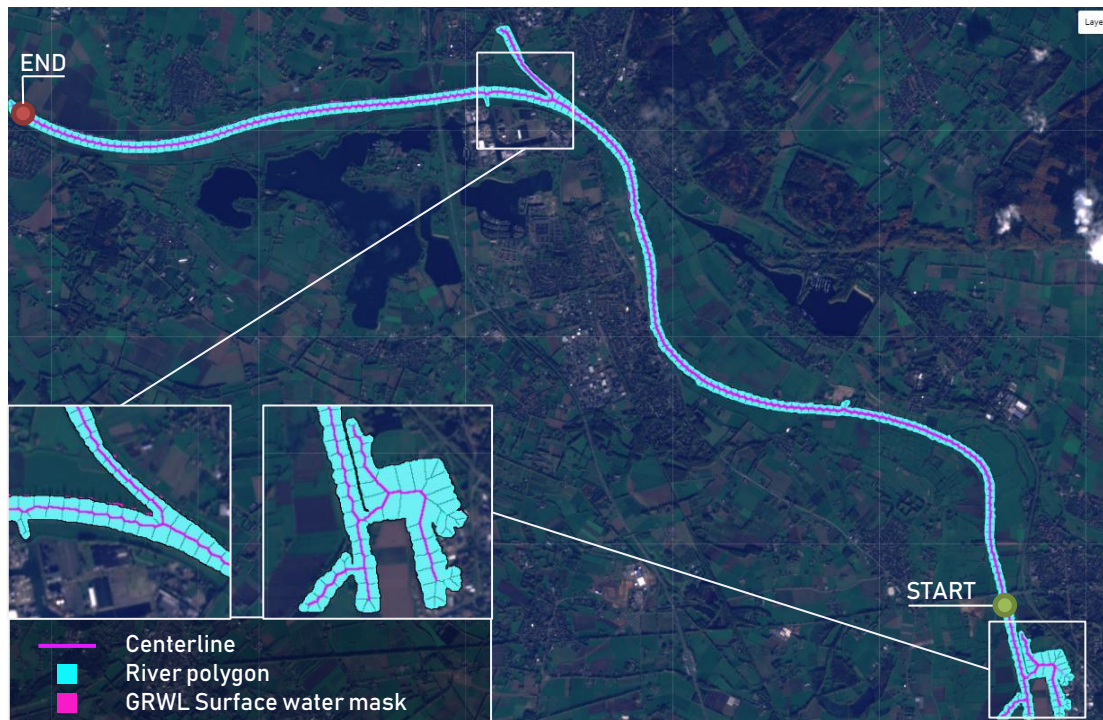


Figure 4.2 – The centerline (purple), river polygon (cyan), and surface water mask (magenta; Allen and Pavelsky, 2018) for a segment of the Meuse, based on a cloudless multispectral image (17-11-2017).

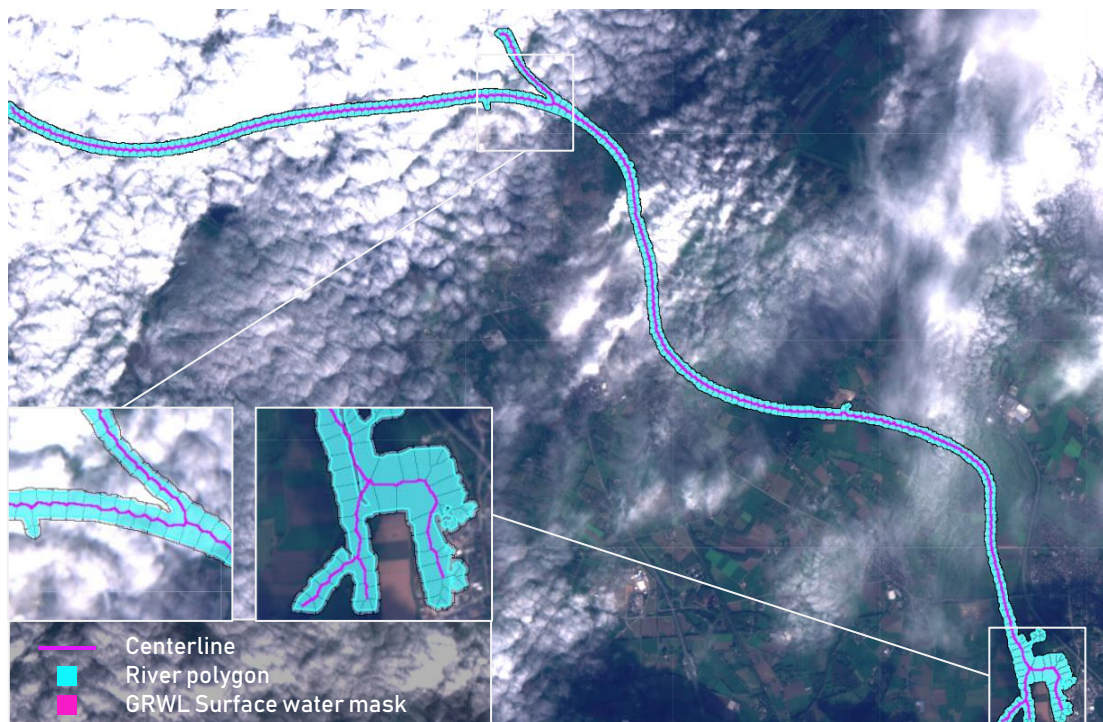


Figure 4.3 – The centerline (purple), river polygon (cyan), and surface water mask (magenta; Allen and Pavelsky, 2018) for a segment of the Meuse, based on a cloudy multispectral image (02-11-2017).

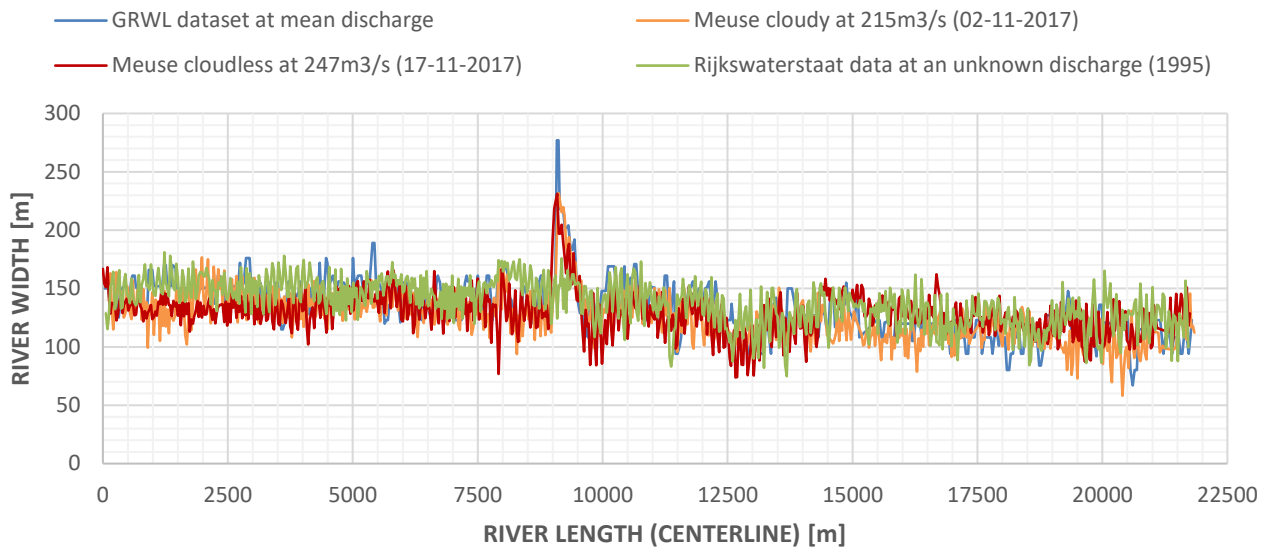


Figure 4.4 – Comparison between the river widths of the GRWL dataset (blue) and a cloudy (orange) and cloudless (red) multispectral satellite image at mean discharge, as well as the river width of the river polygon provided by Rijkswaterstaat (green), for a segment of the Meuse.

Figure 4.4 demonstrates clear similarities between river widths derived from both cloudless and cloudy EO satellite images, the river polygon provided by Rijkswaterstaat and the GRWL dataset. The mean river widths were found to be 129, 125 and 131 meters respectively. The mean river width of the GRWL dataset equals 133 meters. The peak at a river length of roughly 9000 meters as a result of a bifurcation is not present within the river polygon provided by Rijkswaterstaat and is therefore not noticeable in Figure 4.4.

Furthermore, although this may be difficult to notice, it is found that, occasionally, the GRWL dataset may be slightly shifted compared to the EO satellite-based results (in terms of the river length). This can be attributed to the fact that the centerline is not always completely parallel to the bounds of a river. However, to be fair, this is not the case for the EO-satellite based centerline either, since it relies on a Voronoi-based skeleton. This shows that there definitely is room for improvement. For example, a comparison between the centerlines of both methods is illustrated in Figure 4.5. A jagged centerline, compared to a smooth centerline, will generally result in a slight overestimation of a river’s length.



Figure 4.5 – Comparison between the quality of the centerline of the approach as seen in §3.5 (purple) and the GRWL dataset (black).

Beside the Meuse, the same procedure is applied to a segment of the Rhine one its tributaries (that is, the Waal). Figure 4.6 demonstrates the typical representation of the EO satellite-based river polygons (cyan), as well as the river polygons provided by Rijkswaterstaat (orange), under both cloudless and cloudy circumstances. For the sake of completion, the Pannerden Canal is also shown. Similar to the selected segment of the Meuse, the shapes of the EO satellite-based river polygons appear to show a high degree of similarity compared to the river polygon provided by Rijkswaterstaat.

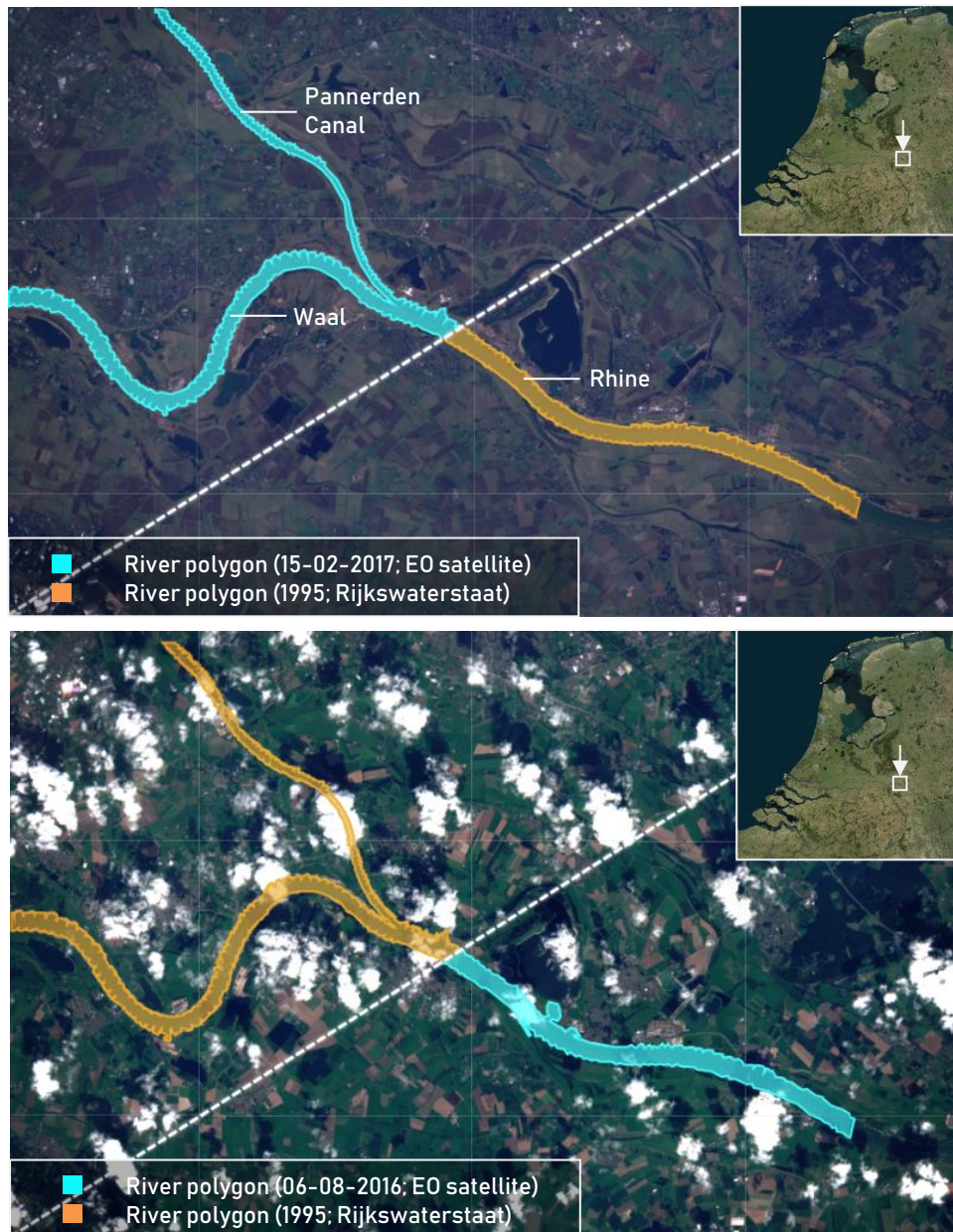


Figure 4.6 – Differences between an automatically generated river polygon (cyan) and a river polygon provided by Rijkswaterstaat (orange) of a segment of the Rhine and two of its tributaries (Waal and Pannerden Canal), for both cloudless and cloudy satellite images.

Firstly, both the surface areas and the mean river widths are compared for the selected segment of the Rhine, as well as a segment of the Waal, at four instances in time throughout 2016. The Pannerden Canal is ignored. The results are presented in Tables 4.3 and 4.4. The results show that the total surface area of the EO satellite-based river polygons under cloudless circumstances deviate between +10.07% and -2.42% from its reference case throughout 2016. For the same period, the mean river widths deviate between +7.36% and -3.81% from the point of reference (+29 and -15 meters respectively). For cloudy EO satellite-based images, the river polygons were found to deviate between +6.92% and -1.40% in terms of the total surface area. The corresponding mean river widths were found to deviate between +4.31% and -3.30% from the reference case (+17 and -13 meters respectively).

Table 4.3 – Comparison between the total surface area and mean river width of various river polygons of a segment of both the Rhine and the Waal throughout 2016, based on fairly cloudless EO satellite images (< 15% cloud coverage), as well as the river polygon provided by Rijkswaterstaat (1995).

River polygon origin	Date [dd-mm-yyyy]	Total surface area [m ²]	Relative difference [%]	Mean river width [m]	Relative difference [%]
Rijkswaterstaat	1995	8,499,401	-	394	-
EO satellite	11-04-2016	9,073,245	+6.75	409	+3.81
EO satellite	07-06-2016	9,355,440	+10.07	423	+7.36
EO satellite	08-09-2016	8,334,131	-1.94	381	-3.30
EO satellite	04-12-2016	8,293,886	-2.42	379	-3.81

Table 4.4 – Comparison between the total surface area and mean river width of various river polygons of a segment of both the Rhine and the Waal throughout 2016, based on cloudy EO satellite images (≥ 15% cloud coverage), as well as the river polygon provided by Rijkswaterstaat (1995).

River polygon origin	Date [dd-mm-yyyy]	Total surface area [m ²]	Relative difference [%]	Mean river width [m]	Relative difference [%]
Rijkswaterstaat	1995	8,499,401	-	394	-
EO satellite	09-03-2016	8,860,073	+4.24	400	+1.52
EO satellite	10-07-2016	9,087,488	+6.92	411	+4.31
EO satellite	18-09-2016	8,419,329	-0.94	383	-2.79
EO satellite	17-12-2016	8,380,131	-1.40	381	-3.30

Additionally, the river widths of both a cloudless and cloudy EO-satellite images and the GRWL dataset are compared at mean discharge. Furthermore, the river widths are compared to the river polygon provided by Rijkswaterstaat. The mean discharge for the selected segment of the Rhine was found to be ~2122 m³/s at a gauge station nearby Lobith. Both a cloudless and cloudy (based on a 4-month sampling time span) multispectral satellite image were sampled on 26-01-2017 (~2289 m³/s) and 27-07-2016 (~2337 m³/s). In Figures 4.7 and 4.8, for both the cloudless and cloudy multispectral satellite images, river polygons are shown including their centerlines, as well as the surface water mask sourced from the GRWL dataset. In Figure 4.9, the river widths are compared at mean discharge. Here, Pannerden Canal is excluded. For both the river polygon provided by Rijkswaterstaat as well as the EO satellite-based river polygons, data is sampled every 10 meters. In Figure 4.7, “start” and “end” denote the length over which the river width is sampled.

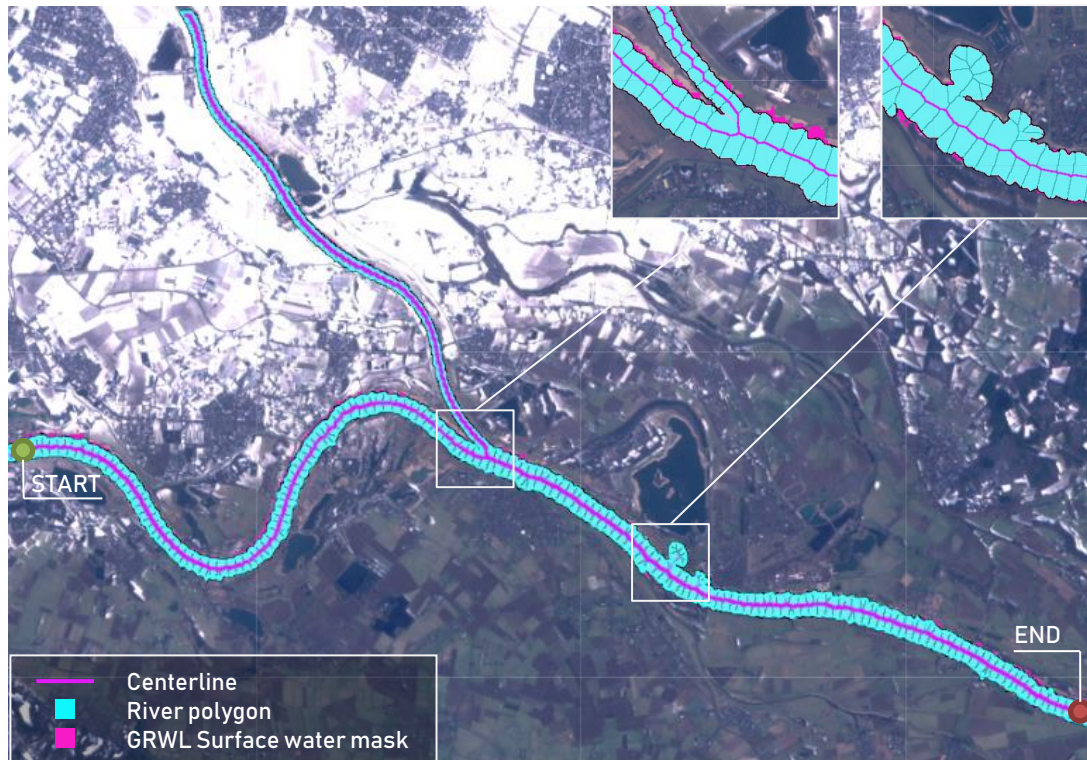


Figure 4.7 – The centerline (purple), river polygon (cyan), and surface water mask (magenta; Allen and Pavelsky, 2018) for a segment of the Rhine and the Waal/Pannerden Canal, based on a cloudless multispectral image (26-01-2017).

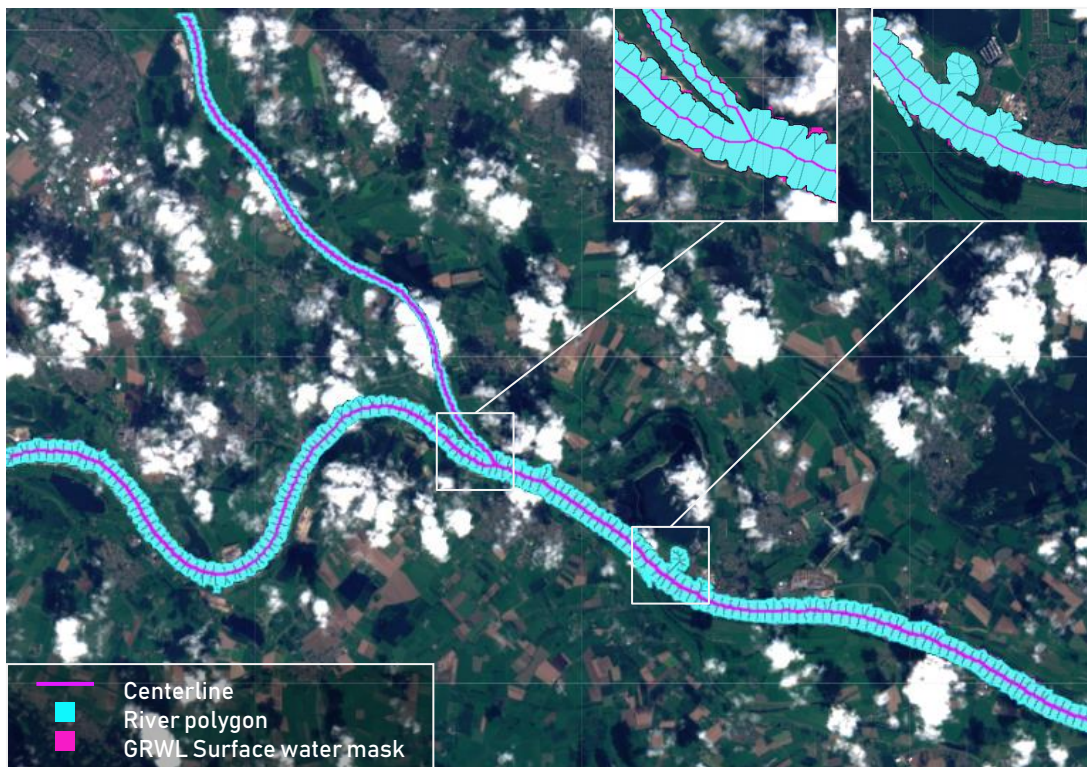


Figure 4.8 – The centerline (purple), river polygon (cyan), and surface water mask (magenta; Allen and Pavelsky, 2018) for a segment of the Rhine and the Waal/Pannerden Canal, based on a cloudy multispectral image (27-07-2016).

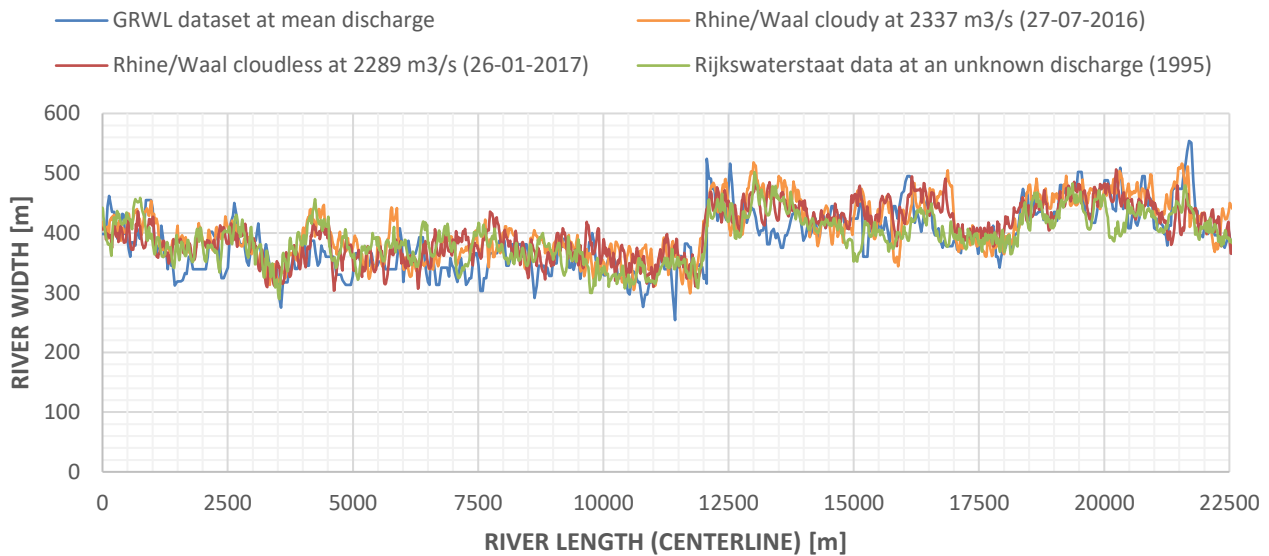


Figure 4.9 – Comparison between the river widths of the GRWL dataset (blue) and a cloudy (orange) and cloudless (red) multispectral satellite image at mean discharge, as well as the river width of the river polygon provided by Rijkswaterstaat (green), for a segment of the Rhine and Waal (as seen in Figure 4.10).

The geometries derived from both cloudless and cloudy EO satellite images, the river polygon provided by Rijkswaterstaat and the GRWL dataset were found to be highly similar (see Figure 4.9). The mean river widths equal 402, 408, 394 and 393 meters respectively. Larger deviations at certain river lengths (e.g. 4300 and 13500 meters) can be attributed to the fact that the estimated river polygon is found to be wider than the water mask of the GRWL dataset. However, upon closer inspection based on visual interpretation, no clear overestimations of the river widths could be observed.

All in all, the results of the EO-satellite based river polygons show a high-degree of similarity towards the river polygons provided by Rijkswaterstaat as well as the GRWL dataset. Throughout 2016, for a segment of the Meuse, deviations between +2 and -2 meters (+1.53% and -1.53%) as well as +1 and -8 meters (+0.76% and -6.11%) were found compared to data provided by Rijkswaterstaat, for cloudless and cloudy images respectively. For a segment that comprises of the Rhine and the Waal, deviations between +29 and -15 meters (+7.36% and -3.81%), and +17 and -13 meters (+4.31% and -3.30%) were found for cloudless and cloudy images respectively, for the same year. Additionally, further investigation towards the validity of EO satellite-based river geometries (Figures 4.4 and 4.9) showed clear similarities towards the river polygons provided by Rijkswaterstaat as well as the GRWL dataset.

4.2 GLOBAL APPLICABILITY & LIMITATIONS

To assess the global applicability of the formed procedure, polygons were generated for seven rivers around the world. Alabyan and Chalov (1998) suggested a classification scheme where a river is classified based on its “structural level” (valley bottom, flood channel or low water channel) and its plan outline (straight, sinuous and branched). The scheme is outlined in Appendix D. In order to make sure most of the river types are covered, rivers were selected based on this particular classification scheme, each displaying various features (e.g. meandering, braiding, point bars, medial bars, islands and varying sizes), and under different climate conditions. In Figure 4.10 the selected locations are displayed on a geographical map. The results are demonstrated in Figures 4.11-4.17 for both Landsat 8 and Sentinel-2. Furthermore, typical resulting centerlines for complex shapes are presented in Figure 4.18 and Figure 4.19. Both the date of interest as well as cloud content within a multispectral satellite image were selected at random. In terms of the overall global applicability of the method, the following limitations were found:

- The generation of river polygons is limited to rivers that are at least three to four times the width of the corresponding satellite’s spatial resolution in order to obtain usable results (based on Landsat-8 and Sentinel-2’s spatial resolution of 10×10 and 30×30 meters respectively). Relatively small water features can simply not be detected when the spatial resolution is too coarse. For example, in Figures 4.11 and 4.14, areas where this is indeed the case are highlighted by means of orange colored circles. Furthermore, the temporal resolution is limited to 16 and 5 days respectively (Landsat 8 and Sentinel-2). A more frequent revisit period would allow for historical images to be sampled within a smaller time window, which is likely to result in more accurate estimates under cloudy circumstances.
- Similar to a river polygon, if a river is found to be relatively narrow, the centerline can often not be computed, or is incomplete. This can be seen in Figure 4.19, and generally occurs if a river is less than 75 meters wide. This, in fact, has to do with the number of vertices present within a polygon. Vertices at more frequent intervals result in a more accurate EDM, ultimately producing a more accurate skeleton. Generally, frequent intervals between the vertices are needed for relatively narrow channels in order to generate an accurate centerline. However, it is found that if the number of vertices is increased, parts of the centerline may still fail. In fact, there is a chance that the same problem occurs in case of a relatively low number of vertices. A post⁹ on the GEE developers forum by Donchyts reveals that this is most likely a bug within GEE. Since the same polygon-intersection-approach is used to generate the centerline, this remains an unresolved issue for now. Some kind of workaround is necessary to avoid this issue.

⁹ <https://groups.google.com/forum/#!searchin/google-earth-engine-developers/intersection%20bug%7Csort:date/google-earth-engine-developers/z65gS-IfaqQ/sQmpLXNDEQAJ>

- The operations needed to execute the computation and thus generate a river polygon including information about its width may be too memory intensive, ultimately resulting in the computation to time out. This severely limits the maximum size of the river polygon and thus its global applicability. The following two reasons were found to be the main cause:
 - The number of concurrent queries in GEE is limited by Google (memory limit). As a result, river polygons that are relatively wide (e.g. Amazon River), or relatively lengthy (~50 km+, depending on their width) often fail to compute, or may take a very long time to do so. Optimizations of some sort or access to more memory is required to solve this issue. By profiling the script (see Appendix E), it was found that the utilization of resampling techniques as well as the projection scale (pixel resolution) are the main causes, and that there is a direct relation between the quality of a river polygon and its maximum possible size. Although larger river polygons can be generated than the ones showed in Figures 4.11-4.17, their accuracy and thus usability may be lacking (e.g. as seen in Figure 3.6 (1)).
 - The corresponding script was written with the overall performance in mind but could most certainly be optimized in terms of computation speed. However, since this was not part of the main objective, and due to limited amount of available time/relative inexperience with GEE's built-in functions¹⁰/hidden source code, this was not further investigated.
- In terms of data availability, the generation of river polygons is currently limited to multispectral satellite images originating from both Landsat 8 and Sentinel-2. Sentinel-2 provides data from 23-06-2015 and onwards, whereas Landsat 8 provides data since 11-04-2013. The usage of additional satellites allows for the extension of the total amount of available data to sample from (e.g. Landsat 7, which contains similar spectral bands to Landsat 8 and was launched on 15-04-1999).

The estimation of the geometry of a river remains limited in terms of global applicability. The main issue is currently that the computation is found to be too resource-intensive in GEE, limiting the maximum size of a river polygon that can be generated. Script optimizations or access to more memory is required to solve this issue. Furthermore, it is of importance that a workaround is found to avoid a potentially incomplete centerline. Nonetheless, it is found that, generally, the geometry of a river can indeed be determined estimated on a global level. However, the applicability of the method is currently limited to a local scale.

¹⁰ See https://developers.google.com/earth-engine/api_docs for the API reference.



River	Location
(A) Danube	nearby Budapest, Pest County, Hungary
(B) Murray River	nearby Robinvale, Victoria/New South Wales, Australia
(C) Niger River	nearby Segou, Segou Region, Mali
(D) Magdalena River	nearby La Dorada, Caldas/Cundinamarca, Colombia
(E) Thanlyin River	nearby Khe Kpyu, Kayah State, Myanmar
(F) Irtysh River	nearby Turtas, Tyumen, Russia
(G) Yellowstone River	nearby Forsyth, Montana, USA

Figure 4.10 – An overview of the selected rivers and their locations (source: Map data © 2018 Google).

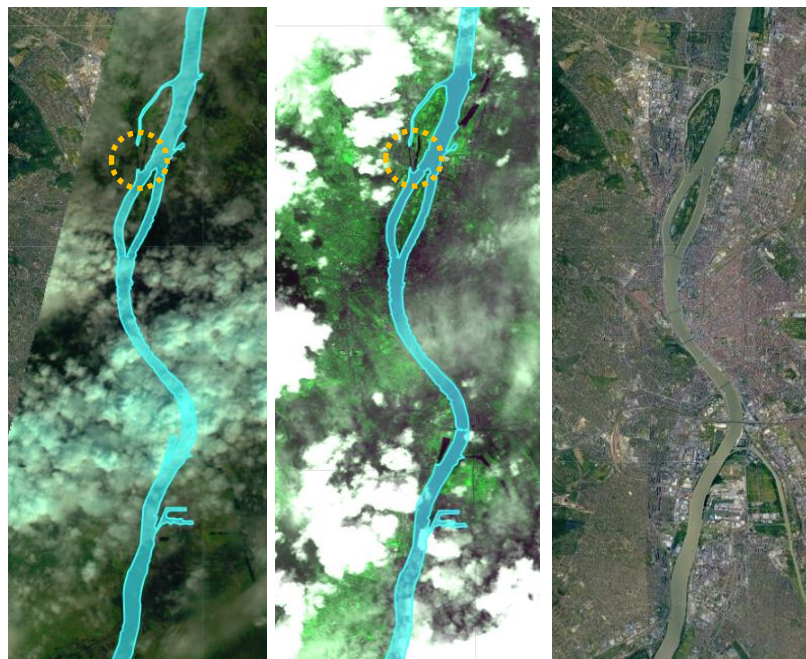


Figure 4.11 – Typical resulting river polygons for the Danube in Budapest, Hungary, based on Landsat 8 and Sentinel-2 data respectively. The third image (right) is a standard google maps image (source: Map data © 2018 Google).

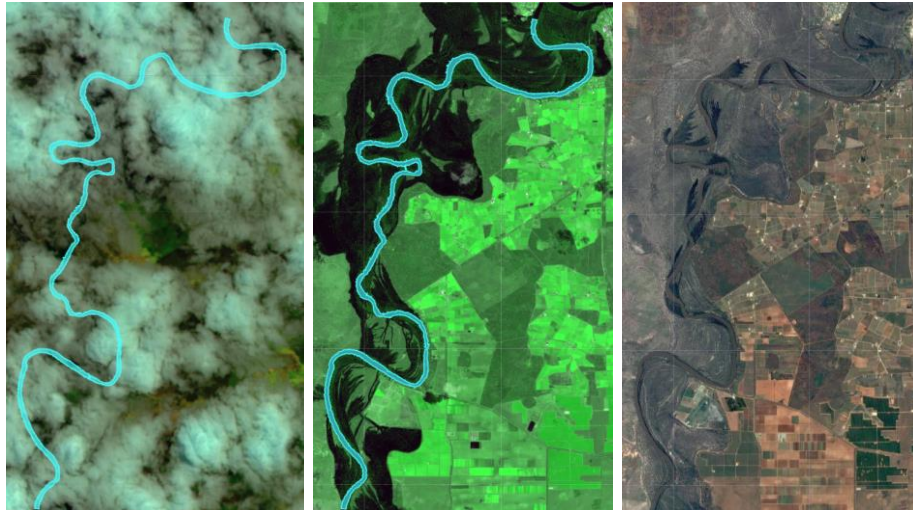


Figure 4.12 – Typical resulting river polygons for the Murray River in Victoria/New South Wales, Australia, based on Landsat 8 and Sentinel-2 data respectively. The third image (right) is a standard google maps image (source: Map data © 2018 Google).

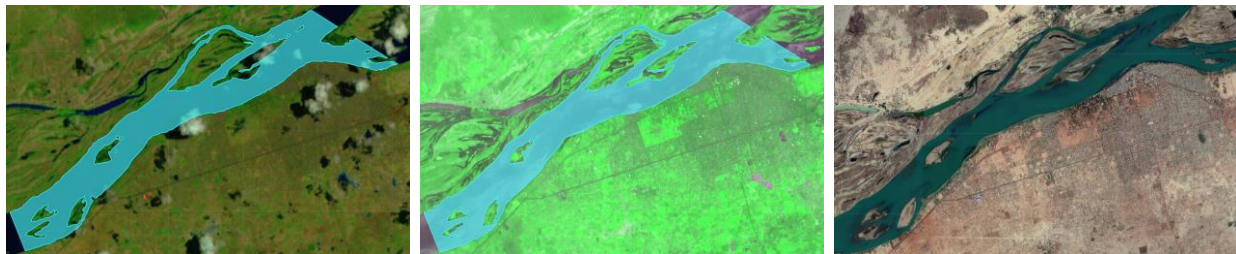


Figure 4.13 – Typical resulting river polygons for the Niger River in Segou, Mali, based on Landsat 8 and Sentinel-2 data respectively. The third image (bottom) is a standard google maps image (source: Map data © 2018 Google).

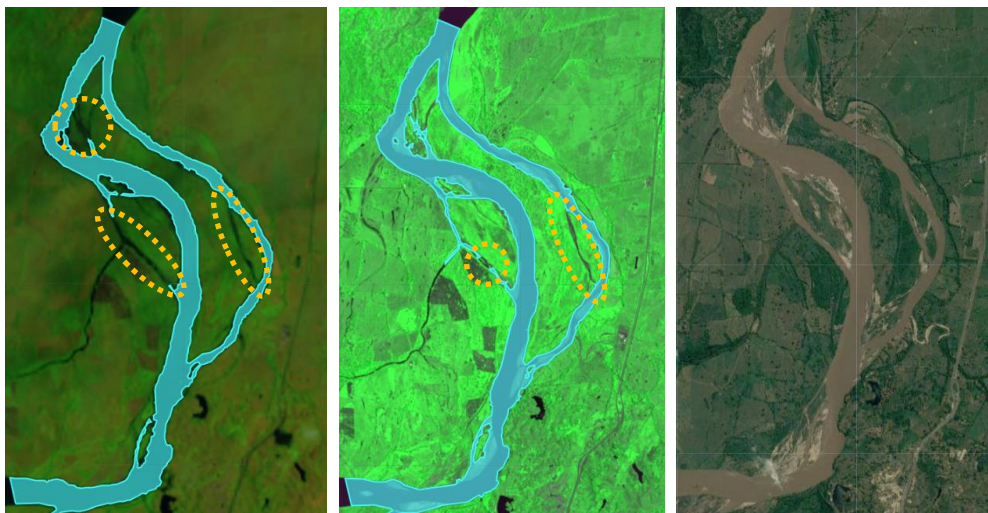


Figure 4.14 – Typical resulting river polygon for the Magdalena River nearby La Dorada, Colombia, based on Landsat 8 and Sentinel-2 data respectively. The third image (right) is a standard google maps image (source: Map data © 2018 Google).



Figure 4.15 – Typical resulting river polygon for the Thanlyin River nearby Khe Hpyu, Myanmar, based on Landsat 8 and Sentinel-2 data respectively. The third image (right) is a standard google maps image (source: Map data © 2018 Google).

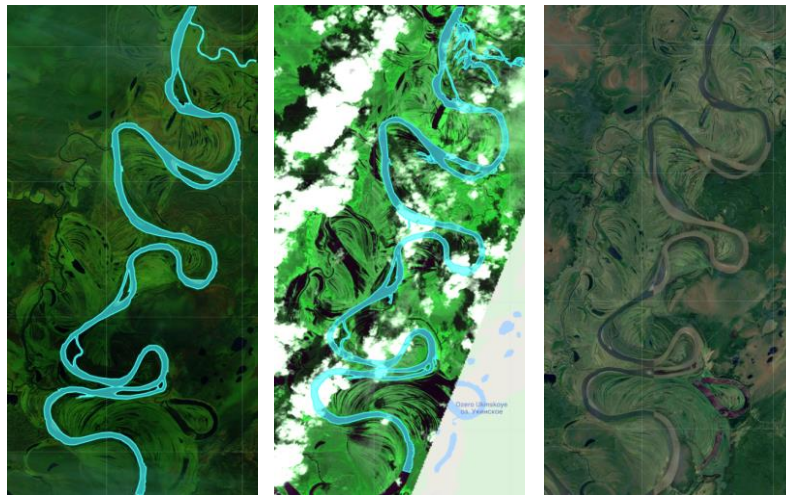


Figure 4.16 – Typical resulting river polygon for the Thanlyin River nearby Turtas, Russia, based on Landsat 8 and Sentinel-2 data respectively. The third image (right) is a standard google maps image (source: Map data © 2018 Google).

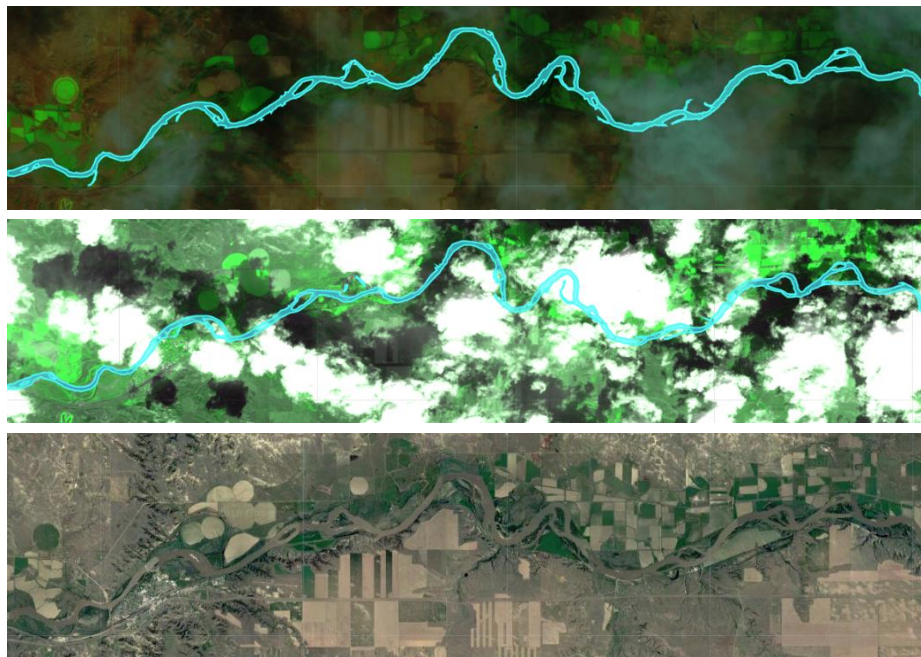


Figure 4.17 – Typical resulting river polygon for the Yellowstone River nearby Forsyth, USA, based on Landsat 8 and Sentinel-2 data respectively. The third image (bottom) is a standard google maps image (source: Map data © 2018 Google).

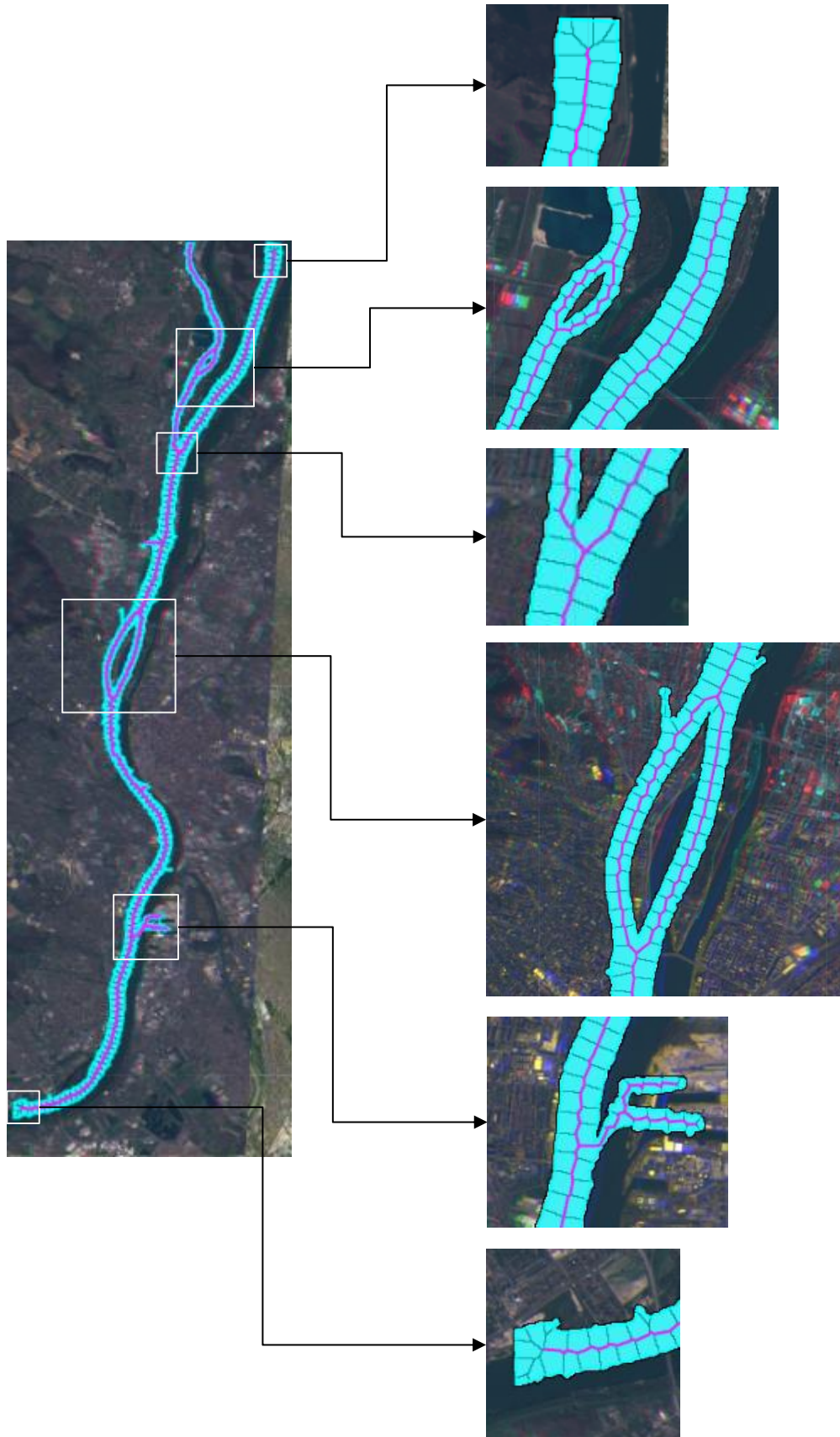


Figure 4.18 – Typical resulting centerline for a segment of the Danube in Budapest, Hungary (Sentinel-2).

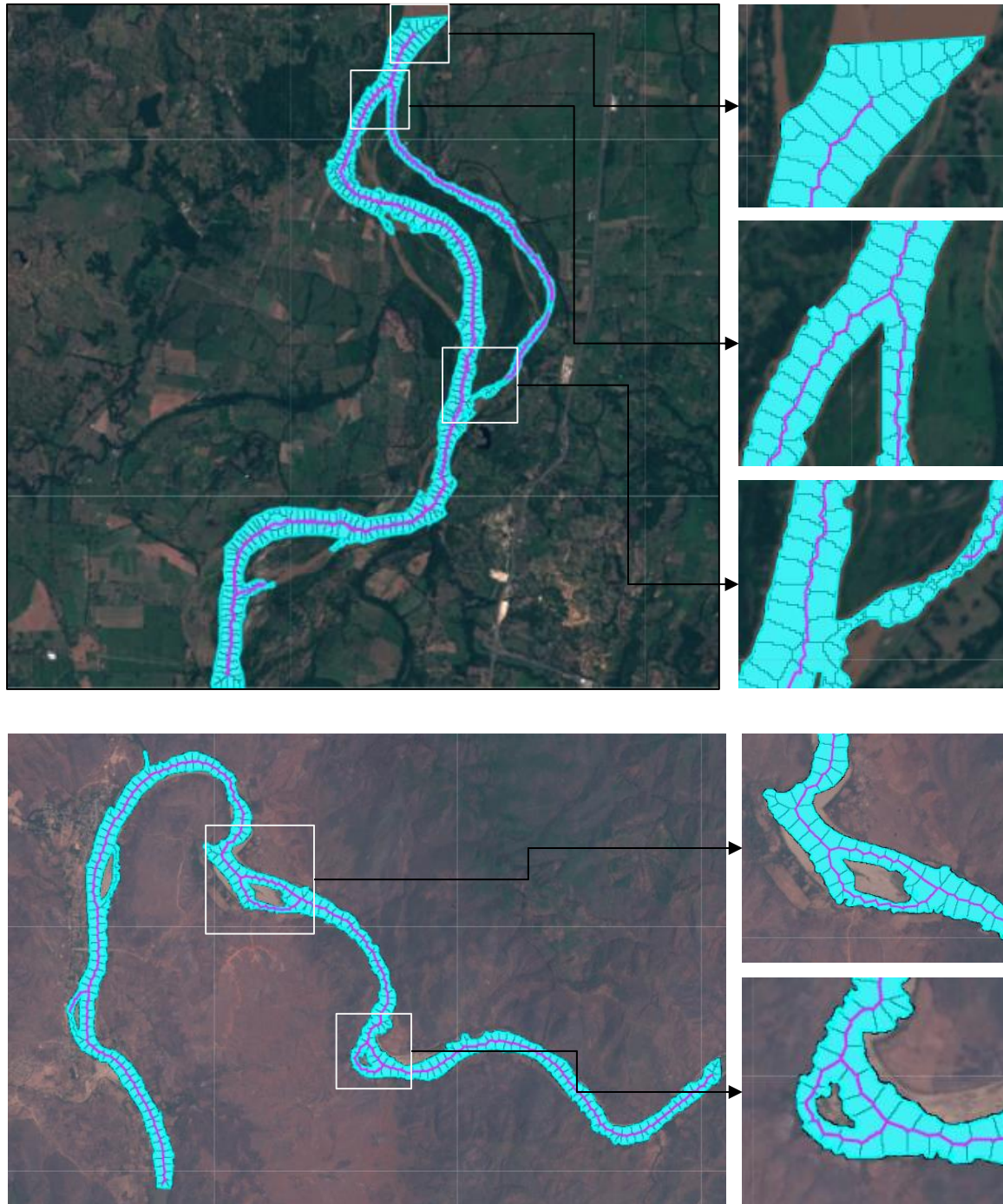


Figure 4.19 – Typical resulting centerlines for segments of the Magdalena River nearby Dora, Colombia, and the Thanlyin River nearby Khe Hpyu, Myanmar (Sentinel-2).

5. SENSITIVITY ANALYSIS

In this chapter a sensitivity analysis is conducted to obtain insight into the dependency of the estimated geometry of a river towards influential variables. The sensitivity of selected parameters is analyzed based on the initially selected study area—that is the Trinity River. Surface area values of water and their relative differences are compared to assess the significance of a change. The same is done for the mean river widths¹¹. The sensitivity of parameters related to the detection of water that have been examined in the past are not further investigated (e.g. the utilization of Otsu’s method to detect surface water in an automated manner as seen in Donchyts et al., 2016).

Historical imagery: sampled time span

Historical satellite images have been used to estimate the course of a river under circumstances where a satellite is obstructed by clouds, haze or fog. The time span over which historical data is sampled influences the estimated course of a river. To gain insight into the impact of this parameter towards the geometry of a river, the sensitivity is investigated. More specifically, the sensitivity of the estimated course of a river to varying time windows—that is, 1 month, 2 months, 4 months, 8 months, 16 months and 32 months—is explored. Two cloudless multispectral satellite images of a segment of the Trinity River, taken on 26-10-2016 and 24-04-2017, are selected as point of references. Historical images are sampled relative to this date and merged with the originally detected surface water mask. For example, a time window of 2 months ranges from 26-09-2016 up to 25-11-2016 (~-30 and +30 days from its point of reference, that is 26-10-2016 in this case). Both the changes towards the surface area and the mean river width are compared. Note that, to assess the sensitivity of various sampling windows towards the Trinity River, the historical composite is not eroded before it is merged with the detected surface water mask. The result is displayed in Figure 5.1, as well as Table 5.1 and Table 5.2.

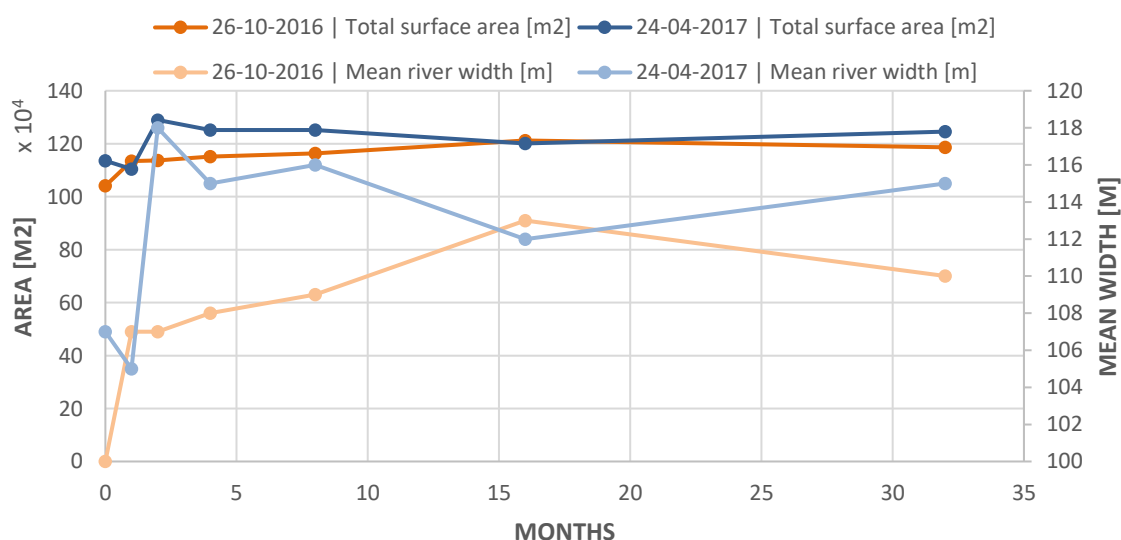


Figure 5.1—Sensitivity of the Trinity River towards a gradually enlarged time window of the historical composite.

¹¹ Note that, in some cases, mean river widths could not be derived from a surface water mask as a result of relatively narrow rivers bounds, or simply because the course of a river could not be reliably estimated. This is denoted with an asterisk (*).

Table 5.1 – Sensitivity of the Trinity River towards a gradually enlarged time window of the historical composite, in addition to the relative differences between the total surface areas and the mean river widths for a cloudless multispectral satellite image taken on 26-10-2016.

Months	Total surface area [m ²]	Relative difference [%]	Mean river width [m]	Relative difference [%]
0	1,041,184	-	100	-
1	1,134,659	+8.98	107	+7.00
2	1,136,599	+9.16	107	+7.00
4	1,151,161	+10.56	108	+8.00
8	1,163,050	+11.70	109	+9.00
16	1,212,316	+16.44	113	+13.00
32	1,186,237	+13.93	110	+10.00

Table 5.2 – Sensitivity of the Trinity River towards a gradually enlarged time window of the historical composite, in addition to the relative differences between the total surface areas and the mean river widths for a cloudless multispectral satellite image taken on 24-04-2017.

Months	Total surface area [m ²]	Relative difference [%]	Mean river width [m]	Relative difference [%]
0	1,136,305	-	107	-
1	1,104,517	-2.80	105	-1.87
2	1,289,814	+13.51	118	+10.28
4	1,251,668	+10.15	115	+7.48
8	1,252,269	+10.21	116	+8.41
16	1,201,216	+5.71	112	+4.67
32	1,245,420	+9.60	115	+7.48

The results show that the Trinity River is, generally, sensitive to the time span over which historical data is sampled. The relative differences for the satellite image taken on 26-10-2016 show an increasing trend, whereas the relative differences for the satellite image taken on 24-04-2017 vary quite heavily. Only after a period of roughly 16 months, the relative difference, for both cases, appears to somewhat stabilize.

In general, the sensitivity of the estimated geometry of a river towards the varying sampling windows highly depends on two factors: (1) variations of the stream width over time and (2) the assumed weighted distribution, since the historical composite represents a weighted average.

Historical imagery: threshold value

To exclude pixels that have been falsely interpreted as water, or water that is in fact not part of the main river course as a result of a possible short-term flood, a threshold value was introduced. Values assigned to pixels of the historical composite are rescaled to a range of values between [0, 1], where values that are less than a predefined threshold are set to 0. To investigate the sensitivity of this particular threshold value, a cloudy multispectral satellite image taken on 06-10-2016 is selected, where threshold values of 0.1, 0.2, 0.4 and 0.8 are tested and their relative differences are compared. Since the number of images sampled affects the impact of the threshold value, this is done for a total of 5, 10, 20 and 40 images, respectively. In this case, a total of 5 images translates to a time window of roughly 2 months, 10 to 4 months and 20 to 8 months and 40 to 16 months. The results are demonstrated in Figure 5.2 and Figure 5.3., as well as and Table 5.3.

5. SENSITIVITY ANALYSIS

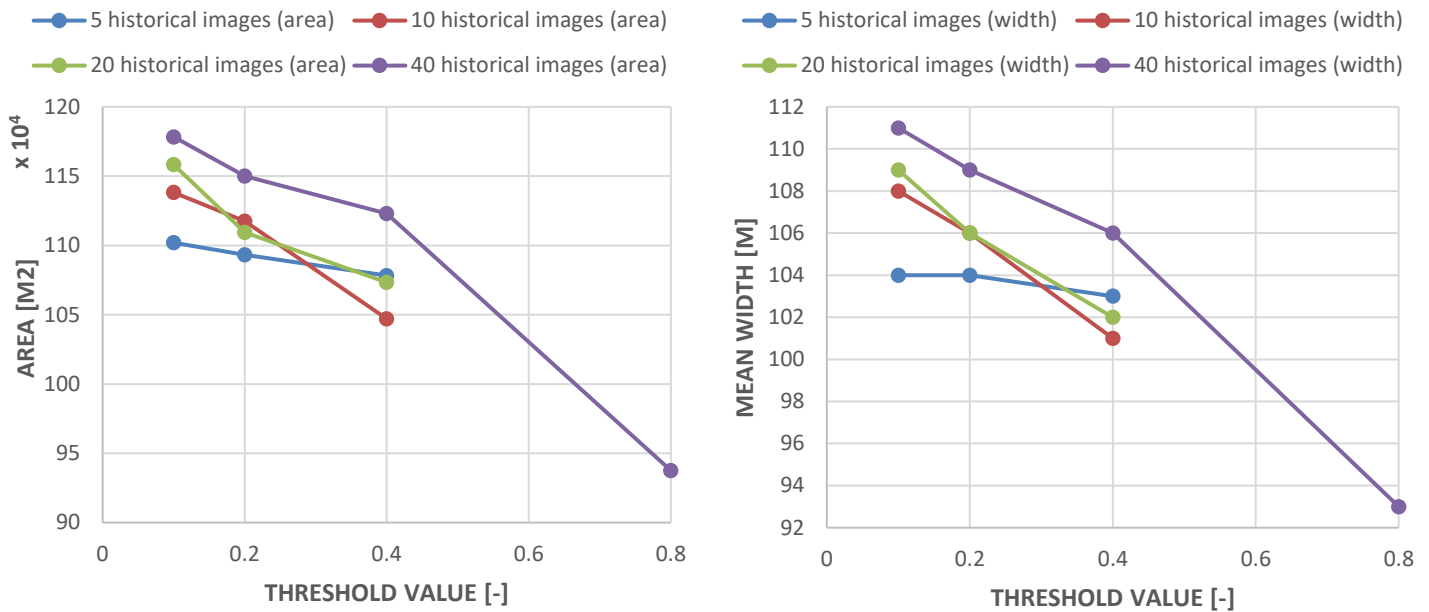


Figure 5.2 – Sensitivity of the historical composite of the Trinity River towards an increasing threshold value, as well as an increasing number of sampled images.

Table 5.3 – Sensitivity data belonging to the Trinity River, showing the total surface area, the mean river width as well as their relative differences for varying threshold values and number of historical images. *A threshold value of 0.8 fails to detect the complete course of a river for 5, 10 and 20 historical images, resulting in unreliable mean river widths, and is therefore left out.

Number of historical images	Threshold value	Total surface area [m ²]	Relative difference [%]	Mean river width [m]	Relative difference [%]
5 (~2 months)	0.1	1,101,945	-	104	-
	0.2	1,093,148	-0.80	104	0.00
	0.4	1,078,268	-2.15	103	-0.96
	0.8	*	*	*	*
10 (~4 months)	0.1	1,138,206	-	108	-
	0.2	1,117,384	-1.80	106	-1.85
	0.4	1,047,037	-8.00	101	-6.48
	0.8	*	*	*	*
20 (~8 months)	0.1	1,158,282	-	109	-
	0.2	1,109,489	-4.21	106	-2.75
	0.4	1,073,355	-7.33	102	-6.42
	0.8	*	*	*	*
40 (~16 months)	0.1	1,178,365	-	111	-
	0.2	1,149,998	-2.41	109	-1.80
	0.4	1,122,992	-4.70	106	-4.50
	0.8	937,605	-20.43	93	-16.22

The results show that, as the threshold value is increased, both the total surface area and the mean river width decreases. For relatively low threshold values, the relative differences remain quite small. For sampling periods of roughly 4 months (~10 images) and more, the Trinity River was found to be sensitive to a threshold value that is generally equal or larger than 0.4. Threshold values that are equal or higher than 0.8 caused the estimation of certain segments of the course of the Trinity River to fail, except for a sampling period of roughly 16 months (~40 images). Failure occurs, especially for relatively few numbers of sampled images, because not all historical

images are completely cloudless. All images of which the cloud coverage is equal or less than 15% are considered. Although this percentage could be lowered, this is likely to result in much fewer images to sample from, depending on the location of interest. If variations happen towards the stream width, and relatively few images are sampled, there is a chance that this will not be captured. For example, consider a sampling period of 4 months. Here, 10 images are sampled, of which 4 are discarded due to their limited representation of the predefined area of interest (see Figure 5.3). Furthermore, for simplicity, assume that there is no weight value attached to a sampled image ($\forall i \in I; weight = 1$). The result is a composite that fails to estimate the complete course of the river for a threshold value that is equal or larger than 0.5. For example, consider one pixel that is, under cloudless conditions, part of the Trinity River in the lower left corner of the set of images. The value that is assigned to the pixel equals 1 in three of the considered images, since water has been detected. However, as a result of cloud obstructions, the value that is assigned to said pixel equals 0 in the other three images since water could not be detected. The value that is assigned to the pixel of the water occurrence composite is therefore $\frac{(1+1+1)}{6} = 0.5$, meaning that if the threshold value is equal or greater than 0.5, the value of the pixel is set to 0 and is considered to be a background feature. All things considered, a river is only found to be sensitive to this parameter for relatively high threshold values. Generally, a value of 0.2 is found to work well, which was also used to assess the global applicability.

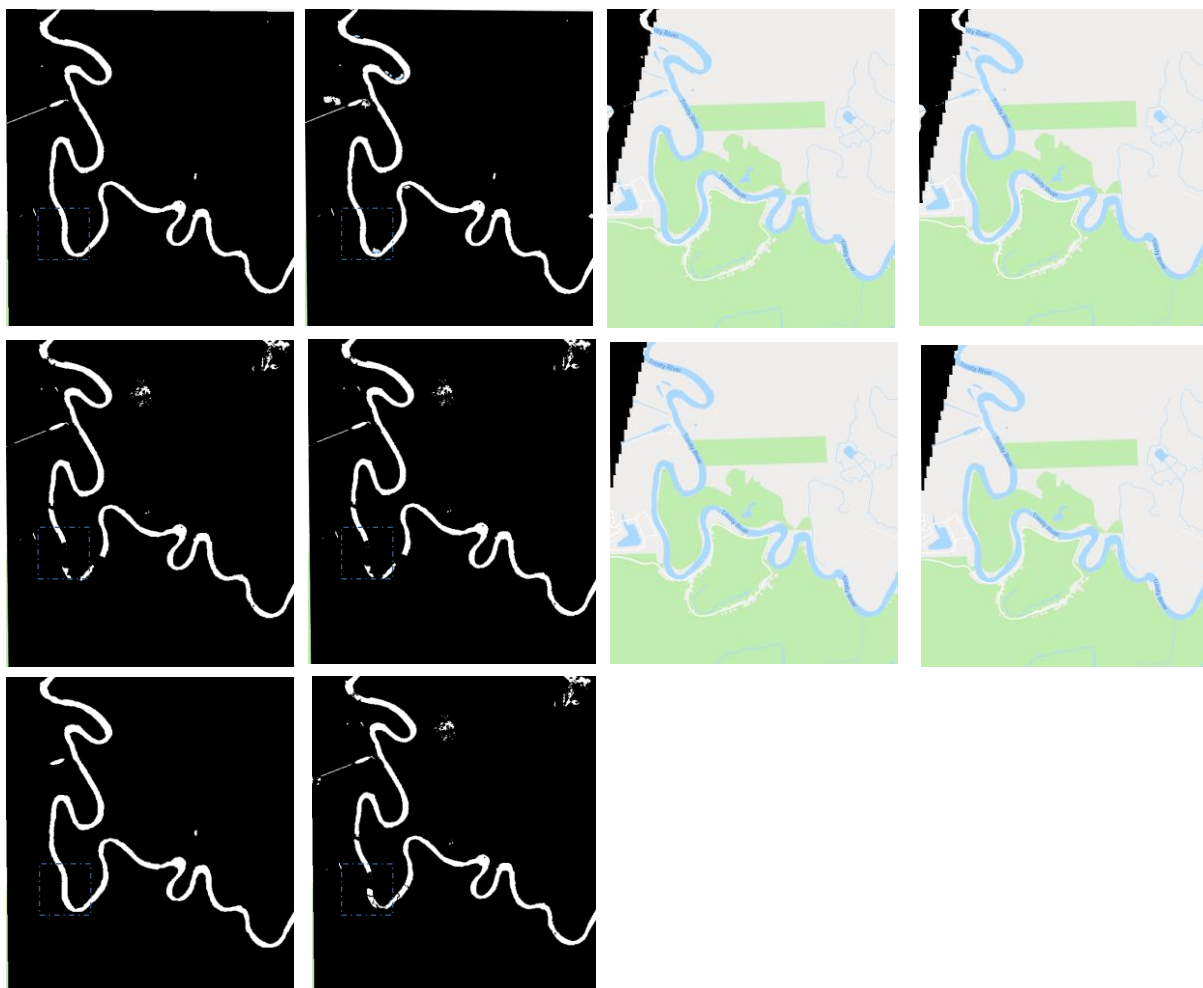


Figure 5.3 – A typical set of sampled images used to generate the water occurrence composite (sampling time window equals 4 months).

Weighted distribution

To vary the contribution of a sampled image towards the historical composite, an inverse distance weighting function was introduced, where the weight attached to an image is based on the date at which it is sampled relative to the considered date of interest, as well as a power parameter p . The shape of the distribution by which sampled images are weighted depends on p (see Figure 5.4 (right)). The sensitivity of p towards a segment of the Trinity River is investigated by generating a series of historical composites from a cloudy satellite image taken on 06-10-2016, for the set $A = \{0, 0.2, 0.4, 0.8, 1.6, 3.2\}$ where $p_i \in A$. The sampling period is a total of 4 months, resulting in 11 images. The threshold value is set to 0.2, and thus every pixel that has been assigned a value that is less than 0.2 is set to 0. Both the total surface area and the mean river widths are compared (see Figure 5.4 (left) and Table 5.4).

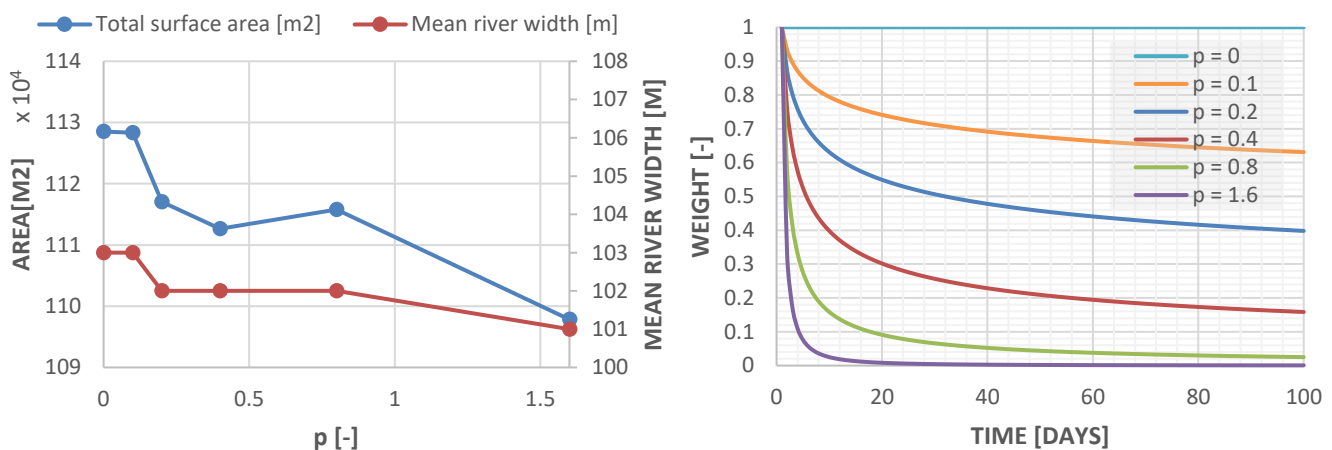


Figure 5.4 – Sensitivity of varying weight distributions towards the estimated historical composite of the Trinity River for a sampling period of 4 months (date of interest = 06-10-2016).

Table 5.4 – Relative differences between varying total surfaces areas and mean river widths of the estimated historical composite for varying weight distributions, corresponding to a segment of the Trinity River.

p	Total surface area [m ²]	Relative difference [%]	Mean river width [m]	Relative difference [%]
0	1,128,520	-	103	-
0.1	1,128,333	-0.02	103	0.00
0.2	1,117,045	-1.02	102	-0.97
0.4	1,112,627	-1.41	102	-0.97
0.8	1,115,772	-1.13	102	-0.97
1.6	1,097,834	-2.72	101	-1.94

For varying weighted distributions between 0 and 1.6, only marginal differences can be observed. Compared to the historical composite that represents an average instead of a weighted average ($p = 0$), this in fact reveals that the mean stream width of the Trinity River has not varied significantly over the period wherein images have been sampled. However, this does certainly not mean that the estimated historical composite is insensitive to various weighted distributions. In fact, the sensitivity of the estimated historical composite towards varying weighted distributions highly depends on variations of the water surface width over time.

Adaptive erosion

As described in §3.3, erosion was applied in an adaptive manner to influence the impact of the historical composite towards the detected surface water mask of the course of a river. The magnitude by which the historical composite is eroded depends on the relationship between A_{ratio} and kernel radius r , where A_{ratio} was defined as $\frac{A_{SWM2}}{A_{SWM1}}$, with SWM1 being the surface water mask of the detected river, and SWM2 the surface water mask of the historical composite (A = total water surface area). The sensitivity of the historical composite of the Trinity River towards erosion is demonstrated by means of varying kernel radii. A cloudy multispectral satellite image, taken on 19-04-2016, was selected. The sampling period is a total of 4 months. The results are illustrated in Figure 5.5 and 5.6 as well as Table 5.5. Firstly, the detected surface water mask is merged with the historical composite (top row, third from the left in Figure 5.6). Here, no erosion is applied. Subsequently, the kernel radius by which the historical composite is eroded is gradually increased. Clearly, the stream width of the Trinity River is sensitive towards erosion applied to the historical composite. A gradual increase of the radius of the kernel leads to a steady decrease of both the total surface area and the mean river width.

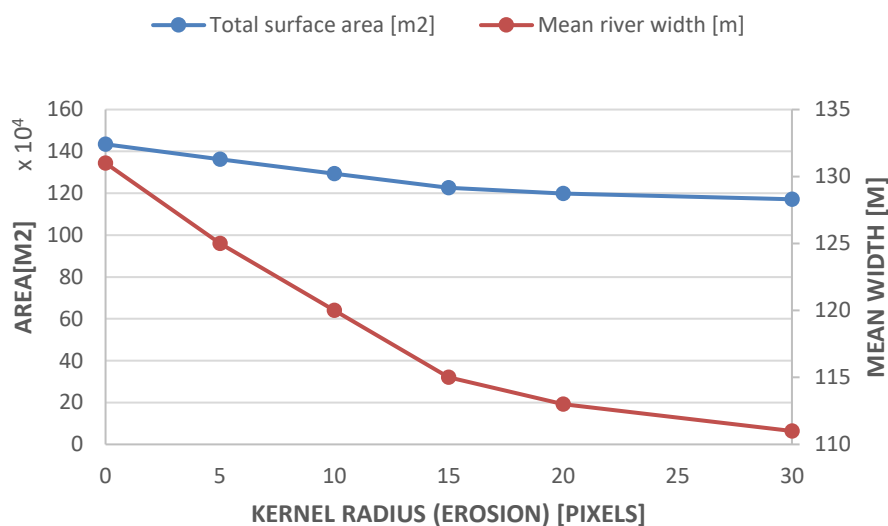


Figure 5.5 – Sensitivity of varying kernel radii (erosion) towards the geometry of the Trinity River.

Table 5.5 – Relative differences between varying total surfaces areas and mean river widths of the Trinity River, for varying radii of the kernel (erosion).

Erosion (kernel radius) [pixels]	Total surface area [m ²]	Relative difference [%]	Mean river width [m]	Relative difference [%]
0	1,434,067	-	131	-
5	1,362,397	-5.00	125	-4.58
10	1,293,911	-9.77	120	-8.40
15	1,225,412	-14.55	115	-12.21
20	1,199,274	-16.37	113	-13.74
30	1,171,273	-18.33	111	-15.27

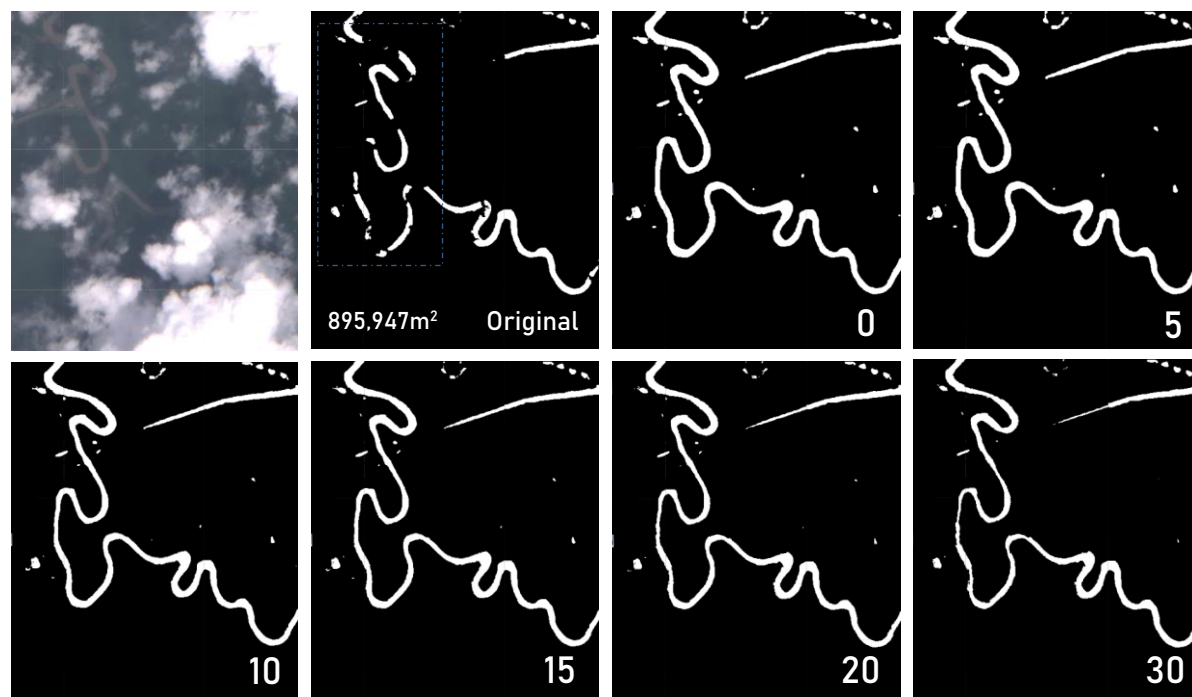


Figure 5.6 – The impact of erosion towards the derived surface water mask of the Trinity River, for various radii. The radius of the kernel from the top row, third image from the left, to bottom right are as follows: 0, 5, 10, 15, 20 and 30.

Kernel radius size

As described in §3.3, the size of the kernel radius r is dependent on A_{ratio} , if and only if A_{ratio} lies in between the upper and lower bounds of K , which was defined as a set of real values ranging from 1 to 1.5. The sensitivity of various distributions between A_{ratio} and r towards a segment of the Trinity River is investigated by increasing the upper bound of K to 2, 3 and 5 (see Figure 5.7–right). The maximum kernel radius is not adjusted, since it has been demonstrated that a radius that is too big excessively erodes the surface water mask (see Figure 5.6). For example, in theory this would mean that, if A_{ratio} equals 1.5, r would be either 0, 12.5, 18.75 or 21.88, depending on the upper bound of K , since the relationship between A_{ratio} and r is linear. Two cloudy images, taken on 06-10-2016 and 26-09-2017, are sampled to assess the impact of the distributions as shown in Figure 5.7 (right) towards the historical composite of the Trinity River. The results are shown in Figure 5.7 (left) and 5.8 as well as Table 5.6. The estimated mean river widths are not shown in Figure 5.7 (left), as a result of the inability to reliably estimate such values for most historical composites, since the river bounds were found to be too narrow to do so.

An increase of $max(K)$, thus altering the linear relationship between A_{ratio} and r , leads to more erosion for every value of A_{ratio} , as long as A_{ratio} satisfies the upper and low bounds of K . This can be seen in Figure 5.7 and 5.8, as well as Table 5.6, showing a steady decrease of the total water surface area as the upper bound for K is increased. Sampled cloudless images in the temporal proximity of 06-10-16 and 26-09-17 reveal total surface water areas of around $\sim 1,100,000 \text{ m}^2$, showing that a distribution with an upper bound of K somewhere in between 1.5 and 2 might be optimal for the Trinity River. All in all, the resulting data reveals that the Trinity River, and most likely any river, is highly sensitive to varying distributions between A_{ratio} and r . Although it remains difficult to find an optimal value for r , the usage of a linear distribution between A_{ratio} and r allows for an estimation.

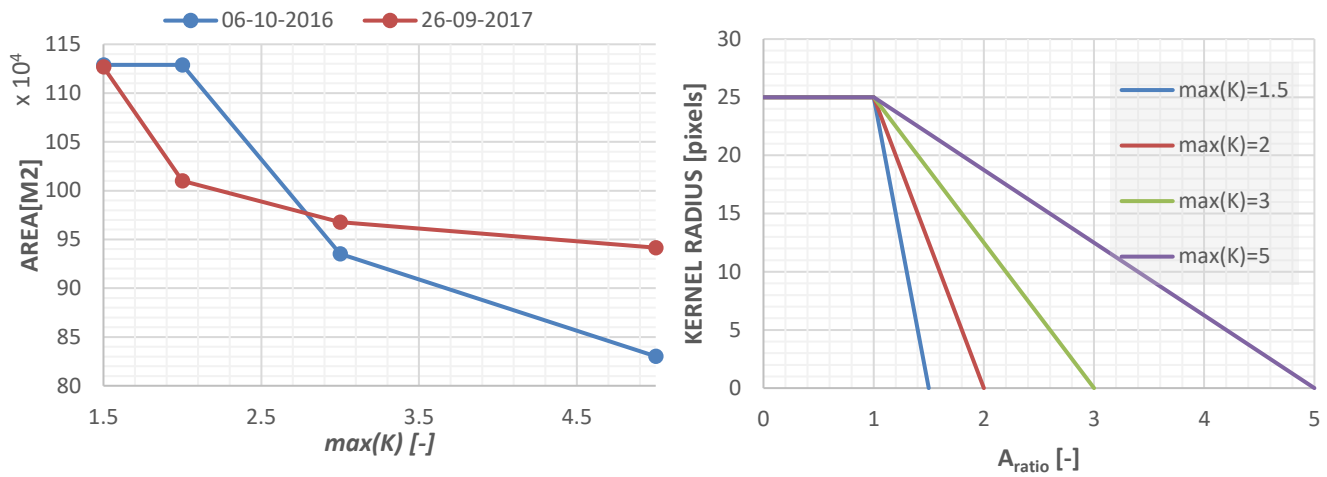


Figure 5.7 – Sensitivity of varying distributions towards the total surface area of the estimated historical composite for a segment of the Trinity River, as a result of varying upper bounds of K .

Table 5.6 – Relative differences between varying total surfaces areas and mean river widths of the estimated historical composite, for varying upper bounds of K .

Date	A_{ratio}	$max(K)$	Total surface area [m ²]	Relative difference [%]	Mean river width [m]	Relative difference [%]
06-10-16	1.88	1.5	1,128,933		103	-
		2	1,018,653	-9.77	99	-3.88
		3	935,290	-17.15	*	*
		5	830,202	-26.46	*	*
26-09-17	1.45	1.5	1,126,688		102	-
		2	1,010,117	-10.35	96	-5.88
		3	967,630	-14.12	*	*
		5	941,561	-16.43	*	*

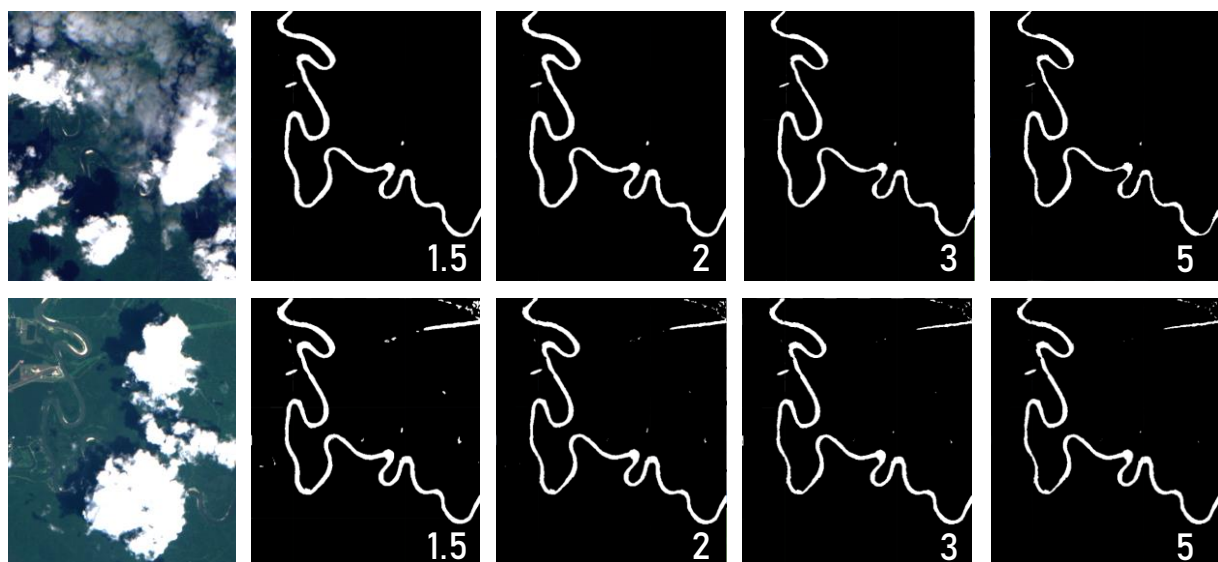


Figure 5.8 – The estimated historical composites for the distributions as illustrated in Figure 5.7, as a result of various values for the upper bound of K . Satellite images were taken on 06-10-2016 (upper row) and 26-09-2017 (lower row).

Opening

As described in §3.5, opening served as a preprocessing step in order to remove relatively small water bodies that are present within a multispectral satellite image and fill small gaps of the surface water mask that might have been overlooked by the surface water detection algorithm. The sensitivity of this parameter with respect to changes towards the surface water mask is investigated by modifying the radius of the kernel. The results are illustrated in Figures 5.9 and 5.10 as well as Table 5.7. Relatively small water bodies in comparison to the Trinity River are clearly sensitive to the operation. The Trinity River itself is largely unaffected, apart from its bounds, which are somewhat smoothed as a result of dilation. This is true up to a certain threshold value—in this case a radius of roughly 40 pixels—where water pixels can no longer be dilated since they have been removed by means of erosion. From this point onwards, the Trinity River becomes very sensitive to changes.

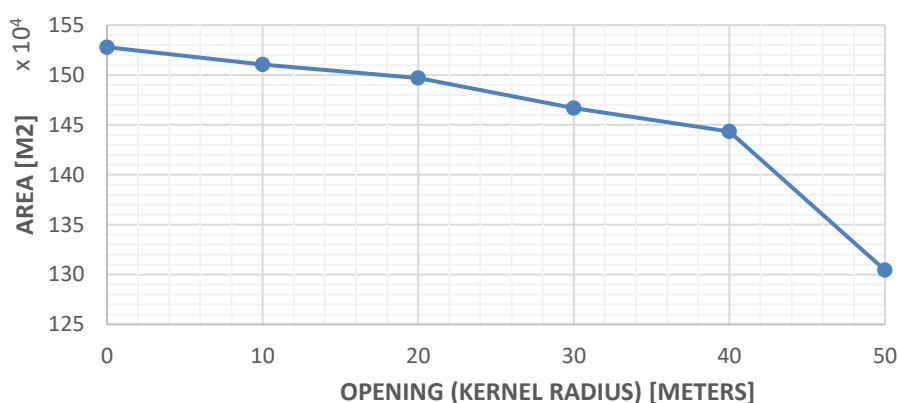


Figure 5.9— Sensitivity of the total water surface area towards varying kernel radii (opening).

Table 5.7— Relative differences between varying total water surface areas for varying kernel radii (opening).

Opening (kernel radius) [pixels]	Total surface area [m ²]	Relative difference [%]
0	1,527,910	0
10	1,510,615	-1.13
20	1,496,848	-2.03
30	1,466,926	-3.99
40	1,443,545	-5.52
50	1,304,355	-14.63

*Note that in this case the total surface area represents all detected water within a surface water mask and not just the Trinity River.

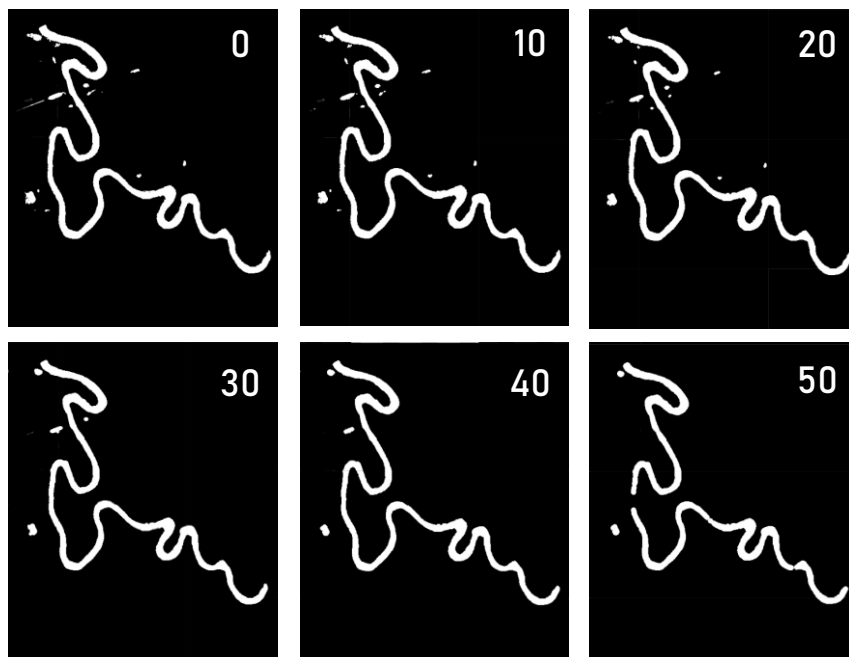


Figure 5.10— The impact of opening towards the derived surface water masks of the Trinity River for varying kernel radii.

Quality of the geometry

Lastly, there are four more parameters that greatly affect the quality of the estimated geometry, that is the resampling method, projection scale, the extent to which a river polygon is simplified, and the number of vertices used to generate the EDM, which directly affects the quality of the centerline. The impact of various resampling techniques (nearest neighbor interpolation, bilinear interpolation and bicubic interpolation) towards a river polygon has already been demonstrated in §3.4 and is therefore not further discussed.

Firstly, the projection scale—that is the pixel resolution—is found to be a highly sensitive parameter that dictates the overall quality of both the river polygon as well as the derived river widths. Although the used datasets are limited to pixel resolutions of 10×10 and 30×30 meters (Sentinel-2 and Landsat 8), rescaling the pixel resolution allows for manipulations to be executed at a higher resolution, such as 5×5 meters, at the expense of the overall computation duration. The sensitivity of the Trinity River towards various projection scales is demonstrated (see Figure 5.11). Since the overall change in quality is difficult to measure, the sensitivity is demonstrated by means of visual interpretation. Noticeable differences can be observed to both the river polygon and the centerline. Specifically, simplified river polygons of relatively narrow rivers of which the pixel resolution is 20×20 meters or lower start to show large disparity in terms of the overall quality. The fact that the polygon breaks for lower resolutions makes sense, since fewer pixels are available when an image is downsampled, ultimately resulting in insufficient data points to render a polygon. The same applies to the centerline, since its overall quality, beside the interval at which vertices are computed (as mentioned in §4.2), is in fact based on the projection scale.

Secondly, the extent to which a geometry is simplified heavily influences the shape of the geometry. In §3.4, it was briefly mentioned that the Douglas-Peucker algorithm is used to do so, reducing the number of vertices within a polygon. In fact, the result is very similar to a reduction

of the pixel resolution (Figure 5.11). An increase of the simplification scale results in fewer vertices present within a river polygon.

Furthermore, the number of vertices that are used to compute the EDM affect the quality of the centerline. More specifically, the distance between those vertices is of importance, especially for very narrow channels, where a relatively high number of vertices is in fact necessary to compute the centerline. The differences for a small segment of the Trinity River can be seen in Figure 5.12.

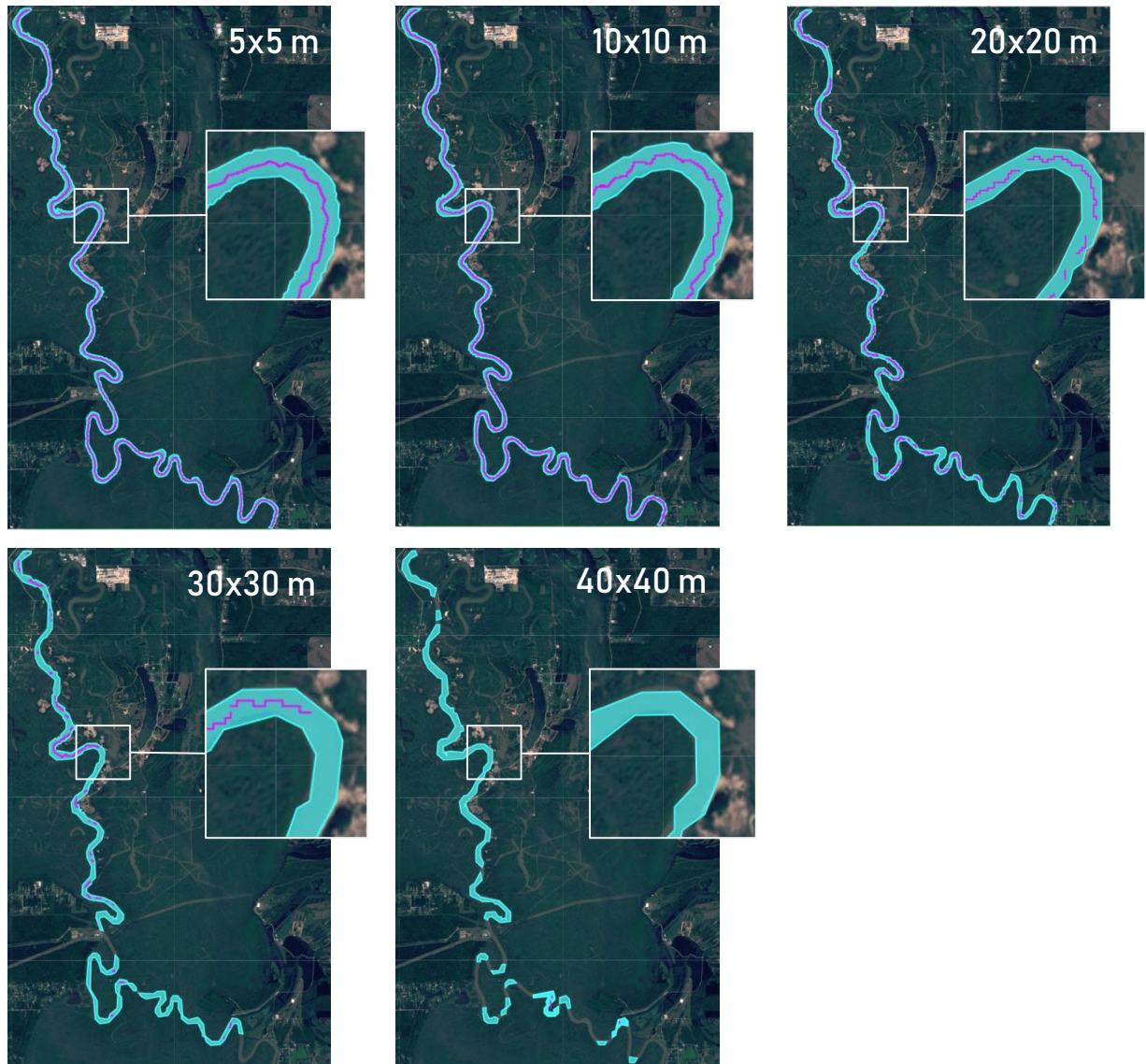


Figure 5.11 – The impact of various projection scales towards the quality of the estimated geometry of a river.

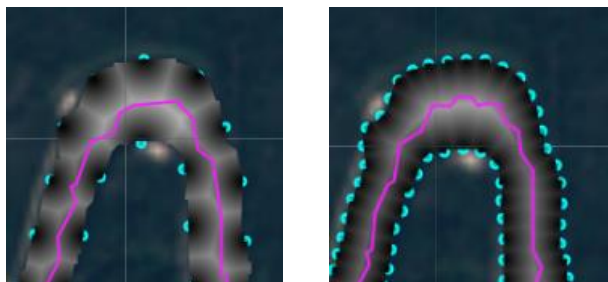


Figure 5.12 – The impact of the number of vertices used towards the quality of the EDM, and thus the centerline.

6. DISCUSSION

On the basis of previously conducted research, as well as existing concepts from various fields, this thesis introduced an approach that allows for the geometry of rivers to be detected in a more or less automated manner, both under cloudless and cloudy circumstances, using multispectral satellite imagery. A high-degree of similarity was found between river widths derived from river polygons that were estimated by means of multispectral satellite imagery, and river polygons provided by Rijkswaterstaat, showing that the geometry of a river can be determined reasonably accurately. However, clear distinctions from the GRWL dataset were found. Furthermore, it was found the geometry of a river can be estimated on a global level. However, their applicability remains limited to a local scale, mainly due to the fact that computations were found to be too resource-intensive in terms of memory usage, restraining the maximum size of a river polygon that can be generated.

Although the approach used to estimate the geometry of rivers based on multispectral satellite data appears to show reasonably accurate results, a critical evaluation of the study reveals the follows issues.

First of all, water indices (MNDWI, and NDWI in the presence of snow/ice) have been utilized to highlight water features, based on its proven accuracy and reliability throughout various studies. In terms of global application, this is likely not optimal, since Fisher et al. (2016) stated that no index was proven to perform the best across all water types. Although the results demonstrate that the geometry of rivers can be estimated reasonably accurately, the utilization of multiple indices might be worthwhile to look into.

Furthermore, interpolation techniques have been investigated to obtain more data points, resulting in a smoother representation of the bounds of a river. This was found to be necessary to derive reasonably accurate river widths from a river polygon, avoiding sudden large deviations due to a relatively large pixel resolution. However, doing so may introduce a small bias, which can result in a slight over- or underestimation of the estimated river width, since data points in between the known data points are estimated.

The approach towards the estimation of the course of a river under cloudy circumstances is currently flawed in case the stream width is highly variable over time (e.g. as a result of a highly variable discharge pattern). Under cloudy conditions, at least one cloudless image of which the stream width is similar to the stream width of the river of interest needs to be sampled to provide a reasonably accurate estimate. For example, consider the through of a discharge wave in between two peaks, which occur within a relatively short time frame. Additionally, assume that at a certain date of interest, which happens to be at said through, the satellite image is severely obstructed by clouds, such that most of the water occurrence composite represents the best estimate of the course of the river. Furthermore, assume that in this case the stream width of the river of interest is relatively narrow. The time span over which images that contribute to the water occurrence composite are sampled happens to be during both peaks of the discharge wave, resulting in a clear overestimation of the stream width, which is inaccurate. Although weights have been assigned to the sampled images in order to attempt to reduce the impact of highly varying surface water widths, unless cloudless satellite images can be sampled before large

variations occur, the water occurrence composite will still result in an overestimation. Since the revisit interval of a satellite is limited to either 5 days or 16 days, and only relatively cloudless images are suitable for the estimation of the course of a river under cloudy conditions, this issue might be challenging to solve. Certainly, to avoid this issue, the end-user could, in this case, manually sample a cloudless image that represents a reasonably accurate estimation of the river of interest. However, the ultimate goal is to provide a solution that works in an automated manner. Unfortunately, this issue could not be resolved. In Appendix F, typical scenarios where the method fails to provide a reasonably accurate representation of the course of a river are demonstrated.

To obtain an estimate of the geometry of a river under cloudy circumstances, a weight distribution of $p = 0.1$ was assumed, as well as a linear relationship between the kernel radius r and A_{ratio} , which was defined as the total water surface area of the historical composite divided by the total water surface area of the detected river, with upper and lower bounds of 1 and 1.5 respectively. Both distributions were found to be able to, generally, provide a reasonably accurate estimate of the course of a river (e.g. as seen in §4.1 and §4.2). However, depending on the variability of the water surface width over time, different values for p , r , or bounds for A_{ratio} may provide a more accurate estimation. This requires further testing towards multiple river types across the globe.

The accuracy of the method has been validated based on two river polygons provided by Rijkswaterstaat, showing reasonably good results. Additionally, similarities towards the GRWL dataset were found, for the same location. However, to truly obtain an understanding of the accuracy, and thus the overall usability on a global level, more tests on multiple river types across the globe are needed.

It was found that there is a chance that the estimated centerline of a river polygon might be incomplete (see §4.2), which is likely attributed to a geometry-intersection bug¹² within GEE. A workaround is necessary to avoid this issue in order to improve the reliability of an accurate result.

Nevertheless, the utilization of remote sensing technology allows for a significant reduction of the time needed to estimate the geometry of a river. The applicability of the procedure as shown in chapter 3 allows for the geometry of a river to be estimated within roughly 1 to 3 minutes, depending on the overall size. The need to manually draw a river polygon using a geographical map is in most cases no longer needed, unless the course of a river is found to be undetectable by either Landsat 8 or Sentinel-2. Although the approach functions in a more or less automated manner, small tweaks may still be necessary to obtain optimal results, such as the time span over which historical images are sampled, the distribution of the weights assigned to the sampled images, the extent to which the geometry or centerline is simplified, or the projection scale.

¹² See <https://groups.google.com/forum/#!searchin/google-earth-engine-developers/intersection%20bug%7Csort:date/google-earth-engine-developers/z65gS-lfaqQ/sQmpLXNDEQAJ>

7. CONCLUSIONS AND RECOMMENDATIONS

In this thesis, the extent to which the geometry of rivers around the globe can be determined in an automated manner, based on openly available optical Earth Observational (EO) satellite sensors, has been explored. This chapter consists of two sections. Firstly, the research questions are answered (§7.1). This leads to the objective of this research. Thereafter, recommendations for further work as well as recommendations for use are given (§7.2).

7.1 CONCLUSIONS

7.1.1 ANSWERS TO RESEARCH QUESTIONS

The following questions have been formulated in §1.4 in order to provide an answer to the objective of this thesis.

How can river bounds be detected in an automated manner, in case a multispectral satellite image is subject to common disturbances, such as clouds, haze or fog?

In order to detect surface water within a multispectral satellite image, water indices (both MNDWI and NDWI) have been utilized, followed by a HAND-map and an image thresholding approach (Otsu's method). The purpose of a water index is to enhance water features based on its reflective properties, the HAND-map to avoid potential errors due to shadows, and Otsu's method to reduce the resulting grayscale image to a binary surface water mask, separating water from non-water features. To estimate the bounds of a river under cloudy circumstances, multiple cloudless historical images are sampled to generate a composite, representing the water occurrence of a river over time in the form of a binary image. Sampled images are weighted based on the date they were sampled to potentially reduce the impact of variations within the stream width over time. The composite is used to fill the gaps within the course of a river, which were initially undetectable due to the presence of clouds. The resulting surface water mask is then converted to a smooth polygon, providing information about the course of a river.

How can river widths be determined in an automated manner, based on openly available multispectral satellite imagery?

Based on existing concepts, a method is proposed that allows for the river widths to be derived from a river polygon in an automated manner. This approach consists of three steps. First, a Euclidian distance map (EDM) is computed based on the known vertices within a river polygon, representing the distance of each pixel to its nearest boundary—that is, the nearest vertex. Secondly, the centerline of a river polygon is generated, which is derived from a Voronoi diagram that has subsequently been skeletonized and pruned. Lastly, values of the EDM that intersect with the computed centerline are sampled, resulting in knowledge about the width of a river.

The approach has been validated based on two river polygons provided by Rijkswaterstaat, representing a segment of the Meuse and the Rhine. The estimated geometries based on EO satellite imagery were found to be highly similar to that of the two river polygons. Throughout 2016, for a segment of the Meuse, deviations between +2 and -2 meters (+1.53% and -1.53%) as well as +1 and -8 meters (+0.76% and -6.11%) were found compared to data provided by Rijkswaterstaat, for cloudless and cloudy images respectively. For the segment that comprises of the Rhine and the Waal, deviations between +29 and -15 meters (+7.36% and -3.81%), and +17 and -13 meters (+4.31% and -3.30%) were found for cloudless and cloudy images respectively,

for the same year. Furthermore, the estimated geometries have been compared to a recently built database consisting of global river widths from Landsat imagery (GRWL), based on mean discharge data (Allen and Pavelsky, 2018). Similar river widths were found.

What is the global applicability of river polygons?

To assess the overall global applicability of the approach, river geometries have been estimated for seven rivers around the world, each displaying various features (e.g. meandering, braiding, point bars, medial bards, islands and varying sizes). Although reasonable representations of the bounds of the selected rivers could be estimated, it was found that the maximum size of a river polygon is limited, due to the fact that computations were found to be too resource-intensive in terms of memory usage. Optimizations of some sort are necessary to be able to resolve this issue, or access to more memory, since the maximum amount of usable memory is limited within GEE. Another notable constraint is that the generation of river polygons is limited to rivers that are at least three to four times the width of the corresponding satellite's spatial resolution in order to obtain usable results. Relatively small water features were found to be undetectable using either Landsat 8 or Sentinel-2, of which the spatial resolution is 30×30 and 10×10 meters respectively. All in all, it was found that river geometries can be estimated global level, however their applicability is currently limited to a local scale.

What is the sensitivity of parameters that directly influence the geometry of a river polygon?

Beside the utilization of water indices to detect water, the estimated geometry of a river under cloudy conditions is found to be the most sensitive towards the following parameters: (1) the time span over which historical images are sampled, (2) the corresponding weights assigned to those images, (3) the severity of erosion, and four parameters that directly affect the quality of the result, that is (4) the resampling technique, (5) the pixel resolution (projection scale), (6) the extent to which geometry is simplified and the (7) number of vertices used to generate the EDM, which directly affects the quality of the centerline. (1), (2) and (3) do not apply to cloudless conditions. The sensitivity towards varying sampling windows highly depends on variations within the stream width over time (e.g. as a result of a highly variable discharge pattern), as well as the distribution of the weights assigned to the sampled images. The sensitivity towards erosion depends on the size of the kernel radius. Furthermore, the shape of the geometry drastically changes if it is either bilinearly or bicubically interpolated. The same applies to different values for (5) and (6).

7.2 RECOMMENDATIONS

7.2.2 RECOMMENDATIONS FOR FURTHER WORK

It has been shown that the geometry of rivers can be estimated on various locations around the globe using optical EO sensors. However, the applicability of the method is currently limited to a local scale (see §4.1 and §4.2). The following recommendations are proposed to not only allow for the estimation of the geometry of a river on a global scale, but to also improve the reliability of the method as a whole:

1. In terms of the detection of surface water, this study utilizes the MNDWI as a result of its proven effectiveness to separate water from non-water features (NDWI in case of ice/snow). However, Fisher et al. (2016) stated that no index was proven to perform the

best across all water types. Further research towards to utilization of varying indices around the globe, and, an automated selection of a certain water index based on the properties of water will likely improve the results in terms of accuracy. However, more recent studies seem to steer into the direction of image classification methods based on machine learning, demonstrating surprisingly good results (e.g. Chen et al., 2018 and Acharya et al., 2018).

2. The approach towards the estimation of the course of a river under cloudy circumstances is currently flawed in case the water surface width is highly variable over time (e.g. as a result of a highly variable discharge pattern). Under cloudy conditions, at least one cloudless image of which the stream width is similar to the stream width of the river of interest needs to be sampled to provide a reasonably accurate estimate. Although weights have been assigned to the sampled images, in case of limited amount of available cloudless images to sample from within a short period of time, this does not prevent an over- or underestimation of the geometry of a river. Since the revisit intervals of satellites are fixed in time, and thus the number of usable images is limited, improved logic is necessary to avoid this issue. Even though, in this particular case, a proper cloudless image could be sampled manually to avoid this issue, this defeats the purpose of an automated method.
3. Currently, to find the centerline within a Voronoi-based skeleton, polygons are intersected in order to figure out where the bounds of said polygons overlap. However, for some unexplainable reason, this sometimes fails in GEE. According to a post on the GEE developers forum by Donchyts, this is likely to be a bug¹³. A workaround has yet to be found. In order to ensure that generation of the centerline is reliable under any condition, it is highly recommended that a solution towards this issue is found.
4. Furthermore, to be able to quickly sample the river widths from any start to end point within the estimated geometry, the implementation of a pathfinding algorithm along the centerline is recommended.
5. Any form of obstruction, whether that is a cloud or a bridge, results in the inability to detect water. Although most obstructions can be avoided based on historical satellite images, bridges cannot, which will often result in disconnected polygons. A workaround needs to be found to avoid this issue.
6. Currently, the biggest limitation is the size of a geometry that can be estimated. Resultant objects that may be too big, or too numerous, could not be computed due to memory limitations within GEE. Optimizations of some sort are necessary to mitigate, or completely avoid this issue.
7. The estimation of the geometry of a river ultimately depends on the freely available EO satellite data that is used—either Landsat 8 or Sentinel-2 data in this case. However, many

¹³ Example: <https://code.earthengine.google.com/27e508824057efa520d1a68233a05198>
GEE developers forum post: <https://groups.google.com/forum/#!searchin/google-earth-engine-developers/intersection%20bug%7Csort:date/google-earth-engine-developers/z65gS-lfaqQ/sQmpLXNDEQAJ>

more datasets are available with a much higher resolution, some of which are of commercial nature (e.g. as listed in Table 2.1). Although the utilization of both Landsat 8 and Sentinel 2 is usually sufficient, their resolution may be inadequate in case smaller water features are of importance. The addition of more datasets may improve the accuracy of the results, as well allow for more data to sample from.

Based on the approach as outlined in this thesis, the estimation of the geometry of a river should, in theory, work on any scale, as long as a cloudless binary surface water mask of the river network can be computed. Under the assumption that this can be achieved for a large scale, and the issue as stated in (3) is resolved, it is expected that the geometry of the river network can be estimated reliably, assuming the resources are given to do so.

7.2.1 RECOMMENDATIONS FOR USE

In order to make use of the overall method, a total of three mandatory parameters require manual input by the end-user. Furthermore, several more optional parameters allow for the refinement of the results. What follows is a list of parameters that may be altered by the end-user.

Mandatory input parameters:

- *Satellite selection*
A satellite of choice must be selected between Landsat 8 and Sentinel-2, which serves as the main data source. Note that the spatial resolutions of both satellites are 30×30 and 10×10 meters respectively. Furthermore, Landsat 8 data is available from 11-04-2013 and onwards. Sentinel-2 data is available from 23-06-2015 and onwards. In order to retrieve the most accurate river polygon, the Sentinel-2 is recommended. If Sentinel-2 imagery is unavailable, Landsat-8 should be selected.
- *Date of interest*
A start and end date should be given, where the first (most recent relative to defined start date) multispectral satellite image in the list is selected.
- *Area of interest*
To define the specific river of interest, the bounds must be clearly defined. To do so, a square or polygon must be drawn on the presented geographical map. Surface water that is not located within the predefined bounds are excluded.

Optional input parameters:

- *Historical data sampling range (defaults to 120 days)*
Wherever the course of a river is not visible due to possible image obstructions, the classification of a pixel is estimated based on a series of a historical images, resulting in a composite image representing the water occurrence. This parameter defines the amount of days that are considered, relative to a certain date of interest. For example: Assume the date of interest is set to 01-01-2018 and the parameter is set to 120 days, then all historical satellite images relative to that point in time are considered; that is, every satellite image between 03-09-2017 and 01-05-2018 (so, -120 and +120 relative to a

certain date of interest). Generally, a sampling time span of 4 months is found to be more than sufficient.

- *Historical data: cut-off threshold (defaults to 0.2)*

This parameter is directly related to “*Range of historical data*”. To compute a composite water occurrence image, which consists of a sum of binary images, pixel values that are below a certain threshold value are excluded. This is ultimately done to remove clouds and detect the general bounds of a river of interest. The setting is set to 0.2 by default, removing any pixel of which the sum of the binary images is less or equal than 20% of the total sum. It is demonstrated that this threshold value works well and is thus recommended.

- *Geometry subtraction (turned off by default)*

This parameter allows for the removal of any water body that is directly connected to the main river polygon, such as a harbor or a bifurcation. Multiple custom shapes can be drawn on the geographical map, resulting in any water body that is bounded by the shape to be excluded from the river polygon. Alternatively, the coordinates of the vertices of a custom shape may be provided. By default, this particular parameter does not influence the estimated river polygon in any way.

- *River width threshold range (turned off by default)*

To exclude water bodies from the river polygon that are considered to be irrelevant, a minimum and maximum river width may be defined. Any detected water body that does not fall within the given range is excluded. This may sometimes require a trial-and-error approach to do so successfully. This computation is found to be resource-intensive due to the fact that the mean width has to be computed for every water body present within an image. Instead, it is recommended that the area of interest is selected in such a way, that the river of interest is the largest water body within an image, which will subsequently be recognized automatically.

- *Projection scale (defaults to 10×10 meters)*

This particular parameter is dedicated to the scale at which the river polygon and the corresponding centerline is projected (also known as the pixel resolution). A projection scale of 10×10 meters is recommended to produce seemingly accurate results. Higher projection scales are possible but becoming increasingly resource-intensive. Lower projection scales (e.g. 10×10 meters or 30×30 meters) are recommended for the estimation of the geometry of a river that is relatively large.

- *Maximum number of vertices per polygon (defaults to a cap of 500 vertices)*

The quality of both the Euclidian distance map and the Voronoi-based skeleton are based on the number of vertices within a river polygon. In turn, the number of vertices within a river polygon is directly related to the projection scale. To prevent calculations that may be too resource-intensive, the maximum number of vertices is capped at an arbitrary number (500) by default.

- *Prune scale factor (defaults to 1)*

In order to remove undesirable branches from the Voronoi-based skeleton, they are pruned based on the distance of a branch point to its nearest boundary, in Euclidian space.

To exclude branches that are relatively far away from a branch point, the search radius may be arbitrarily expanded by increasing the scale multiplier.

- *Simplification factor (defaults to 1.5 times the projection scale)*
For optimization purposes, the number of vertices within a river polygon are reduced by means of simplification (as explained in §3.4). A similar variable is available for the simplification of the centerline.

- *Resample (defaults to bilinear)*
In order to achieve a smooth river polygon, the initially obtained polygon is resampled. Bilinear interpolation was found to be faster over bicubic interpolation, while minimizing the loss of quality, and is recommended as the default option. Other options are bicubic or nearest neighbor interpolation (default in GEE).

- *Power parameter p (defaults to 0.1)*
This variable specifies the distribution of the weights (see Figure 5.4) that are assigned to the sampled images, used to generate the historical composite.

- *K (defaults to [1, 1.5])*
This variable specifies the proportionality of the linear relationship between the kernel radius r and A_{ratio} .

REFERENCES

- Acharya T. D., Subedi A., Huang H., Lee D. H., Classification of Surface Water using Machine Learning Methods from Landsat Data in Nepal (2018). Proceedings of 5th International Electronic Conference on Sensors and Applications, 1 (doi: 10.3390/ecs-a-5-05833)
- Acharya, T. D., Lee, D. H., Yang, I. T., & Lee, J. K. (2016). Identification of water bodies in a Landsat 8 OLI image using a J48 Decision Tree. *Sensors*, 16 (7), 1075.
- Alabyan, M. A., and Chalo S. C., (1998). Types of river channel patterns and their natural controls. *Earth Surface Processes and Landforms*. 23. 467 - 474. 10.1002/(SICI)1096-9837(199805)23:5<467::AID-ESP861>3.0.CO;2-T.
- Allen, G. H., & Pavelsky, T. M. (2015). Patterns of river width and surface area revealed by the satellite-derived North American River Width data set. *Geophysical Research Letters*, 42, 395–402. <https://doi.org/10.1002/2014GL062764>
- Beltman M. (2016) Exploring the D-RATIN tool. Studying inland navigation potential using a rapid assessment tool, Universiteit Twente (bachelor thesis)
- Burrough, P.A. (1986) Principles of Geographic Information Systems for Land Resource Assessment. Monographs on Soil and Resources Survey No. 12, Oxford Science Publications, New York.
- Brandt, Jonathan & Algazi, V. (1992). Continuous skeleton computation by Voronoi diagram. *CVGIP: Image Understanding*. 55. 329-338. 10.1016/1049-9660(92)90030-7.
- Chen, Yang & Fan, Rongshuang & Yang, Xiucheng & Wang, Jingxue & Latif, Aamir. (2018). Extraction of Urban Water Bodies from High-Resolution Remote-Sensing Imagery Using Deep Learning. *Water*. 10. 585. 10.3390/w10050585.
- Choi, H., and Bindschadler, R. (2004). Cloud detection in Landsat imagery of ice sheets using shadow matching technique and automatic normalized difference snow index threshold value decision. *Remote Sensing of Environment*, 91(2), 237–242. <https://doi.org/10.1016/j.rse.2004.03.007>
- Chowdary, V. M., Chandran, R. V., Neeti, N., Bothale, R. V., Srivastava, Y. K., Ingle, P., et al. (2008). Assessment of surface and sub-surface waterlogged areas in irrigation command areas of Bihar state using remote sensing and GIS. *Agricultural Water Management*, 95(7), 754–766. <https://doi.org/10.1016/j.agwat.2008.02.009>
- Crist, E. P. (1985). A TM Tasseled Cap equivalent transformation for reflectance factor data. *Remote Sensing of Environment*, 17(3), 301–306. [https://doi.org/10.1016/0034-4257\(85\)90102-6](https://doi.org/10.1016/0034-4257(85)90102-6)
- Domenikiotis, C., Loukas, A., & Dalezios, N. R. (2003). The use of NOAA/AVHRR satellite data for monitoring and assessment of forestfires and flood. *Natural Hazards and Earth System Sciences*, 3, 115–128.
- Donchyts, G., (2018). Planetary-scale surface water detection from space. doi:10.4233/uuid:510bd39f-407d-4bb6-958e-dea363c5e2a8 (PhD dissertation)
- Donchyts, G., Schellekens, J., Winsemius, H., Eisemann, E., & van de Giesen, N. (2016). A 30 m resolution surface water mask including estimation of positional and thematic differences using Landsat 8, SRTM and OpenStreetMap: A case study in the Murray-Darling Basin, Australia. *Remote Sensing*, 8(5), 386.
- Douglas, D.H. and Peucker, T.K., 1973. Algorithms for the reduction of the number of points required to represent a digitized line or its caricature. *Cartographica: The International Journal for Geographic Information and Geovisualization*, 10(2): 112-122.
- Du, Y., Zhang, Y., Ling, F., Wang, Q., Li, W., & Li, X. (2016). Water bodies' mapping from Sentinel-2 imagery with modified normalized difference water index at 10-m spatiresolution produced by sharpening the SWIR band. *Remote Sensing*, 8(4), 354.
- Du, Z., Li, W., Zhou, D., Tian, L., Ling, F., Wang, H., et al. (2014). Analysis of Landsat-8 OLI imagery for land surface water mapping. *Remote Sensing Letters*, 5(7), 672–681. <https://doi.org/10.1080/2150704X.2014.960606>
- Fabbri, R., Costa, L., Torrelli, J., Bruno, O. (2008). 2d Euclidean Distance Transform Algorithms: A comparative survey. *ACM Computing Surveys* 40.
- Feyisa, G. L., Meilby, H., Fensholt, R., & Proud, S. R. (2014). Automated water extraction index: A new technique for surface water mapping using Landsat imagery. *Remote Sensing of Environment*, 140(0), 23–35. <https://doi.org/10.1016/j.rse.2013.08.029>

7. CONCLUSIONS AND RECOMMENDATIONS

- Fisher, A., Flood, N., & Danaher, T. (2016). Comparing Landsat water index methods for automated water classification in eastern Australia. *Remote Sensing of Environment*, 175, 167–182. <https://doi.org/10.1016/j.rse.2015.12.055>
- Frazier, P. S., & Page, K. J. (2000). Water body detection and delineation with Landsat TM data. *Photogrammetric Engineering and Remote Sensing*, 66(12), 1461–1467.
- Gallant, J. C., & Dowling, T. I. (2003). A multiresolution index of valley bottom flatness for mapping depositional areas. *Water Resources Research*, 39(12), 1347. <https://doi.org/10.1029/2002WR001426>
- Gao, H., Wang, L., Jing, L., & Xu, J. (2016). An effective modified water extraction method for Landsat-8 OLI imagery of mountainous plateau regions. Paper presented at IOP Conference Series: Earth and Environmental Science, Beijing, China.
- Gianinetto, M., Villa, P., & Lechi, G. (2006). Post flood damage evaluation using landsat TM and ETM plus data integrated with DEM. *IEEE Transactions on Geoscience and Remote Sensing*, 44(1), 236–243. <https://doi.org/10.1109/tgrs.2005.859952>
- Gunderson, A., & Chodas, M. (2011). An investigation of cloud cover probability for the HyspIRI mission using MODIS cloud mask data. Paper presented at 2011 IEEE Aerospace Conference, Big Sky, MT, USA
- Hansen, M.C.; Potapov, P.V.; Moore, R.; Hancher, M.; Turubanova, S.A.; Tyukavina, A.; Thau, D.; Stehman, S.V.; Goetz, S.J.; Loveland, T.R.; et al. High-resolution global maps of 21st-century forest cover change. *Science* 2013, 342, 850–853.
- Hoberg T., Rottensteinerv F., Feitosa R. Q., and Heipke C., Conditional random fields for multitemporal and multiscale classification of optical satellite imagery. *IEEE Transactions on Geoscience and Remote Sensing*, 53(2):659–673, 2015.
- Huang, C., Chen, Y., Zhang, S., Wu, J (2018). Detecting, extracting, and monitoring surface water from space using optical sensors: A review. *Rev. Geophys.* 2018, 56, 333–360.
- Hui, F. M., Xu, B., Huang, H. B., Yu, Q., & Gong, P. (2008). Modelling spatial-temporal change of Poyang Lake using multitemporal Landsat imagery. *International Journal of Remote Sensing*, 29(20), 5767–5784. <https://doi.org/10.1080/01431160802060912>
- Ji, L. Y., Geng, X. R., Sun, K., Zhao, Y. C., & Gong, P. (2015). Target detection method for water mapping using Landsat 8 OLI/TIRS imagery. *Water*, 7(2), 794–817. <https://doi.org/10.3390/w7020794>
- Ji, L., Zhang, L., & Wylie, B. (2009). Analysis of dynamic thresholds for the normalized difference water index. *Photogrammetric Engineering and Remote Sensing*, 75(11), 1307–1317.
- Kokaly, R.F., Clark, R.N., Swayze, G.A., Livo, K.E., Hoefen, T.M., Pearson, N.C., Wise, R.A., Benzel, W.M., Lowers, H.A., Driscoll, R.L., and Klein, A.J., 2017, USGS Spectral Library Version 7: U.S. Geological Survey Data Series 1035, 61 p., <https://doi.org/10.3133/ds1035>.
- Kokaly, R.F., Clark, R.N., Swayze, G.A., Livo, K.E., Hoefen, T.M., Pearson, N.C., Wise, R.A., Benzel, W.M., Lowers, H.A., Driscoll, R.L., and Klein, A.J., 2017, USGS Spectral Library Version 7 Data: U.S. Geological Survey data release, <https://dx.doi.org/10.5066/F7RR1WDJ>.
- Kummu M., de Moel H., Ward P.J., Varis O. (2011), How Close Do We Live to Water? A Global Analysis of Population Distance to Freshwater Bodies. *PLoS ONE* 6(6): e20578. doi:10.1371/journal.pone.0020578
- Li, J. L., & Sheng, Y. W. (2012). An automated scheme for glacial lake dynamics mapping using Landsat imagery and digital elevation models: A case study in the Himalayas. *International Journal of Remote Sensing*, 33(16), 5194–5213. <https://doi.org/10.1080/01431161.2012.657370>
- Li, S., Sun, D., Yu, Y., Csaszar, I., Stefanidis, A., & Goldberg, M. D. (2013). A new Short-Wave Infrared (SWIR) method for quantitative water fraction derivation and evaluation with EOS/MODIS and Landsat/TM data. *IEEE Transactions on Geoscience and Remote Sensing*, 51(3), 1852–1862. <https://doi.org/10.1109/tgrs.2012.2208466>
- Li, Y., Gong, X., Guo, Z., Xu, K., Hu, D., & Zhou, H. (2016). An index and approach for water extraction using Landsat–OLI data. *International Journal of Remote Sensing*, 37(16), 3611–3635. <https://doi.org/10.1080/01431161.2016.1201228>
- Liu, Z., Yao, Z., & Wang, R. (2016). Assessing methods of identifying open water bodies using Landsat 8 OLI imagery. *Environment and Earth Science*, 75(10), 1–13.
- Lou X., Huang V., Shi A., Tcng J., (2005). Raster to vector conversion of classified remote sensing image. *Geoscience and Remote Sensing Symposium IGARSS-05 Proceedings. IEEE International* 5: 3656–3658

7. CONCLUSIONS AND RECOMMENDATIONS

- Manavalan, P., Sathyanath, P., & Rajegowda, G. L. (1993). Digital image analysis techniques to estimate waterspread for capacity evaluations of reservoirs. *Photogrammetric Engineering and Remote Sensing*, 59(9), 1389–1395.
- McFeeters, S. K. (1996). The use of the normalized difference water index (NDWI) in the delineation of open water features. *International Journal of Remote Sensing*, 17(7), 1425–1432.
- Meijster, A. (2004). *Efficient sequential and parallel algorithms for morphological image processing* Groningen: s.n.**
- Mercury, M., Green, R., Hook, S., Oaida, B., Wu, W., Gunderson, A., & Chodas, M. (2012). Global cloud cover for assessment of optical satellite observation opportunities: A HypsIRI case study. *Remote Sensing of Environment*, 126(Supplement C), 62–71. <https://doi.org/10.1016/j.rse.2012.08.007>
- Olthof, I. (2017). Mapping seasonal inundation frequency (1985–2016) along the St-John River, New Brunswick, Canada using the Landsat archive. *Remote Sensing*, 9(2), 143.
- Ozesmi, S. L., & Bauer, M. E. (2002). Satellite remote sensing of wetlands. *Wetlands Ecology and Management*, 10(5), 381–402. <https://doi.org/10.1023/a:1020908432489>
- Pekel, J.-F., Cottam, A., Gorelick, N., & Belward, A. S. (2016). High-resolution mapping of global surface water and its long-term changes. *Nature*, 540(7633), 418.
- Potapov, P.V.; Turubanova, S.A.; Hansen, M.C.; Adusei, B.; Broich, M.; Altstatt, A.; Mane, L.; Justice, C.O. (2012) Quantifying forest cover loss in Democratic Republic of the Congo, 2000–2010, with Landsat ETM+ data. *Remote Sens. Environ.*, 122, 106–116.
- Phillips J.D., Slattery M.C. & Musselman Z.A. (2004) Dam-to-delta sediment inputs and storage in the lower Trinity River, Texas. *Geomorphology*, 62, 17–34.
- Qi, S. H., Brown, D. G., Tian, Q., Jiang, L. G., Zhao, T. T., & Bergen, K. A. (2009). Inundation extent and flood frequency mapping using LANDSAT imagery and Digital Elevation Models. *GIScience & Remote Sensing*, 46(1), 101–127. <https://doi.org/10.2747/1548-1603.46.1.101>
- Rennó, C. D., Nobre, A. D., Cuartas, L. A., Soares, J. V., Hodnett, M. G., Tomasella, J., & Waterloo, M. J. (2008). HAND, a new terrain descriptor using SRTM-DEM: Mapping terra-firme rainforest environments in Amazonia. *Remote Sensing of Environment*, 112(9), 3469–3481. <https://doi.org/10.1016/j.rse.2008.03.018>
- Riekert, W.-F. (1993). Extracting area objects from raster image data. *IEEE Computer Graphics and Applications*, 13(2), 68–73. doi:10.1109/38.204969
- Salomonson, V. V., and Appel, I. (2004). Estimating fractional snow cover from MODIS using the normalized difference snow index. *Remote Sensing of Environment*, 89(3), 351–360. <https://doi.org/10.1016/j.rse.2003.10.016>
- Schumann, G. J. P., & Moller, D. K. (2015). Microwave remote sensing of flood inundation. *Physics and Chemistry of the Earth*, 83–84, 84–95. <https://doi.org/10.1016/j.pce.2015.05.002>
- Sheng, Y. W., Su, Y. F., & Xiao, Q. G. (1998). Challenging the cloud-contamination problem in flood monitoring with NOAA/AVHRR imagery. *Photogrammetric Engineering and Remote Sensing*, 64(3), 191–198.
- Shepard, Donald. (1968). A Two-Dimensional Interpolation Function for Irregularly-Spaced Data. *ACM National Conference*. 23. 517-524. 10.1145/800186.810616.
- Singh, K., Ghosh, M., & Sharma, S. R. (2016). WSB-DA: Water Surface Boundary Detection Algorithm using Landsat 8 OLI data. *IEEE Journal of Selected Topics Applied Earth Observation Remote Sensing*, 9(1), 363–368. <https://doi.org/10.1109/JSTARS.2015.2504338>
- Solís Montero, A., Lang, J., 2012. Skeleton pruning by contour approximation and the integer medial axis transform. *Comput. Graph.* 36, 477–487.
- Sun, D. L., Yu, Y. Y., & Goldberg, M. D. (2011). Deriving water fraction and flood maps from MODIS images using a decision tree approach. *IEEE Journal of Selected Topics Applied Earth Observation Remote Sensing*, 4(4), 814–825. <https://doi.org/10.1109/jstars.2011.2125778>
- Tagliasacchi, Andrea & Delame, Thomas & Spagnuolo, Michela & Amenta, Nina & Telea, Alexandru. (2016). 3D Skeletons: A State-of-the-Art Report. *Computer Graphics Forum*. 35. 10.1111/cgf.12865.

7. CONCLUSIONS AND RECOMMENDATIONS

- Ward, D. P., Petty, A., Setterfield, S. A., Douglas, M. M., Ferdinands, K., Hamilton, S. K., & Phinn, S. (2014). Floodplain inundation and vegetation dynamics in the Alligator Rivers region (Kakadu) of northern Australia assessed using optical and radar remote sensing. *Remote Sensing of Environment*, 147(Supplement C), 43–55. <https://doi.org/10.1016/j.rse.2014.02.009>
- Wylie, D., Jackson, D. L., Menzel, W. P., & Bates, J. J. (2005). Trends in global cloud cover in two decades of HIRS observations. *Journal of Climate*, 18(15), 3021–3031. <https://doi.org/10.1175/JCLI3461.1>
- Xie, H., Luo, X., Xu, X., Pan, H., & Tong, X. (2016). Evaluation of Landsat 8 OLI imagery for unsupervised inland water extraction. *International Journal of Remote Sensing*, 37(8), 1826–1844. <https://doi.org/10.1080/01431161.2016.1168948>
- Xu, H. Q. (2006). Modification of normalized difference water index (NDWI) to enhance open water features in remotely sensed imagery. *International Journal of Remote Sensing*, 27(14), 3025–3033.
- Yang K. and Smith L. C., (2013). “Supraglacial streams on the Greenland Ice Sheet delineated from combined spectral-shape information in high-resolution satellite imagery,” *IEEE Geosci. Remote Sens. Lett.*, vol. 10, no. 4, pp. 801–805.
- Yang, Xiucheng & Zhao, Shanshan & Qin, Xuebin & Zhao, Na & Liang, Ligang. (2017). Mapping of Urban Surface Water Bodies from Sentinel-2 MSI Imagery at 10 m Resolution via NDWI-Based Image Sharpening. *Remote Sensing*. 9. 596. [10.3390/rs9060596](https://doi.org/10.3390/rs9060596).
- Yang, Y., Liu, Y., Zhou, M., Zhang, S., Zhan, W., Sun, C., & Duan, Y. (2015). Landsat 8 OLI image based terrestrial water extraction from heterogeneous backgrounds using a reflectance homogenization approach. *Remote Sensing of Environment*, 171, 14–32. <https://doi.org/10.1016/j.rse.2015.10.005>
- Zervakis D.I (2015) Combining a Physics-based Model and Spatial Interpolation of Scarce Bed Topography Data in Meandering Alluvial Rivers, TUDelft (master thesis)

APPENDIX A: OTSTU THRESHOLDING & CANNY EDGE DETECTOR

A.1 OTSU THRESHOLDING

The sole purpose of Otsu's method (Otsu, 1975) in this thesis is to convert a gray level image, which is obtained by computing the spectral index (e.g. MNDWI) of a multispectral satellite image, to a binary image (consisting of water (white) and non-water pixels (black)). To do so, the method iterates through all possible threshold values and calculates the measure of spread for all pixel values at each side of the threshold. The threshold value separates the image into so called foreground and background pixels T_0 and T_1 , where $T_0 = \{0, 1, \dots, t\}$ and $T_1 = \{t, t + 1, \dots, l\}$, with t being the threshold value and l the maximum gray level in the image (e.g., 256). The optimal threshold value is the value with the minimum within-class variance, which is the sum of the foreground and background variances multiplied by their associated weights. The within-class variance is defined as:

$$\sigma_w^2(t) = w_b(t)\sigma_b^2(t) + w_f(t)\sigma_f^2(t) \quad (\text{A.1})$$

where σ_w^2 is the intra-class variance, t the threshold value, w_b and w_f the weights of the background and foreground pixels, and σ_b^2 and σ_f^2 the variances of the background and foreground pixels respectively. Furthermore, the weights, means and variances are defined as:

$$w_b(t) = \sum_{i=1}^t P(i) \quad (\text{A.2})$$

$$w_f(t) = \sum_{i=t+1}^l P(i) \quad (\text{A.3})$$

$$\mu_b(t) = \frac{\sum_{i=1}^t i \times P(i)}{w_b(t)} \quad (\text{A.4})$$

$$\mu_f(t) = \frac{\sum_{i=t+1}^l i \times P(i)}{w_f(t)} \quad (\text{A.5})$$

$$\sigma_b^2(t) = \frac{\sum_{i=1}^t (i - \mu_b(t))^2 \times P(i)}{w_b(t)} \quad (\text{A.6})$$

$$\sigma_f^2(t) = \frac{\sum_{i=t+1}^l (i - \mu_f(t))^2 \times P(i)}{w_f(t)} \quad (\text{A.7})$$

With $P(i) = \frac{i}{r \times c}$, where i is the observed gray value at a specific row r and column c . In an experimental study, Yousefi (2011) tested the performance of Otsu thresholding and found that Gaussian Otsu thresholding, an extension of the Otsu thresholding technique, performs faster than Otsu's method. This approach maximizes the between-class variance, instead of minimizing the within-class variance:

$$\sigma_b^2(t) = \sigma^2 - \sigma_w^2(t) = w_b \times w_f \times (\mu_b(t) - (\mu_f(t)))^2 \quad (\text{A.8})$$

where σ^2 is the total variance. The maximum of equation A.7 is used.

A.2 CANNY EDGE DETECTOR

The Canny edge detector is a widely used method applied in computer vision systems and is a technique which allows for the accurate detection of edges in images (Canny, 1986). In this thesis, it is used on binary images where the boundaries between water and non-water pixels are clearly defined. The algorithm operates as follows:

1. Image smoothing – Generally, edge detectors are prone to noise. Therefore, the image is smoothed with a square-sized Gaussian structural element, usually of 5×5 size.
2. Gradient intensity calculation – The gradient magnitudes and directions are computed. The gradient magnitude defines the edge. A high gradient magnitude translates to a rapid change in color (an edge); a low gradient magnitude does not. The gradient direction, as the name implies, defines the orientation of the edge. Both terms are defined as follows:

$$G = \sqrt{G_x^2 + G_y^2} \quad (\text{A.9})$$

$$\theta = \tan^{-1}\left(\frac{G_y}{G_x}\right) \quad (\text{A.10})$$

where G_x and G_y are the x and y derivatives of the current pixel. The gradient directions are rounded to either 0, 45, 90 or 135 degrees (vertically, horizontally and two diagonals).

3. Non-maximum suppression – Pixels that are not maximum values are suppressed, resulting in very thin edges. This is done by iterating over all pixels, followed by a scan that checks if the current pixel is a local maximum in its neighborhood.
4. Hysteresis thresholding – This stage removes small pixel noises based on two threshold values of the intensity gradient, and discards pixels below a certain threshold.

Google Earth Engine supplies a built-in interpretation of Canny's edge detection algorithm which is utilized to compute the edges.

APPENDIX B: MORPHOLOGICAL OPERATORS

Morphological operators, specifically erosion, dilation and opening are applied in this thesis in order to perform manipulations on binary images, and are commonly used in the processing of digital images. A binary image can be interpreted as a two-dimensional grid in Euclidean space, where white pixels (1's) represent the foreground—in this case water—and black pixels (0's) serve as background pixels. By sliding a structural element, or a kernel—which is simply a $n \times m$ -sized matrix—to each position in the binary image (e.g. by iterating over the rows and columns of an image), it is possible to manipulate the values within a binary image (or any image for that matter). Differently shaped kernels can be obtained by strategically placing the values within the matrix (e.g. square, circle, cross, diamond). Erosion, dilation and opening can be explained as follows:

Erosion

- Erosion shrinks (erodes) the connected sets of 1's of a binary image and can be used for shrinking features or removing connections or branches. For example, assume a 3×3 kernel filled with 1's and a binary image filled with 1's and 0's. The kernel is moved over the binary image. If and only if the kernel completely overlaps a 3×3 space consisting of 1's within the binary image, the new binary image is assigned the value 1 at the current position of the center of the kernel. Wherever this is not the case, the resulting pixel values are 0. The erosion of binary image A by the kernel B can be written as:

$$A \ominus B = \{b \mid \text{for all } a \in A, a + b \in B\} \quad (\text{B.1})$$

i.e., place the kernel anywhere within the binary image and if it is a subset, the origin of the kernel is part the eroded image. Here, \ominus represents the erosion operator. An example is illustrated in Figure B.1.

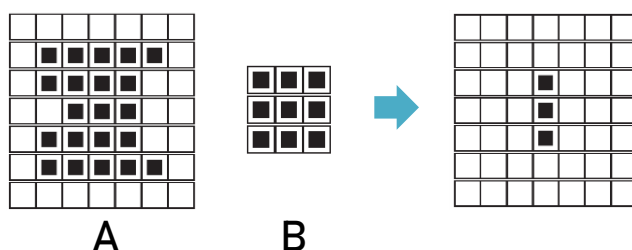


Figure B.1— Erosion of binary image A by kernel B .

Dilation

- Dilation expands (dilates) the connected sets of 1's of a binary image and can be used for growing features or filling holes and gaps. Like erosion, assume a 3×3 kernel filled with 1's that is moved over a binary image. This time, if one single coordinate that is assigned the value 1 within the kernel intersects a 1 within the binary image, the new binary image is assigned the value 1 at the current position of the center of the kernel. Otherwise, a 0 is assigned to the new binary image. The dilation of binary image A by the kernel B can be written as:

$$A \oplus B = \{a + b \mid a \in A \text{ and } b \in B\} \quad (\text{B.2})$$

i.e., the set of all possible additions of an element of A and an element of B , where \oplus represents the dilation operator. An example is illustrated in Figure B.2.

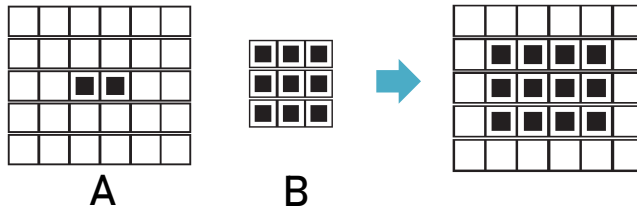


Figure B.2— Dilation of binary image A by kernel B .

Opening

- Opening is simply erosion followed by dilation, and may be useful for removing noise (e.g. relatively small water bodies). The operator can be written as:

$$A \circ B = (A \ominus B) \oplus B \quad (\text{B.3})$$

where \circ denotes opening, \ominus erosion and \oplus dilation.

APPENDIX C: OVERLAPPED RIVER POLYGONS

The same images as demonstrated in Figure 4.1 and 4.6 are illustrated below. However, in this case, the EO satellite-based river polygons (cyan) and those provided by Rijkswaterstaat (orange) are overlapped.

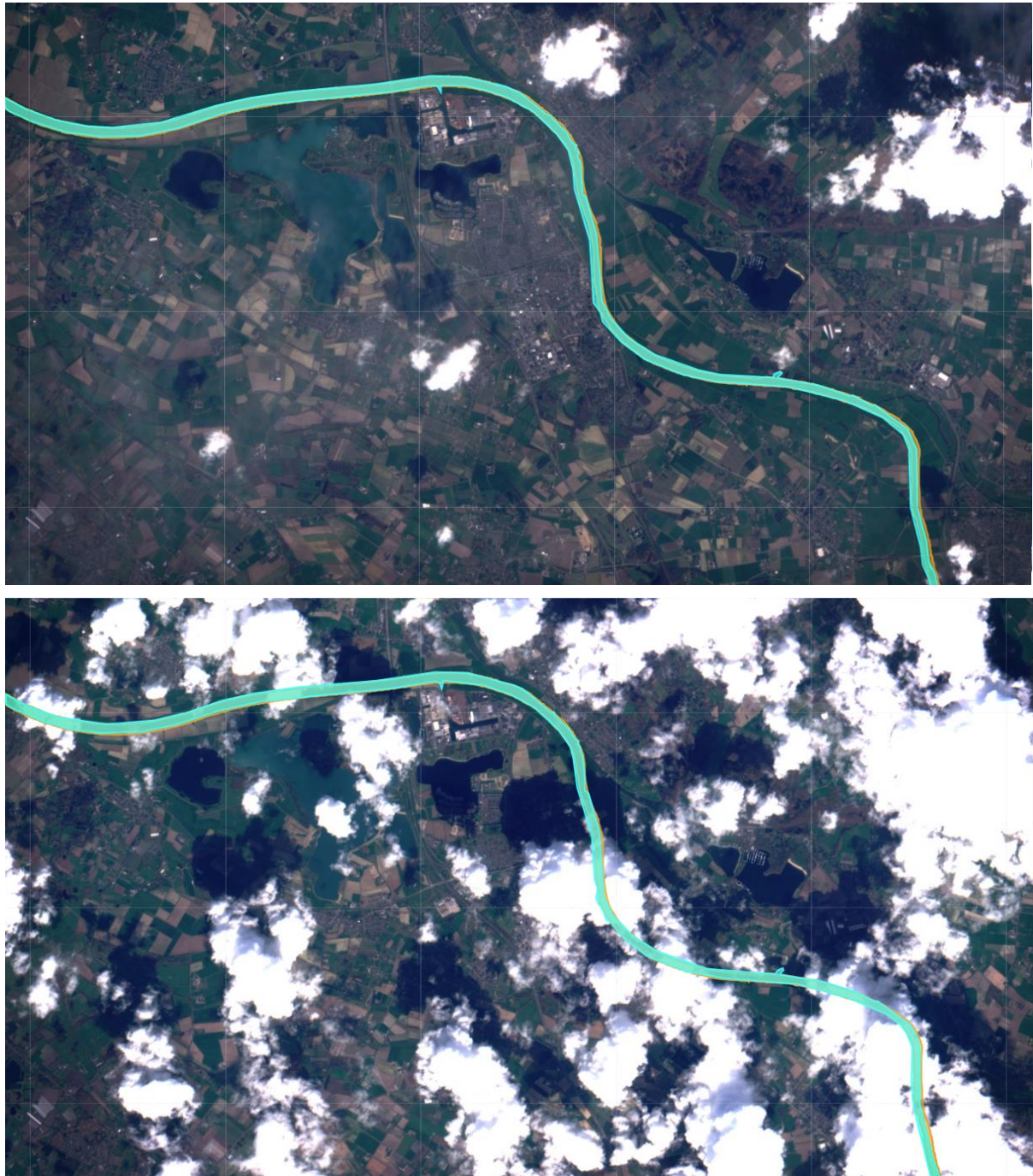


Figure C.1 – Differences between an automatically generated river polygon (cyan) and a river polygon provided by Rijkswaterstaat (orange) for a segment of the Meuse, for both cloudless and cloudy satellite images.

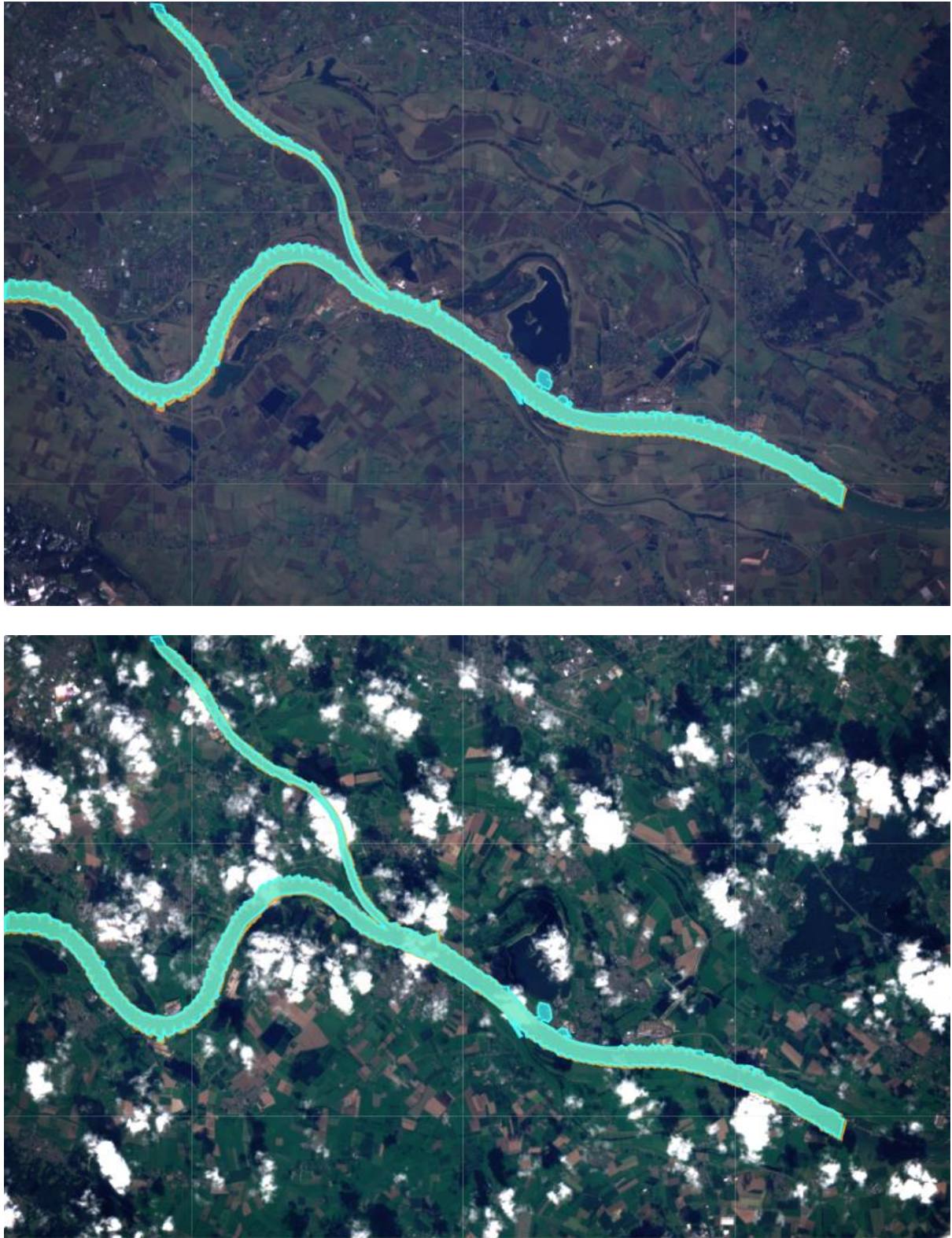


Figure C.2 – Differences between an automatically generated river polygon (cyan) and a river polygon provided by Rijkswaterstaat (orange) for a segment of the Rhine, for both cloudless and cloudy satellite images.

APPENDIX D: RIVER CLASSIFICATION SCHEME

To assess the global applicability of the formed procedure, polygons were generated for seven rivers around the world. A variety of rivers were selected based on the classification scheme by Alabyan and Chalov (1998). The scheme is illustrated in Figure E.1.

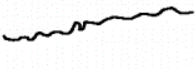
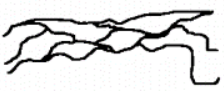
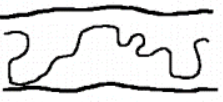
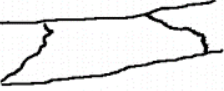
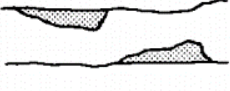
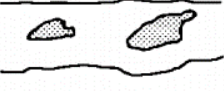
structural level	plan outline			limiting conditions
	straight	sinuous	branched	
valley bottom	 single-thread	 macromeanders	 anabranching	 wide floodplain
flood channel	 straight	 meandering	 braided (or split)	 confined channel
low water channel	 riffle-pool sequences	 alternate bars	 medial bars	 incised channel

Figure D.1 – Classification of river channel patterns (Alabyan and Chalov, 1998).

APPENDIX E: SCRIPTS & TYPICAL MEMORY USAGE

The scripts that have been created to estimate the geometry of a river in a more or less automated manner are presented below. The scripts are hosted on the GEE servers and are openly available for anyone to read. Comments are presented sparingly to keep the code clear. Script 1 depends on script 2 to run successfully.

Script 1: RiverGeometryEstimate

<https://code.earthengine.google.com/de107e51a3401d61adb5ea41169f6144>

Script 2: WaterOccurrenceComposite

<https://code.earthengine.google.com/bc112c19943c34c40cbe913df7b2ab45>

Repository

<https://earthengine.google.com/users/JThissen/ThesisScripts/>

Furthermore, the result of profiling a typical script (in this case a segment of the Trinity River), revealing the utilized resampling techniques—and, indirectly the projection scale—to be the main culprit in terms of peak memory usage.

Compute	Peak Mem	Count	Description
33396.578	119M	806020	Algorithm Image.resample computing pixels
16660.275	678k	499948	Algorithm Image.reduceRegion
6744.136	603k	25318	Algorithm Window.min computing pixels
5109.743	166k	69230	Algorithm reduce.product
4259.889	19M	360750	Algorithm Image.load computing pixels
3263.224	13M	22551684	(plumbing)
1537.492	105M	1888507	Loading assets: (...)/(...)
1488.083	5.4M	73252	Algorithm Image.clip computing pixels
1289.895	5.9M	73630	Algorithm Image.convolve computing pixels
1260.320	4.2M	416648	Algorithm Image.cast computing pixels
1159.273	2.7M	18878	Algorithm Window.max computing pixels
1102.258	2.6M	129974	Algorithm Image.gte computing pixels
879.132	2.3M	24540	Algorithm Image.hypot computing pixels
863.440	5.9M	6426	Reprojection precalculation between (...) and (...)
330.771	2.3M	2401967	Algorithm Image.select
320.508	368k	4600	Algorithm reduce.sum
267.680	2.3M	24540	Algorithm Image.atan2 computing pixels
249.325	519k	53310	Algorithm Image.gt computing pixels
145.948	576k	584	Algorithm Window.mode computing pixels
142.151	448k	12432	Algorithm Image.lt computing pixels
132.393	2.2M	24540	Algorithm CannyEdgeDetector computing pixels
119.645	1.1M	984027	Algorithm Image.mask
113.162	924k	813730	Algorithm Image.rename
76.334	448k	49662	Algorithm Image.updateMask computing pixels
55.799	437k	115174	Algorithm Image.clip
54.939	763k	259007	Algorithm Image.resample
40.334	18M	44674	Algorithm (user-defined function)
39.187	8.9M	11312	Algorithm Image.connectedPixelCount computing pixels
34.343	110k	244935	Algorithm Image.normalizedDifference
34.305	6.5M	2324	Algorithm Image.paint computing pixels
31.393	1,010k	121857	Algorithm Image.unitScale
26.419	1.0k	834088	Algorithm Image.constant computing pixels
26.370	62k	1293003	Algorithm Image.constant
25.092	299k	107946	Algorithm Image.cast
23.312	8.1M	626	Algorithm Image.fastDistanceTransform computing pixels
21.871	564k	3426	Algorithm Geometry.buffer
21.544	222k	107946	Algorithm Landsat.TOA
21.527	122k	154437	Algorithm Image.updateMask
19.753	7.3k	43133	Algorithm Feature.intersects
19.357	423k	963479	Algorithm Image.min
17.446	1.3M	104048	Algorithm Image.normalizedDifference computing pixels
16.239	386k	1004992	Algorithm Image.subtract
16.131	2.1k	410072	Algorithm Landsat.TOA computing pixels
16.110	408k	1006066	Algorithm Image.divide

Figure E.1 — Profiling results of a segment of the Trinity River based on bilinear interpolation as well as a 10×10 meters pixel resolution.

Compute ▼	Peak Mem	Count	Description
36062.617	117M	806020	Algorithm Image.resample computing pixels
17925.652	2.1M	503067	Algorithm Image.reduceRegion
7286.752	603k	25318	Algorithm Window.min computing pixels
5507.720	173k	69230	Algorithm reduce.product
4548.814	19M	360750	Algorithm Image.load computing pixels
3665.771	20M	22659932	(plumbing)
1603.704	5.4M	74368	Algorithm Image.clip computing pixels
1597.881	105M	1894129	Loading assets: (...)/(...)
1390.178	5.9M	73630	Algorithm Image.convolve computing pixels
1355.910	3.0M	416648	Algorithm Image.cast computing pixels
1250.370	2.7M	18878	Algorithm Window.max computing pixels
1173.027	2.6M	129974	Algorithm Image.gte computing pixels
919.709	2.3M	24540	Algorithm Image.hypot computing pixels
898.396	5.9M	6426	Reprojection precalculation between (...) and (...)
353.155	2.3M	2401965	Algorithm Image.select
341.510	368k	4600	Algorithm reduce.sum
287.435	2.3M	24540	Algorithm Image.atan2 computing pixels
271.331	519k	53310	Algorithm Image.gt computing pixels
159.771	576k	584	Algorithm Window.mode computing pixels
154.189	448k	12432	Algorithm Image.lt computing pixels
142.845	2.2M	24540	Algorithm CannyEdgeDetector computing pixels
127.467	1.1M	984027	Algorithm Image.mask
120.308	924k	813730	Algorithm Image.rename
82.780	448k	49662	Algorithm Image.updateMask computing pixels
61.443	437k	116020	Algorithm Image.clip
59.110	763k	259007	Algorithm Image.resample
56.077	6.5M	3440	Algorithm Image.paint computing pixels
42.811	8.9M	11312	Algorithm Image.connectedPixelCount computing pixels
41.888	21M	44738	Algorithm (user-defined function)
39.665	8.1M	1184	Algorithm Image.fastDistanceTransform computing pixels
36.889	110k	244935	Algorithm Image.normalizedDifference
33.758	1,010k	121857	Algorithm Image.unitScale
29.222	944	835204	Algorithm Image.constant computing pixels
28.475	62k	1294707	Algorithm Image.constant
27.365	299k	107946	Algorithm Image.cast
23.641	222k	107946	Algorithm Landsat.TOA
23.587	122k	154437	Algorithm Image.updateMask
20.906	423k	963479	Algorithm Image.min
19.522	6.4k	43507	Algorithm Feature.intersects
19.427	1.3M	104048	Algorithm Image.normalizedDifference computing pixels
18.152	571k	3539	Algorithm Geometry.buffer
17.714	1.8k	410072	Algorithm Landsat.TOA computing pixels
17.411	386k	1004992	Algorithm Image.subtract

Figure E.2 – Profiling results of a segment of the Trinity River based on bicubic interpolation as well as a 10×10 meters pixel resolution.

APPENDIX F: INACCURATE ESTIMATES UNDER HIGHLY VARIABLE CONDITIONS

The approach towards the estimation of the course of a river under cloudy circumstances is currently flawed in case the stream width is highly variable over time (e.g. as a result of a highly variable discharge pattern). Under cloudy conditions, at least one cloudless image of which the stream width is similar to the stream width of the river of interest needs to be sampled to provide a reasonably accurate estimate. If such an image cannot be sampled, the method may fail under highly variable conditions. The scenarios where the method fails to provide a reasonably accurate representation of the course of a river are demonstrated in Figure F.1 and F.2.

Scenario 1

Consider a relatively narrow river, as depicted in Figure F.1 (1). Under cloudy conditions, several segments of the river are unknown due to the presence of clouds (2). In this scenario, the historical composite represents a vast overestimation (3). Since A_{ratio} is larger than $max(K)$, the bounds of the historical composite are not eroded (see §3.3). (2) and (3) are subsequently merged, resulting in (4), which is a severe overestimation of the bounds of a river.

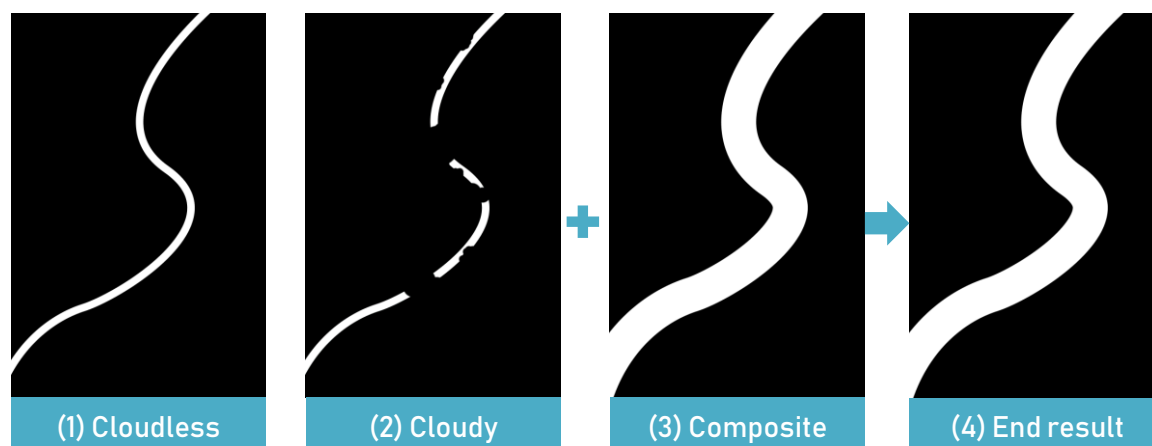


Figure F.1 – Scenario for a relatively narrow river subject to highly variable surface water widths.

Scenario 2

Consider a relatively wide river, as depicted in Figure F.2 (1). Under cloudy conditions, several segments of the river are unknown due to the presence of clouds (2). In this scenario, the historical composite represents a vast underestimation (3). Since A_{ratio} is larger than $max(K)$, the bounds of the historical composite are not modified. (2) and (3) are subsequently merged, resulting in (4), where “gaps” are severely underestimated.

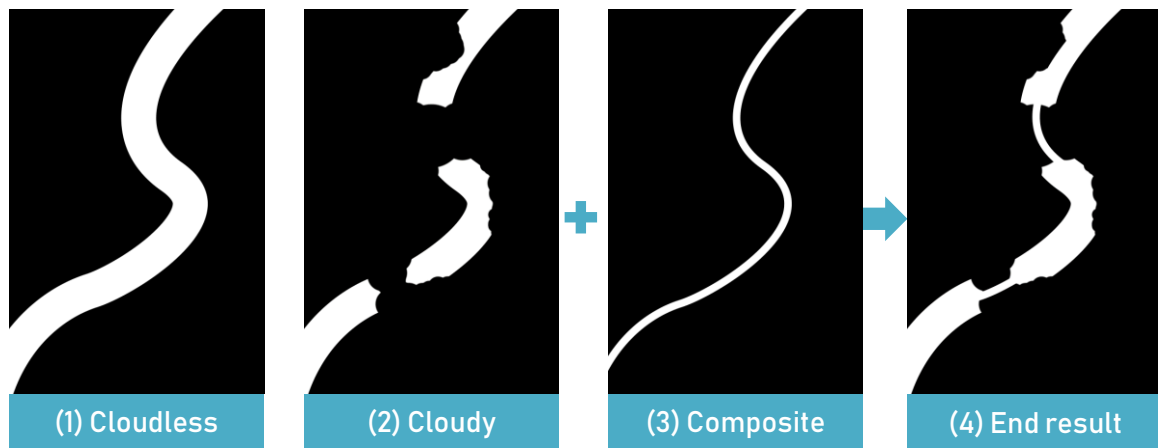


Figure F.2 – Scenario for a relatively wide river subject to highly variable surface water widths.